Seismic Assessment of Geothermal Potential – Concept and Application

Case Study of the German Continental Deep Drilling Site (KTB)

Dissertation
zur Erlangung des Doktorgrades
der Mathematisch-Naturwissenschaftlichen Fakultät
der Christian-Albrechts-Universität
zu Kiel

vorgelegt von

Eva Szalaiová

Kiel, 2012

Referent:	Prof. Dr. Wolfgang Rabbel
Koreferent:	Prof. Dr. Hans-Jürgen Götze
Tag der mündlichen Prüfung:	Kiel, den 19. April 2012
Zum Druck genehmigt:	Kiel, den 19. April 2012

Der Dekan

Abstract

Geothermal reservoirs can embody safe, accessible and stable sources of renewable and environmentally friendly energy. In order to access and extract this energy, drilling of deep wells connected with vast financial investments is unavoidable. Thorough pre-drilling exploration followed by simulations of heat extraction can help to assess the site's geothermal energy potential and thus lower the risk of possible financial losses.

Extraction of heat enclosed in the deep rock can be simulated with a two-well geothermal system. Through one of the wells cool water is being injected into the reservoir, where it is heating up while travelling towards the production well. If certain conditions are fulfilled, water pumped to the surface carries the amount of energy sufficient for geothermal power production. With simulations of such geothermal systems it is possible to predict their profitability and sustainability.

The extensive amount of scientific experiments performed during the Continental Deep Drilling Program (KTB) within the years 1985-1996 yielded a wide database of miscellaneous information concerning the continental crystalline crust. This and the fact that temperatures up to 265°C were measured in the KTB drill hole were the motives to choose the KTB site as case study representative for geothermal reservoirs located in crystalline environments.

In order to estimate the amount of heat available for extraction, it was necessary to consider not only the lithological composition but also the fracture inventory of the site. In a crystalline environment which is characterised by low matrix permeability, fluids tend to percolate through fractures. Therefore length of the travel path is closely related to the time available for heat exchange between the rock matrix and the circulating fluid. Based on three-dimensional reflection seismic data, it was possible to prepare a 3-D structural model of the KTB site which incorporates the lithological units as well as the complex network of fractures of different scales. Indispensable are also information concerning petrophysical rock properties. In the case of the KTB site, these data were at hand thanks to the huge amount of downhole measurements recorded in the two available boreholes.

To calculate the thermal and hydraulic field, coupled steady-state hydrothermal simulations were performed separately for a large scale model of the whole area. The resulting boundary conditions could then be used as input into more detailed models of doublet systems simulating the actual heat extraction. Resulting changes of production temperature and pressure in time show the potential of the KTB site to accommodate a successful geothermal installation.

The work concept followed during the geothermal potential assessment of the KTB site is applicable also for other reservoirs located in a similar environment.

Zusammenfassung

Geothermische Reservoire verkörpern Quellen erneuerbarer, sicherer und jahreszeitenunabhängiger Energie. Um diese Energie zu erreichen ist das Abteufen von tiefen Bohrlöchern unvermeidlich, was jedoch mit erheblichen finanziellen Kosten verbunden ist. Sorgfältige geophysikalische Untersuchungen und anschließende Simulationen der Wärmegewinnung können bei der Beurteilung des geothermischen Potentials der Lokation behilflich sein und somit das Risiko finanzieller Verluste senken.

Extraktion von Wärme aus dem tiefen Gestein kann mit Hilfe geohydrothermaler Dubletten simuliert werden. Durch eine der Bohrungen wird das kühle Wasser in das Reservoir eingeführt, wo es sich auf dem Weg zum dem Produktions-Bohrloch erhitzt. Sind bestimmte Vorausetzungen erfüllt, kann das zur Oberfläche gepumpte Wasser eine ausreichende Menge an Energie zur geothermischen Stromerzeugung mit sich führen. Mit Simulationen solcher Geothermieanlagen ist es möglich ihre Rentabilität und Nachhaltigkeit vorherzusagen.

Die zahlreichen wissenschaftlichen Experimente, die innerhalb des Projektes der Kontinentalen Tiefbohrung (KTB) in den Jahren 1985-1996 durchgeführt wurden, ergaben eine umfangreiche Datenbank. Dies und die Tatsache, dass Temperaturen bis zu 265°C in dem KTB Bohrloch gemessen wurden, waren die Beweggründe die KTB Lokation repräsentativ für geothermische Reservoire in kristallinem Gestein zu wählen.

Um die vorhandene Wärmemenge abschätzen zu können, ist es notwendig nicht nur die lithologische Zusammensetzung, sondern auch das Verwerfungsnetzwerk der Lokation zu betrachten. In kristallinem Gestein, welches sich durch geringe Permeabilität auszeichnet, tendieren Flüssigkeiten dazu sich innerhalb der Verwerfungen zu bewegen. Deswegen hängt die Länge des zu durchquerenden Pfades eng mit der Wärmeaustauschzeit zwischen dem Gestein und der zirkulierenden Flüssigkeit zusammen.

Ausgehend von dreidimensionalen reflexionsseismischen Daten war es möglich ein 3-D Strukturmodell der KTB Lokation zu erstellen, welches sowohl Angaben über die lithologischen Einheiten, als auch über das komplexe Verwerfungsnetzwerk enthält. Unverzichtbar sind auch Informationen über die petrophysikalischen Eigenschaften des Gesteins. In dem Fall der KTB Lokation lagen genug solcher Daten vor, Dank der enormen Menge an Messungen, die in den zwei vorhandenen Bohrungen aufgenommen wurden.

Um das thermische und hydraulische Feld zu verstehen, wurden gekoppelte steady-state hydrothermische Simulationen des gesamten Gebietes durchgeführt. Die daraus resultierenden Randbedingungen wurden anschließend für detailliertere Dubletten-Modelle genutzt um die tatsächliche Wärmeproduktion zu simulieren. Aus der zeitlichen Änderung der Produktionstemperatur und des Druckes können Schlußfolgerungen in Bezug auf die geothermische Nutzbarkeit der Lokation gezogen werden.

Das in dem Falle der KTB Lokation verfolgte Konzept der Beurteilung des geothermischen Potentials ist auch für andere Reservoire mit ähnlichen Eigenschaften anwendbar.

Table of Contents

Chapter 1

Motivation and Concept

The constantly increasing energy consumption together with the slowly disappearing fossil fuels is the reason why the global power industry is in need to turn towards new energy sources. Due to these urging facts, also world governments are starting to increase funding of alternative energy research and encouraging the development of renewable energy power stations.

The heat inside the Earth is the strongest renewable energy source known so far. At the same time, geothermal reservoirs can be reached from any place on the Earth within only 10 km or 12 km distance in the direction towards the Earth centre. Temperatures above 1000°C prevail in 99% of the Earth's volume and temperatures below 100°C in only 0.1% (Rybach & Mongillo, 2006). This enormous quantity of heat comes partially from the residual heat of planetary formation and partially from the decay of naturally radioactive elements (^{238}U, ^{235}U, ^{232}Th and ^{40}K). At the human time scale, geothermal energy can be considered as renewable, since the energy taken from the source is being continuously replaced. On the other hand, this statement is only true if the resource is being exploited in a sustainable manner. Definition of sustainable production from a geothermal reservoir suggested by Axelsson et al. (2001) says: "For each geothermal system and for each mode of production, there exists a certain level of maximum energy production, below which it will be possible to maintain constant energy production from the system for a very long time". This means that even though we are talking about a renewable energy source, excessive extraction can still lead to depletion and deterioration of the geothermal reservoir.

The heat derived from a geothermal source can be used either directly, or for electricity production. Direct use of geothermal energy can theoretically happen anywhere on the Earth's surface, but is presently concentrated mainly in regions with recent volcanic activity. Water of low to moderate temperatures is used directly in a variety of fields, such as agriculture, industry, space heating etc. (Fig. 1.1). One of the applications which found a wide usage is the geothermal heat pump. The pumps supply heating and cooling of buildings using pipe systems buried at shallow depths.

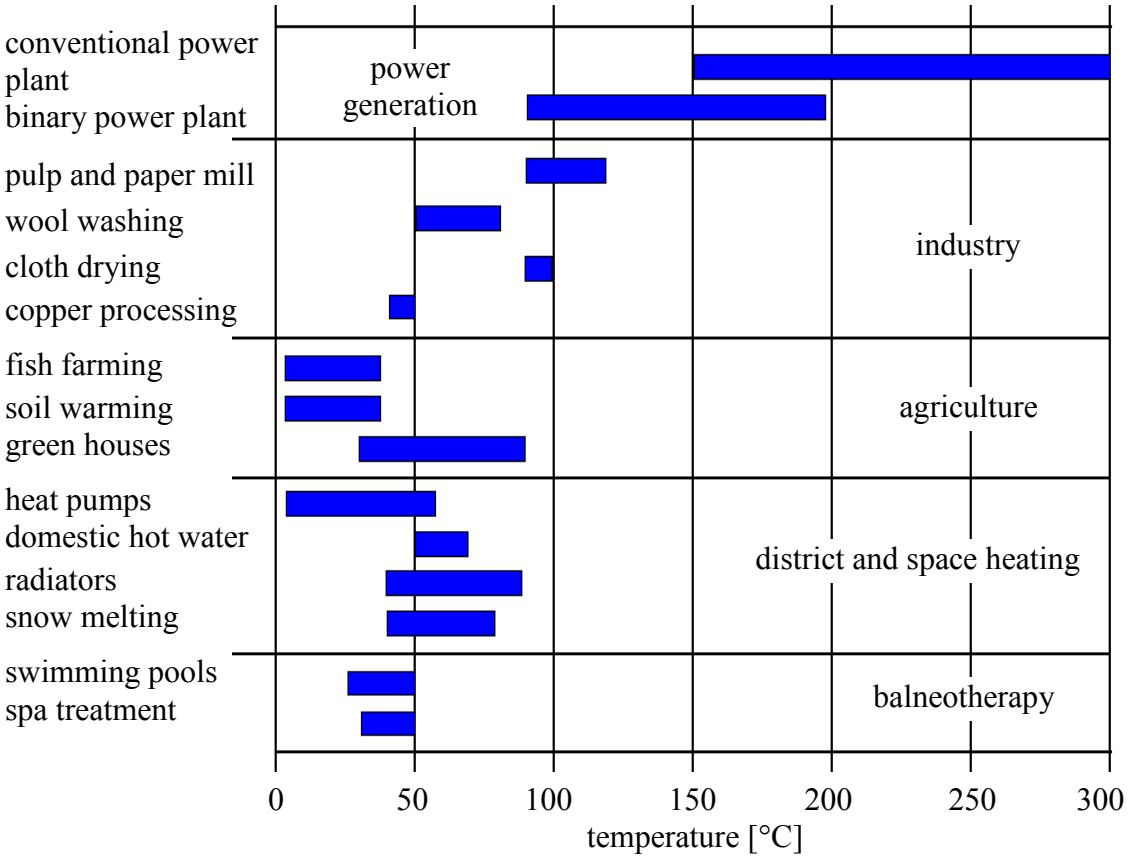

Fig. 1.1: *Some of the applications of geothermal energy with the required temperatures (Ngô et al., 2006).*

Although the number of countries producing geothermal power (Tab. 1.1) and the total worldwide geothermal power capacity under development increased significantly during the last years, still the number of countries using geothermal energy for power generation is relatively small. One of the reasons for this is the fact that until recently only water or steam of high temperatures could be utilized. This lead to limitations to areas with geothermal resources of temperatures above 150 °C. Latest developments in the technology of power production allow plants to generate electricity also from hydrothermal water at lower temperatures (less than 100 °C). This fact will enable power production from geothermal energy in a wider range of areas.

Tab. 1.1: *Top twenty-four countries generating geothermal power in 2010 (Holm et al., 2010).*

rank	country	installed capacity (MW)
1	United States	3086
2	Philippines	1904
3	Indonesia	1197
4	Mexico	958
5	Italy	843
6	New Zealand	628
7	Iceland	575
8	Japan	536
9	El Salvador	204
10	Kenya	167
11	Costa Rica	166
12	Nicaragua	88
13	Russia	82
14	Turkey	82
15	Papua New Guinea	56
16	Guatemala	52
17	Portugal	29
18	China	24
19	France	16
20	Ethiopia	7.3
21	Germany	6.6
22	Austria	1.4
23	Australia	1.1
24	Thailand	0.3

1.1 Motivation

The use of geothermal energy brings a lot of benefits. Reduction of negative impacts of mining, transport, processing and the use of fossil fuels on the environment is one of the most important ones. It is also safe and has a rather small effect on the environment and the use of space. There are several ways to make use of the energy which the heat within the Earth provides. Whereas the use of shallow geothermal sources for purposes of heating is the most obvious way, more interesting is to use the enormous energy from deep reservoirs for electrical power production.

Presently, costs for a survey at a possible geothermal site and the following necessary drilling are way to high to be considered as an alternative to present energy sources, especially since prediction methods considering the amount of usable heat within the reservoir are still inaccurate and not reliable. Indicators of a geothermally relevant location are subtle and thus methods of hydraulic and thermal parameters estimation need improvement.

Within the joint project under the name MeProRisk (Neuartige Methodik zur Aufsuchung, Erschließung und Nutzung geothermischer Lagerstätten. Toolbox zur Prognose und Risikobewertung), five institutes, each with a different field of expertise, have been developing strategies for better understanding of the thermal regime and heat transport processes in great depths. The close cooperation of the partners brought improvements of current approaches which may enable a better quantitative estimation of uncertainties and financial risks involved in the geothermal reservoir prediction.

One of the locations chosen for the development of new and improved methods of geothermal reservoir assessment was the site of the Continental Deep Drillhole (KTB). At this site, one shallower pilot hole (KTB-VB) and one deep main hole (KTB-HB) have been sunk into the rock of the Southern German crystalline. The high temperatures measured in the KTB-HB at the final depth of 9101 m (265°C) and the geological settings make this location interesting from the geothermal point of view. KTB as one of the largest and most expensive programs in geosciences undertaken in Germany, with the huge amount of gathered data, provides a great database for further research. Aim of this thesis was to analyse the available seismic cross-sections together with borehole measurements and evaluate the input which seismic data can contribute to the topic of geothermal reservoir assessment.

Crystalline rock of the southern Germany is of course not the only geothermally relevant location in Germany. Another site located in the North German Basin of a noteworthy hydrothermal potential has also been analysed within the frame of the MeProRisk project. Assessments of this sedimentary site can be found in Vogt et al. (2012).

1.2 Concept

The amount of heat extracted from a geothermal reservoir is controlled by a number of properties, such as temperature gradient, porosity and permeability of the rock, rock petrophysical properties, water stored in the underground, etc. These factors influence not only the process of heat extraction itself but also play a role in the economical component of geothermal energy production.

In order to estimate hydrothermal characteristics of a reservoir correctly, it is necessary to combine the information about geological and tectonic settings of the site provided by the interpretation of seismic sections with petrophysical properties of the rock matrix and finally complement it with thorough coupled hydrothermal simulations (Fig. 1.2).

Petrophysical properties important for hydrothermal simulations are lithology dependent. Classification of the seismic dataset into the main lithological units required considerable effort and the combination of several sources of additional information (Chapter 4). Absolute values of petrophysical properties (such as permeability, porosity, thermal conductivity and heat production) were taken from borehole measurements, which in the case of the KTB are freely accessible and were supplemented with values from different literature sources.

Due to the characteristics of crystalline rock, as it is found at the Continental Deep Drillhole site, we can expect low matrix permeability values and thus fluid movement preferably through fractured media. Detailed knowledge about the geometry of faults is required to determine fracture permeability. The available reflection seismic dataset recorded at the KTB site has been reprocessed, analysed and interpreted with the above mentioned aim in mind (Chapter 5).

Thermal and hydraulic processes taking place in the underground were computed for the model of the KTB site by means of coupled hydrothermal simulations (Chapter 6). Resulting calculated temperatures were compared with the real temperatures measured in the boreholes, providing a verification of the structural model. Additional simulations of two-well heat extraction systems shall help to evaluate the site's suitability for geothermal exploitation.

Due to the considerable amount of processed data, a special focus had to be put on the automatisation of the work flow or at least at its segments. The above described concept (Fig. 1.2) is a joint effort of the Kiel MeProRisk group.

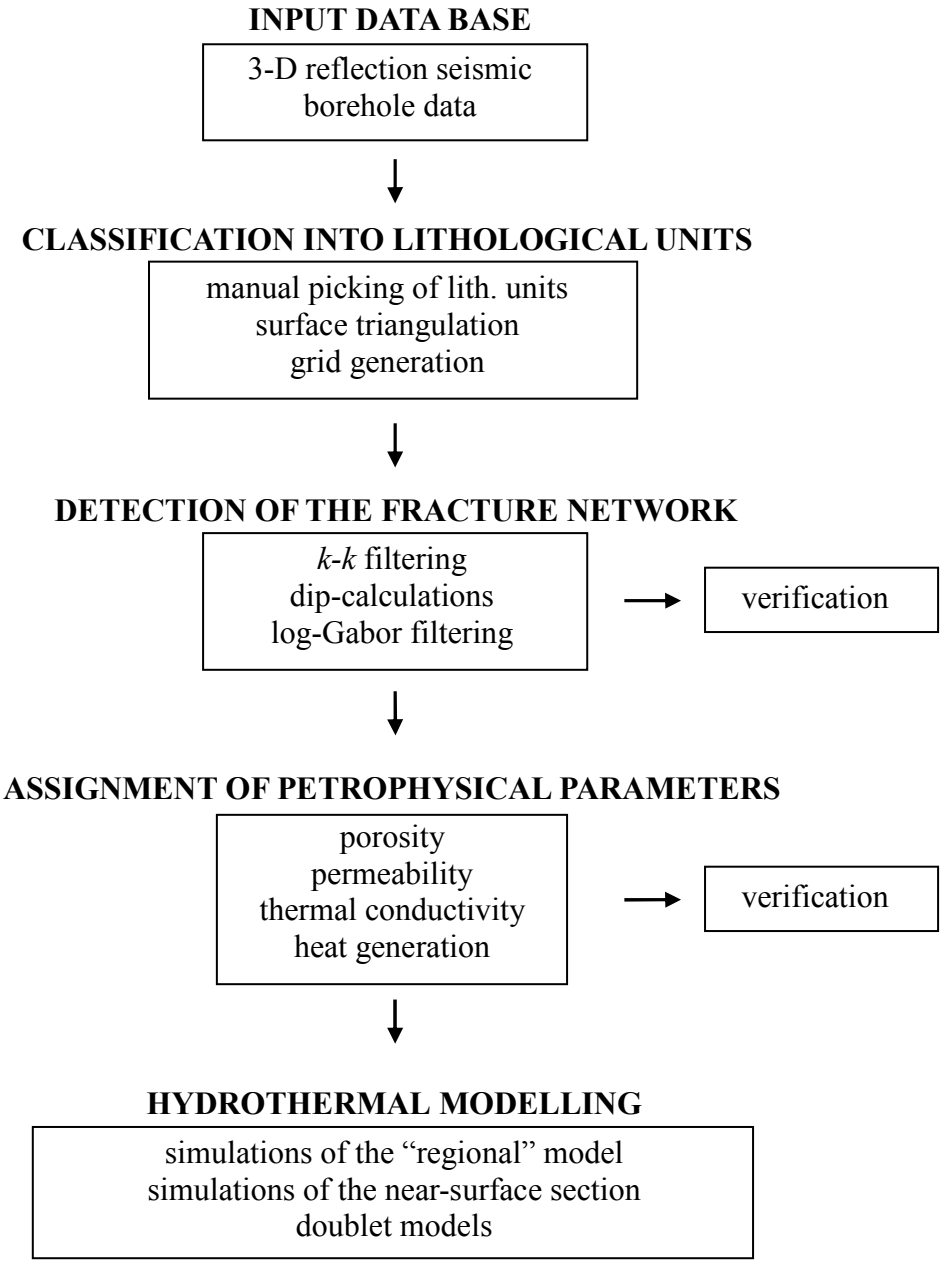

Fig. 1.2: *Concept of structural model construction for coupled thermal and hydraulic simulations on the basis of seismic data. The concept has been applied to the test-location of the Continental Deep Drillhole (KTB).*

Chapter 2

Geoscientific Frame

Numerous papers and reports describing the detailed geological settings at the site of the Continental Deep Drillhole (KTB) have been published by a number of authors. Just to name some of them: Emmermann & Wohlenberg (1989), Emmermann & Lauterjung (1997), Harjes et al. (1997), Zulauf and Duyster (1997), etc. The following chapter shall give only a short and compact overview of the geological and tectonic settings relevant for the topic of this thesis. For a more detailed geoscientific background please see the above mentioned literature.

2.1 Geology and Tectonic Settings

The site of the Continental Deep Drillhole in the Oberpfalz is situated at the contact of two first-order units of the Variscan orogene: Saxothuringian in the NW and Moldanubian in the SE (Fig. 2.1). This suture zone has been formed by the closure of an early Paleozoic ocean during the Variscan collision in Devonian/Carboniferous times (400 – 300 Ma) (Emmermann & Lauterjung, 1997).

The tectonometamorphic unit Zone of Erbendorf-Vohenstrauß (ZEV), which is overlying the suture zone, can be assigned due to its lithological composition and its tectonometamorphic development neither to the Saxothuringian nor to the Moldanubian. According to Emmermann & Lauterjung (1997), the ZEV is a suture-related unit derived from the subduction and exhumation of the early Paleozoic oceanic crust which subsequently involved in the Variscan collision. It consists mainly of steeply inclined (dip between 50° - 80°) alternating layers of crystalline metabasites and gneisses which have been faulted and folded into synformes and antiformes during its complex tectonic history (Fig. 2.2). The KTB superdeep borehole is located directly within the ZEV unit and is crossing the crystalline metamorphic rocks, metabasites, gneisses and alternating gneisses and metabasites in its whole length (Pechnig et al., 1997). All the rocks penetrated by the borehole show signs of intense deformation history and metamorphosis of about 650 °C – 700 °C and 6 kbar – 8 kbar.

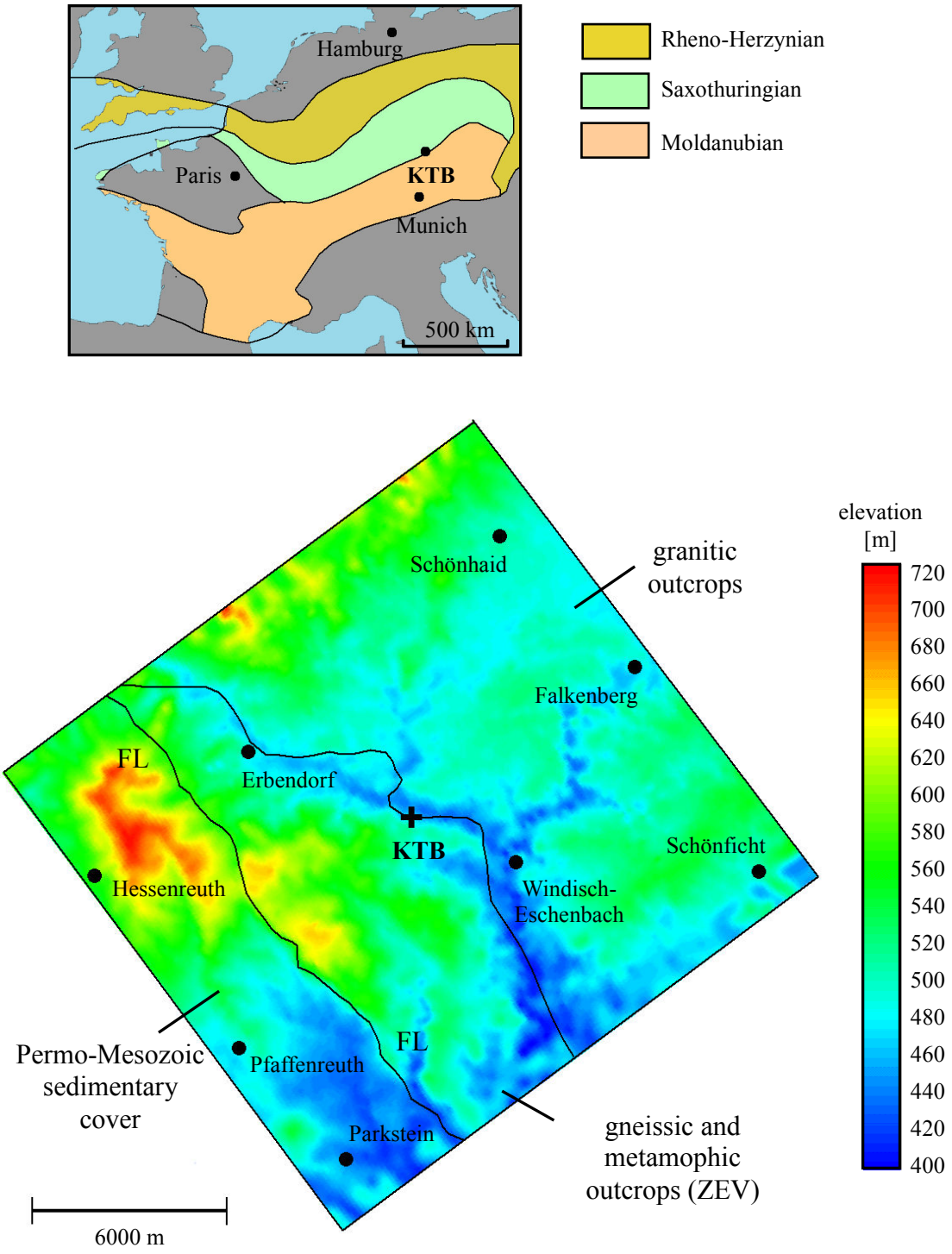

Fig. 2.1: *Upper figure shows the location of KTB at the suture zone of Saxothuringian and Moldanubian (after Emmermann & Lauterjung, 1997). Lower figure: the topography (in color code; provided by M. Stiller) of the area of interest with the main geological units and the Fraconian Lineament (FL) (after Dürbaum et al., 1990).*

Bordering the ZEV from north-east are granitic masses which to two thirds comprise of the Falkenberg granite. This dominating granitic unit is located about 2 km to the NE of the KTB drill site and represents a large exposed late Carboniferous pluton. Its position at the site is shown in Figure 2.2 and its shape is predicted by gravimetry and the interpretation of seismic measurements to be horizontal tabular–like, with a thickness of approximately 6 km to 7 km (Simon & Gebrande, 1994; Casten et al., 1997; Zulauf et al., 1997). The other units, namely granites of Steinwald, Mitterteich, Leuchtenberg, Flossenbürg and Bärnau, reach depths of 2 km – 3 km according to gravimetric modelling (Casten et al., 1997).

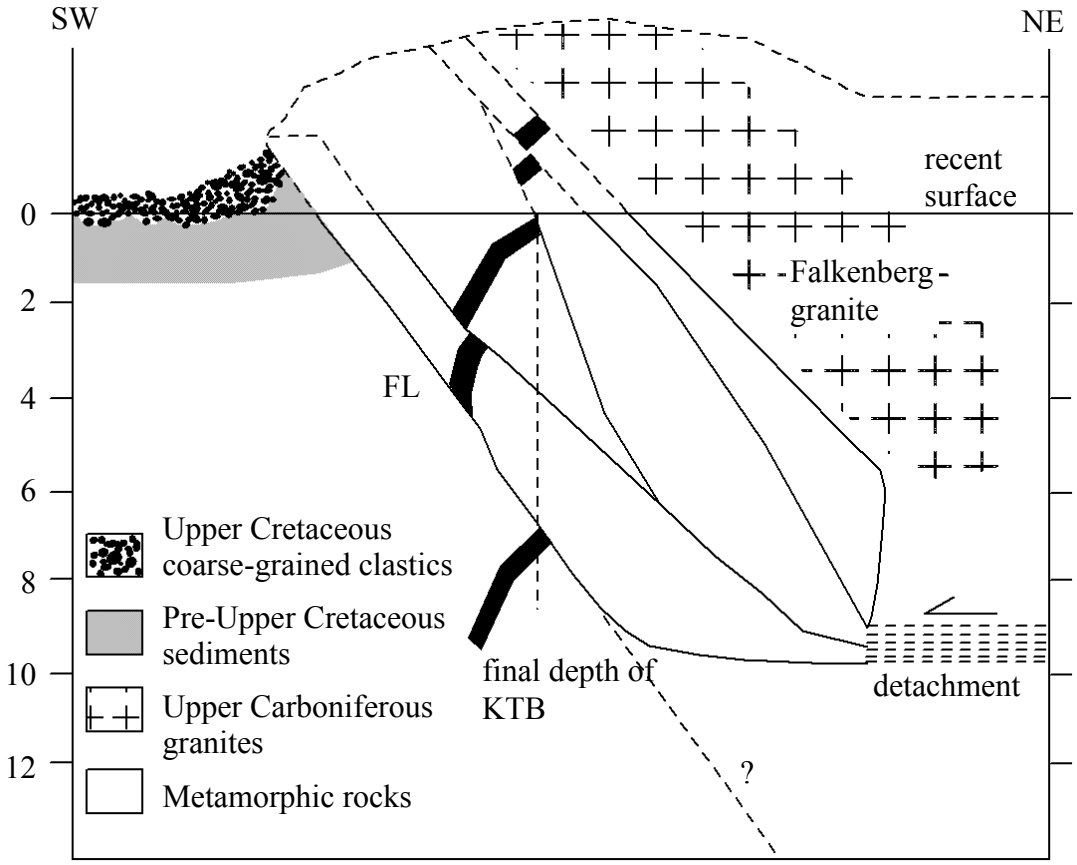

Fig. 2.2: *Cross-section through the KTB drilling site during the late-Cretaceous thickening and uplift. Denudation is largely accommodated by erosion. Location of prominent faults is taken from Hirschmann et al. (1994); the black marker horizon is fictitious indicating the attitude of the foliation and the amounts of fault displacement (Zulauf & Duyster, 1997).*

An up to 3000 m thick sedimentary cover from Permo-Mesozoic times is located in the south-west of the site and is separated from the crystalline metabasites and gneisses of the basement units (Zone of Erbendorf-Vohenstrauß) by the Franconian Lineament (Fig. 2.1). This important fault zone comprises of a number of NW-SE oriented reverse faults which are believed to be associated with late Variscan (early Triassic and Cretaceous) faulting and led to an intra-plate antiformal stack. The deep-reaching bundle of faults - the Franconian Lineament, functioned as the frontal ramp of this stack (Emmermann & Lauterjung, 1997). Hirschmann (1996) estimated the total horizontal displacement to be 5 km – 6 km and a vertical displacement of more than 3 km. In seismic data, the faults belonging to the Franconian Lineament (under the name “seismic events” (SE)), can be identified as steeply dipping reflectors with a dip of approximately 60° to the northeast and reaching up to 10 km depths. The most prominent fault zone has been detected in the KTB borehole in depths between 6850 m to 7260 m and a second major system was crossed in 7820 m to 7950 m depths (Emmermann & Lauterjung, 1997).

The Erbendorf body, a highly reflective zone in depths of around 8 km to 14 km was initially one of the main targets of the KTB drillhole. Due to technical problems caused by the unpredictable characteristics of the environment in the great depths, the Erbendorf body has never been drilled. Considering the results of various seismic experiments, the Erbendorf body has been interpreted as not actually an isolated body but an inhomogeneous zone of high reflectivities separated and shifted by the SE1 fault (Emmermann & Lauterjung, 1997).

2.2 Seismic Experiments in the Vicinity of the KTB

The decision to sink an internationally funded, superdeep drillhole into the crystalline rocks of Oberpfalz Germany, led to numerous pre-site experiments and surveys. A thorough overview of seismic measurements carried out within the years 1985 - 1996 in the area surrounding the KTB site offers Harjes et al. (1997).

The **DEKORP 4** (Deutsches Kontinentales Reflexionsseismisches Program) and **KTB 85** seismic experiments launched in the year 1984 and comprised a 187 km long NW-SE oriented DEKORP 4 profile of near-vertical reflection seismic and six shorter seismic lines, forming a broad network around the planned drill site. Lines KTB 8504, KTB 8505, KTB 8506 are oriented parallel to the DEKORP 4 profile. Perpendicular to it are the profiles KTB 8501, KTB 8502 and KTB 8503 (Fig. 2.3). Aim of this experiment was to investigate the crustal structure of the suture zone between the Saxothuringian and the Moldanubian and to bring new insights into the question concerning the origin of the Erbendorf body, as well as to aid during the selection of a suitable site for the KTB drillhole experiment (Schmoll et al., 1989). (http://www-app1.gfz-potsdam.de/ www/pb3/dekorp/dekorp4.html). A series of 96 dynamite shots for **wide-angle reflection** investigations (and expanding spread velocity recordings) was additionally conducted along the DEKORP 4 line with the help of which mainly the mid- to lower crust has been well imaged. Among the most interesting results was a high velocity zone in the area just below the Erbendorf body.

In 1989, after drilling of the pilot hole (KTB-VB) was almost finished, started the **ISO89** (Integrated Seismic Experiment Oberpfalz) measuring campaign in the surroundings of the drilling site (Dürbaum et al., 1990, 1992; Stiller, 1991; Wiederholt, 1991; Lüschen et al., 1991; Kemper & Harjes, 1991; Gebrande et al., 1991, Körbe et al., 1997). Seismic data, which can be directly linked to the information gathered in the borehole, have been collected at an area of the size approximately 20 km x 20 km. The principal component of this project was a near-vertical deep 3-D seismic survey aimed at the investigation of the complicated crystalline crust and resolving the structures in more detail. A wide-angle survey to investigate the spatial extend and internal structure of the Erbendorf body was carried out within ISO89, when shot points 101 to 120 have been observed by the receiver spread “Reflex 1” and shot points 201 to 221 by the receiver spread “Reflex 2” (Fig. 2.3).

Vertical seismic profiling (**VSP**) and moving source profiling (**MSP**) have been performed in the pilot hole as part of the ISO89 experiment as well (Lüschen et al., 1991), bringing insight into the reflectivity of the metamorphic rock.

A special study of the inner structure of the cataclastic zone, seismically named SE1 (“steep event 1”) has been undertaken within the **INSTRUCT** (Internal Structure) experiment (Wenzel et al., 1995).

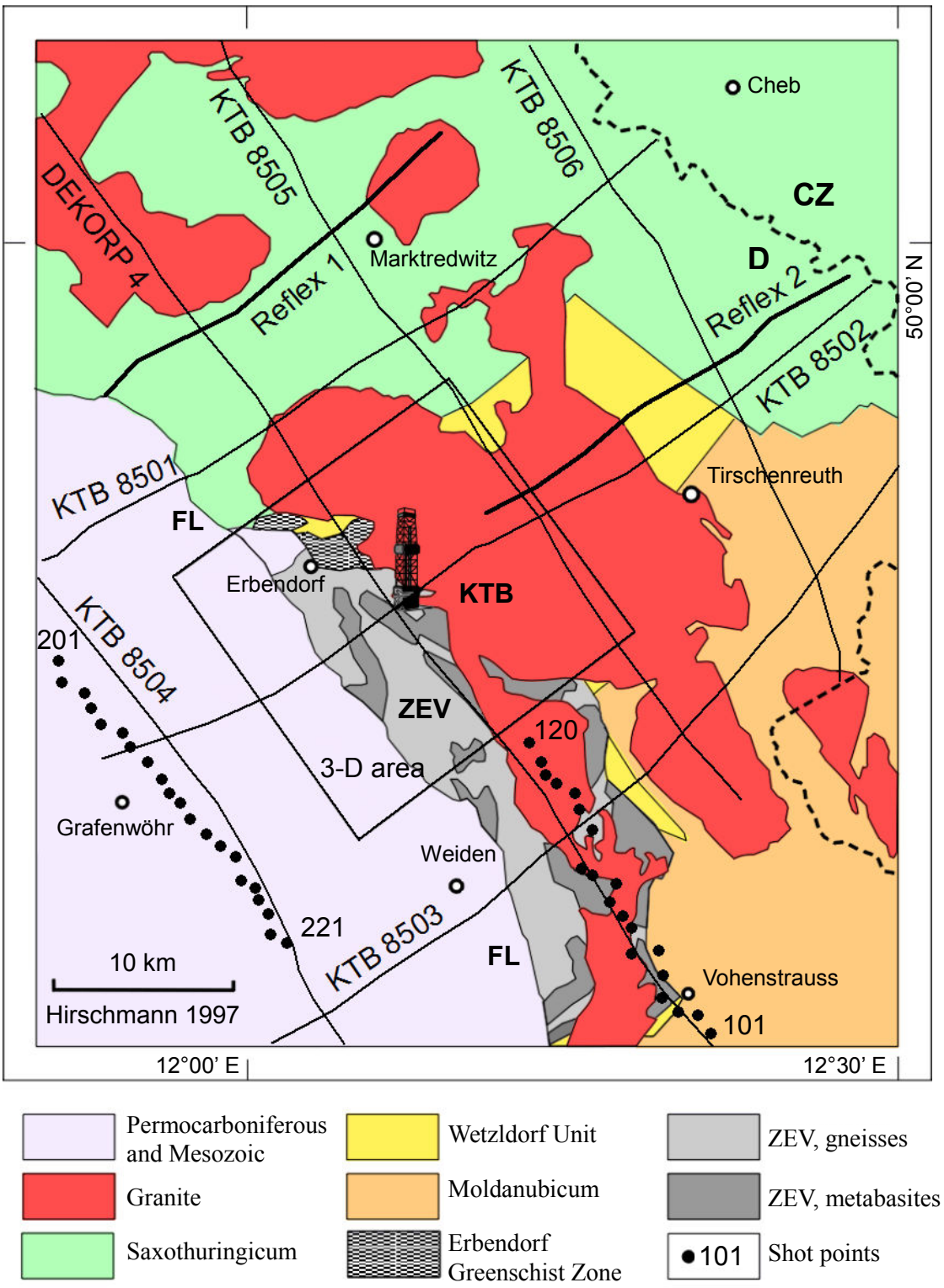

Fig. 2.3: *Location of seismic profiles and campaigns carried out in the vicinity of the KTB (after Harjes et al., 1997).*

2.3 Thermal & Hydraulic Conditions at the KTB Site

The KTB superdeep drillhole penetrating the crystalline continental crust provides valuable insight into the thermal regime and heat transport processes up to great depths. The pre-drilling temperature estimations based on temperature gradients from several shallow boreholes (less than 500 m deep) in the Oberpfalz, proved to be misleading (Burkhardt et al., 1989). While the predicted vertical temperature gradient of 21 K/km was correct up to the depth of 500 m, it starts to increase rapidly until 1500 m depth, where it becomes almost constant (28 K/km). These surprising results lead to a large number of experiments on core material and cuttings as well as to an extensive geothermal logging program.

Heat production and thermal conductivity as properties important for correct geothermal assessment of a reservoir have been measured directly on-site, at the KTB field laboratory. While core samples were available from the pilot borehole (KTB-VB), only cuttings could be used for the investigation of rock petrophysical properties in the main borehole (KTB-HB). The distribution of heat production reflects the local lithology and even though the data show a slight decrease, they definitely do not follow the law of exponential decrease of heat production with increasing depth (Emmermann & Lauterjung, 1997).

While laboratory data are of great quality, downhole recordings of temperature values in the KTB borehole can be described as insufficient. The drilling process is an extreme invasion into the thermal balance of the intersected rock masses. Since the end of the KTB drilling program in 1994, temperature in the boreholes is continuously recovering towards the undisturbed formation temperature. Several temperature logs have been performed in both KTB boreholes during different stages of their thermal relaxation. The latest complete temperature log in the pilot hole has been performed still during the recovery phase of the rock (250 days after drilling) and thus values reflecting the true undisturbed formation temperature can not be expected. Next temperature log followed in 13 months, but due to technical difficulties, it reached only 2000 m depth (Kohl & Rybach, 1996). Clauser et al. (1997) describes temperature profiles recorded in KTB-HB before shut-in and the temperature log recorded 17 months after shut-in. The latest profiles, on which recovering of temperatures is still obvious, were measured in the KTB-HB in March 1996, January 1997 and January 1998 (Fig. 2.4).

Heat flow calculated from the temperature gradient and vertical thermal conductivity by Huenges & Zoth (1991) varies significantly with depth. In 500 m depth occurs a sharp increase raising the average heat flow from about 52 mWm^{-2} to a mean value of 83 mWm^{-2}. Jobmann & Clauser (1994) performed tests to explain the unexpected heat flow behaviour at the KTB site. Although the nature of the KTB regime could not yet be understood completely, several different processes are evident even though their contributions can not be quantified. Possible reasons for such a significant heat flow variation could be: steady-state lateral conductive heat flow effects; steady-state heat advection by percolating surface water; transient diffusion of variable ground-temperature history into the subsurface.

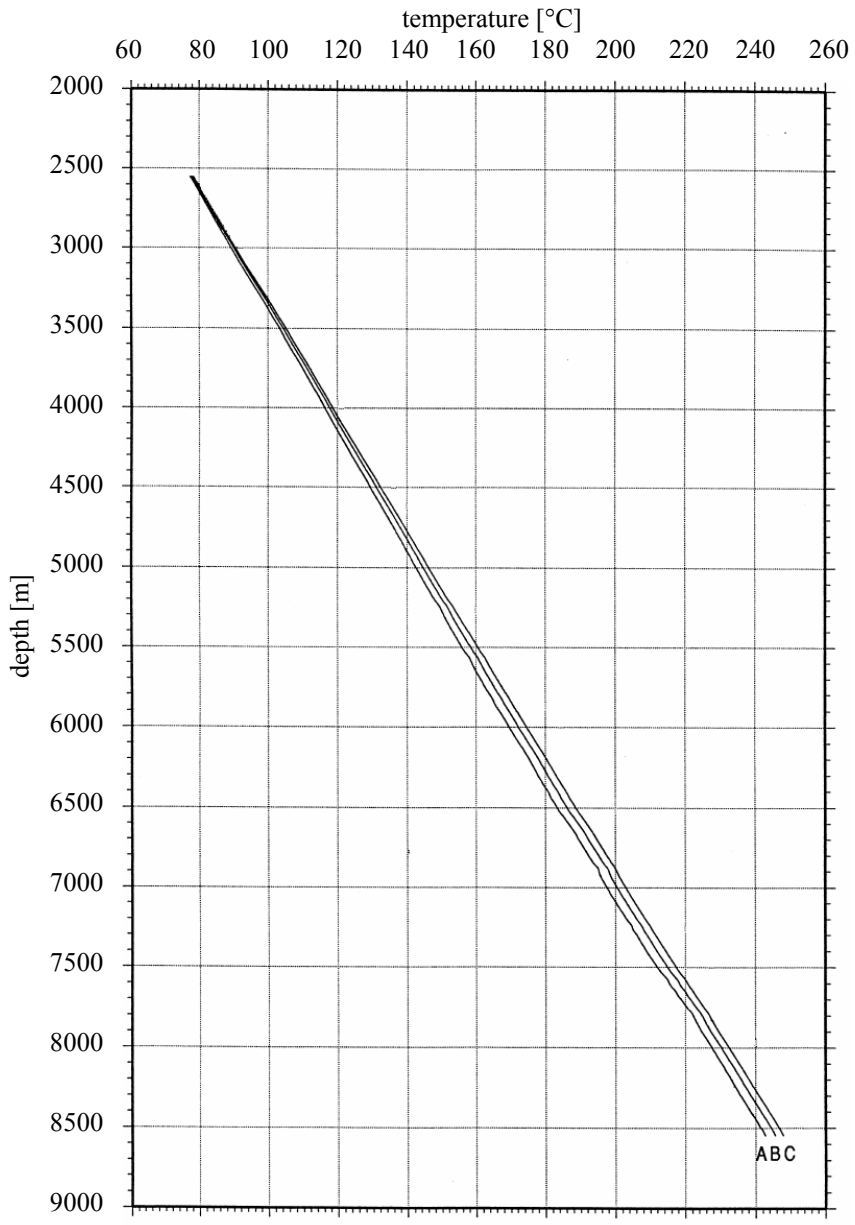

Fig. 2.4: *Temperature logs measured in the KTB-HB after shut-in. A temperature log measured in March 1996; B temperature log measured in January 1997; C temperature log measured in January 1998 (after Wilhelm, 2000).*

A number of shallow boreholes is located in the vicinity of the survey site. Table 2.1 lists the boreholes (Fig. 2.5) of various depths, penetrating different geological structures (Jobmann & Clauser, 1994). From the 25 listed boreholes with available temperature measurements, 21 are situated within the crystalline rocks of the Bohemian Massif and 4 are crossing the sedimentary layers west of the Franconian Lineament.

Tab. 2.1: *Boreholes located in the vicinity of the KTB with their final depths and temperatures measured at 100 m depth (Jobmann & Clauser, 1994).*

number	borehole	final depth [m]	temperature at 100 m depth [°C]
1	Weissenstein	217	7.9
2	Alexanderbad	100	8.2
3	Egerer Waldhäusl 9/90	200	8.38
4	Wülfersreuth	200	8.4
5	Griesbach	278	8.5
6	Poppenreauth	239	8.6
7	Egerer Waldhäusl 8/90	200	8.61
8	Hermannsreuth 6/89	200	8.8
9	Neusorg-Hoell	291	8.9
10	Kondrau Bayernquelle	235	9
11	Weissenstadt	207	9
12	Röthenbach	144	9.1
13	Püllersreuth	275	9.2
14	Remmelberg	145	9.4
15	Friedersreuth 10/90	250	9.87
16	Falkenberg NB3, PB7	500	9.9
17	Sybillenbad H1	315	10
18	Erbendorf 5/89	150	10.11
19	Sybillenbad A	250	10.3
20	KTB-VB	4000	10.5
21	Lengenfeld II	400	10.6
22	Dobrigau 7	171	10.96
23	Weiden T1	1222	11.7
24	Bayreuth	1122	12.7
25	Obernsees 1	1279	17

As the regional temperature trend for the depth 100 m measured in the shallow boreholes and plotted in Figure 2.5 shows, temperatures are higher in the sediments than in the crystalline rock. Jobmann & Clauser (1994) suggest a lateral heat transfer leading from the Bohemian Massif across the Franconian Lineament into the sedimentary foreland possibly through an active regional groundwater flow system concentrated within the top 500 m.

Valuable information for the understanding and evaluation of modelling results can be the knowledge about water percolation behaviour within the shallow boreholes. There seems to be a different behaviour of water flow at sites in the Bohemian Massif and at sites in the sediments west of the Franconian Lineament. Peclet number analysis of T-logs from the shallow boreholes done by Jobmann & Clauser (1994) shows that in all sites located within the crystalline rocks, the water movement has a downward direction, while in the sites to the west of the FL, the water seems to be percolating upwards.

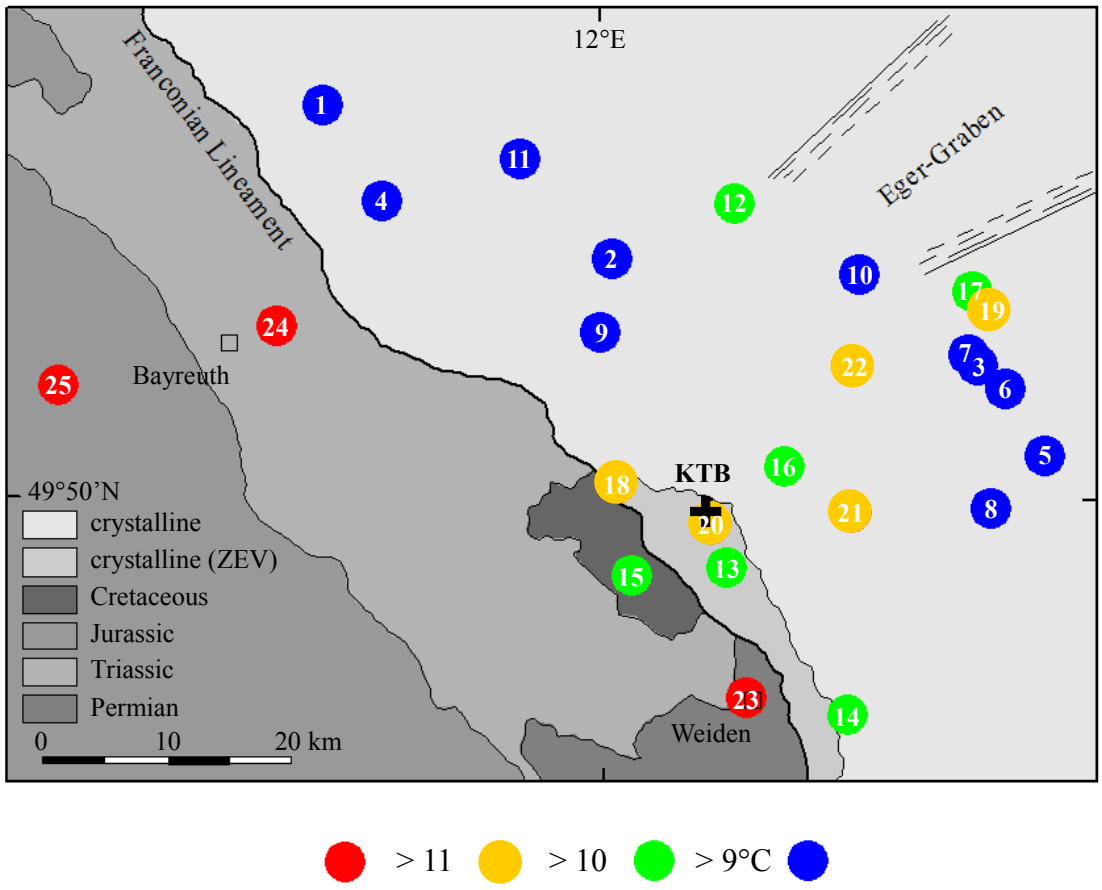

Fig. 2.5: *Twenty-five boreholes located in the vicinity of the KTB including temperature values measured at 100 m depth below surface (after Jobmann & Clauser, 1994). Further information is listed in the Table 2.1.*

2.4 Summary

The Continental Deep Drillhole located within the Zone of Erbendorf-Vohenstrauß penetrates complexly folded layers of crystalline rock. The recovered cores and cuttings exhibit alternation sequences of the two main rock matrix components, the gneisses and metabasites. Reason for the complicated inner structure is a rich tectonic history of the Oberpfalz region. The ZEV, as the main lithological unit of the KTB site, is bordered from the NE by a large granitic unit composed to about 67% from the Falkenberg granite. A clear boundary line towards the foreland sediments in the SW draws the Franconian Lineament, one of the most significant features of the site. Formed during an intra-plate stack during late Variscan when it functioned as a frontal ramp, this steeply inclined fault zone can be followed into depths of about 10 km.

Thanks to the extensive logging accompanied by numerous scientific experiments performed in the two KTB boreholes, very accurate information are available of the material in the close borehole vicinity. Downhole surveys supplemented by high-precision data collected in the KTB field laboratory are part of the large database which is freely accessible for analysis or further processing. Structure of the wider area, including the most interesting features, such as the Franconian Lineament and the Erbendorf body, has been mapped with the help of numerous seismic methods. Pre- and post-drilling campaigns which focused on the investigation of the site's various characteristics turned the Oberpfalz into a highly surveyed region.

Among the countless experiments covering all varieties of subjects, the question about thermal and hydraulic conditions at the site belongs to the most interesting ones. The high temperature gradient, which is almost uniform throughout the whole depth of the drilled section, is making the KTB site a suitable geothermal test area. This is supported by the fact that rock properties necessary for coupled hydrothermal modelling, such as temperature, temperature gradient, thermal conductivity and heat production are known.

Chapter 3

Data Base

The following chapter gives an overview of the datasets processed, analysed or used in some way within the scope of this thesis. The main source of information was the depth migrated 3-D reflection seismic dataset accompanied by the available log data from the two KTB boreholes. Additional information offered the 2-D seismic line KTB 8502, which is crossing through the centre of the KTB site in the SW-NE direction and can be directly compared with cross-sections of the 3-D seismic dataset.

All data were provided by the GFZ Potsdam.

3.1 ISO89 3-D Seismic Dataset

The 3-D reflection seismic dataset recorded during the ISO89 (Integrated seismic Oberpfalz) measuring campaign, consists of 382 parallel crossline (NW-SE) and 357 parallel inline (SW-NE) profiles, of the length 19.1 km x 17.85 km. The data were recorded with a sampling interval of 4 ms and reach up to 16 km depth. The used bin size was 50 m x 50 m x 50 m and in the inner area of the size 15.2 km x 14.4 km, the coverage reached 15-fold (Körbe et al., 1997). Data acquisition parameters and field work are described in detail by Stiller (1991). As seen in the Figure 2.3, orientation of the area was chosen in accordance with the major tectonic feature of the site, the Franconian Lineament. This arrangement proved to be helpful during the processing of the seismic data, when handling the strong velocity variation between the sediments in SW and the crystalline rocks in the NE was less complicated.

The recorded 3-D seismic dataset has been thoroughly processed and migrated by the DEKORP group in the DEKORP Processing Centre (DPC) Clausthal. Due to the steep reflectors in the data, the conventional processing methods were unsuccessful and a new stacking method, during which only envelopes of the seismic traces are being stacked (Stiller, 1992), had to be applied to the dataset. The envelope stack offers a simplified overview of the main structures in the underground of the KTB site.

Smoothed apparent dips were used for a simplified 3-D horizon migration of travel times for specific horizons (Stiller & Tormann, 1992). This migration allowed a first interpretation of the geological settings of the site.

For migration a 3-D phase stack has been produced on the basis of the interpretation of the envelope stack, including the velocity models which have been set up using near surface information. Because of the sparsely sampled data, areas of strong lateral velocity gradients and steep structures, a new algorithm using the summation or Kirchoff technique had to be developed. As Körbe et al. (1997) describes, the summation migration provided better results than other migration techniques.

Provided by the GFZ Potsdam, this 3-D seismic data cube was the main dataset used for interpretation and development of new and improved geophysical methods for geothermal reservoir assessment.

If we examine one sample inline cross-section (SW-NE direction) selected from the 3-D dataset (Fig. 3.1), we can identify the following main structures: in the upper 3000 m SW of the measured area, the seismic image reflects subhorizontal layers of the foreland sediments, offering very good structural information. On the contrary, only poor structural information is available in the case of the granitic body laying to the NE of the KTB borehole. Falkenberg granites reach to about 6000 m or 7000 m depth according to gravity modelling, however the lower borderline can hardly be spotted in the seismic data. In the central area, the seismic image revealed numerous faults and shifts of various angles and reflection amplitudes. The steeply inclined (with dips between 50° – 60°), into the NE dipping elements can be tracked throughout the whole 3-D dataset, from the surface till depths of almost 10 km. These main reflectors are directly linked to the Franconian Lineament at the surface (Harjes et al., 1997). This group of major faults, named SE (seismic events) possibly plays a significant role in the fluid movement and is thus significant for hydrothermal simulations of the area. The Erbendorf body, which can also be identified in the cross-sections, is a structure of high reflectivity with the upper boundary in 10 km depth. Such depths are not relevant in a survey with a geothermal focus and thus the presence of the Erbendorf body has been taken into account only superficially.

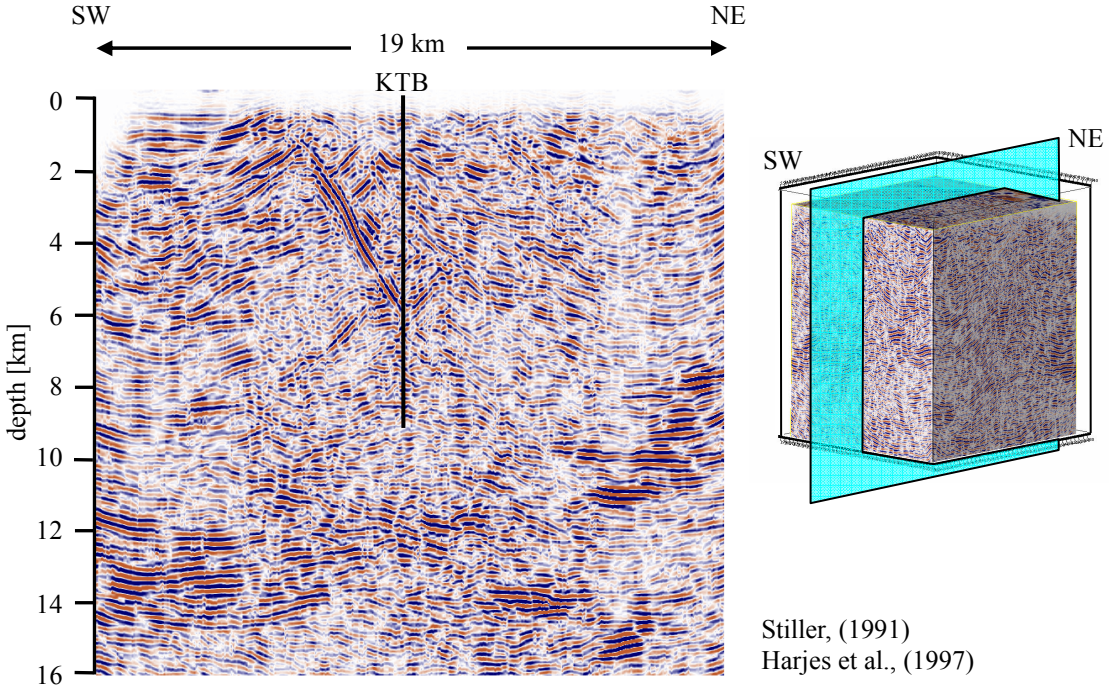

Fig. 3.1: *A sample cross-section (depth migrated) of the 3-D data volume recorded during the ISO89 campaign. The vertical black line represents the section penetrated by the KTB-HB borehole. Figure on the right shows the whole 3-D data cube with the position of the sample cross-section.*

3.2 2-D Seismic Profile KTB 8502

The 2-D KTB 8502 line, the second available seismic dataset from the KTB area, was used mainly for comparison purposes. It has been recorded during the time period from 1984 till 1997 along with five other 2-D reflection seismic lines (KTB 85) and the longer DEKORP 4 profile during the DEKORP (Das Deutsche Kontinentale Reflexionsseismische Programm) measure campaign. As part of the KTB pre-site survey, the measurements were conducted prior to the ISO89 3-D reflection seismic survey. KTB 8502 is crossing the area of interest in the SW-NE direction, parallel to the direction of the 3-D seismic dataset inline profiles. Passing almost exactly through the location of the KTB-HB borehole (Fig. 2.3), it might be considered as the spatial equivalent of the Inline 368 (Fig. 3.1).

The 50.48 km long seismic line has a sampling rate of 4 ms and reached up to 100-fold coverage. The data were recorded with Vibroseis, the sweep length was 20s and the sweep-range 12-48 Hz which resulted in a source wavelet same as was used during the 3-D ISO89 measuring campaign. Data used for the work on the presented topic were processed at the DEKORP Processing Center and offer a time migrated picture comparable with the time migrated data of the 3-D seismic block. Geological and tectonic structures illuminated by the KTB 8502 profile correspond very closely to those described above, in the Chapter 3.1.

3.3 Borehole Measurements at the KTB

Surveys and loggings done directly inside a borehole offer the most reliable and precise information about deep underground rock. The KTB database provides an exceptional amount of high-quality data from numerous experiments carried out in two deep drillholes (Tab. 3.1).

Tab. 3.1: *Basic information about the two KTB boreholes, the pilot hole (KTB-VB) and the main hole (KTB-HB) (Wilhelm, 2000).*

	latitude	**longitude**	**elevation [m]**	**depth [m]**	**open hole [m]**
KTB-VB	N49°48'59.0''	E12°7'10.0''	513.4	4000.1	bottom 150
KTB-HB	N49°48'58.8''	E12°7'19.2''	513.8	9101	bottom 70

With the aim to bring new insight into properties of the deep continental crust and the undergoing processes, a superdeep exploration borehole has been sunk into the crystalline basement of the Oberpfalz as part of the German Continental Deep Drilling Program. In order to ensure the success of this project, a shallower pilot borehole preceding the main borehole has been realised. Apart from the fact that valuable information about the possible drilling techniques have been gathered, the 4000.1 m deep pilot hole (KTB-VB) served as source of 3564 m excellent quality cores and various logging experiments. This fact reduced the need of coring and logging in the upper section of the main borehole (Emmermann & Lauterjung, 1997).

Drilling of the actual superdeep hole (KTB-HB) situated only about 200 m to the SE of KTB-VB, started in the year 1990. Due to technical difficulties and the unexpected rock characteristics at the deep section of the borehole, the aspired 10 km depth could not be reached. Drilling has been terminated in October 1994 at 9101 m depth, temperature ~265 °C and pressure ~240 MPa. Until the depth 7500 m, KTB-HB is practically vertical, but due to the considerable rock instabilities, the lowest part of the borehole reached a horizontal displacement of about 300 m (Emmermann & Lauterjung, 1997).

The scientific drillholes, both located in the Zone of Erbendorf-Vohenstrauß, provide continuous records of the penetrated crystalline rocks (Fig. 3.2). Even though the boreholes are only 200 m apart, their lithological profiles show considerable differences; a proof of the complex structure at the drill site. A wide spectrum of logging operations was carried out in the KTB boreholes, including the recording of acoustic, electric, nuclear, geochemical, magnetic and borehole imaging data (Draxler, 1990; Bram et al., 1991; Bram & Draxler, 1992, 1993, 1994).

The field laboratory established directly at the drill site enabled the collection of geoscientific data on cores, cuttings, rock flour, drilling fluids and gases and provided the opportunity to link downhole measurements with the petrographical and petrophysical features of the basement rock. This joint evaluation of downhole data and results of the field laboratory provided reliable information about the complex geological conditions of crystalline rocks (Pechnig et al., 1997).

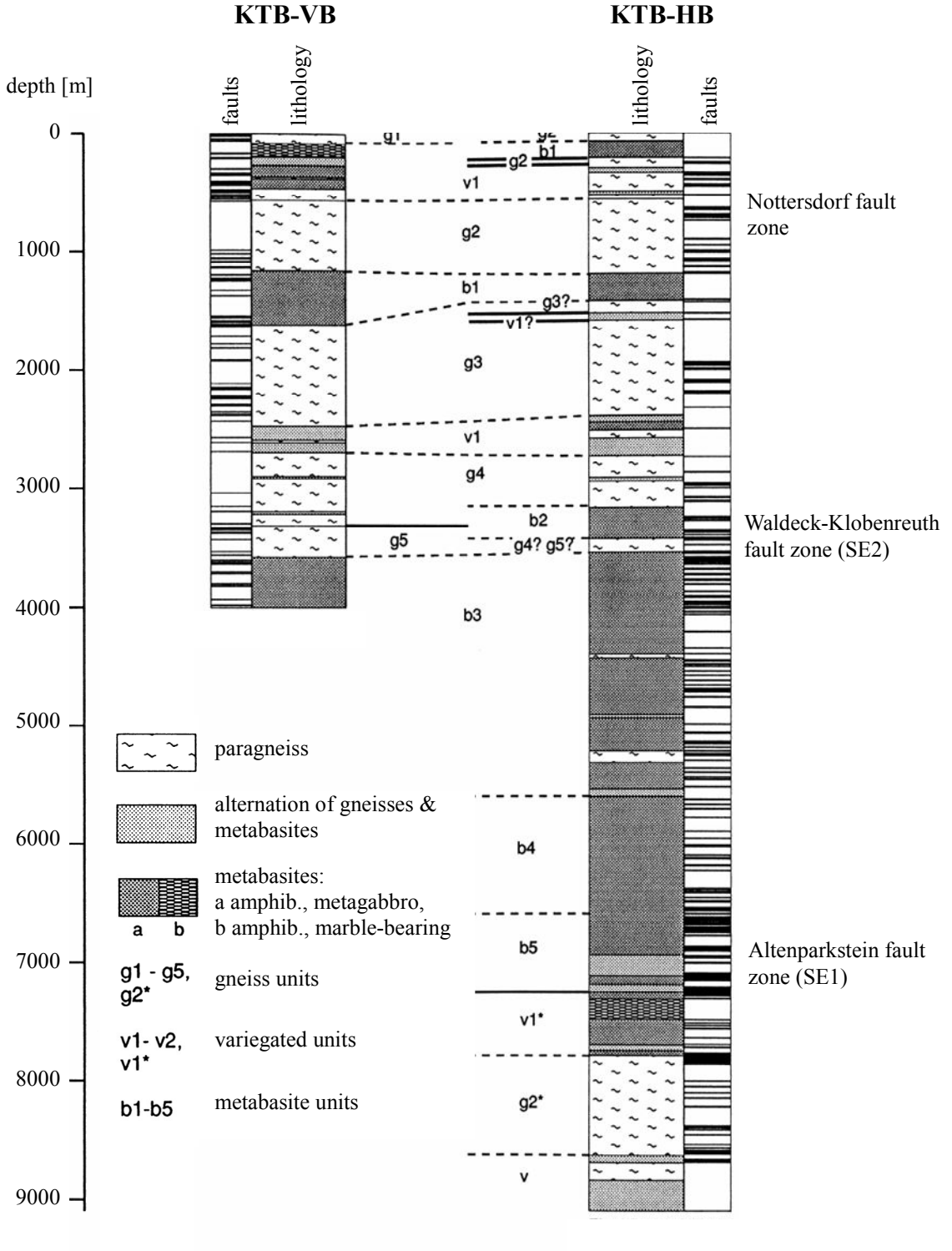

Fig. 3.2: *Simplified lithological profile of the KTB-VB (pilot hole) and the KTB-HB (main hole) (after Harjes et al., 1997).*

Bücker et al. (1990) and Soffel et al. (1992) list petrophysical properties available from the KTB-VB reaching to 4000 m depth. Properties from a depth interval reaching down to 9101 m known from the KTB-HB borehole have been published by Rauen and Winter (1995). Petrophysical properties measured and studied on the KTB-HB cores (Fig. 3.3) are the following (Emmermann et al., 1995):

- density
- magnetic susceptibility
- gamma-spectroscopy
- thermal conductivity
- ultrasonic measurements
- electrical resistivity
- porosity
- permeability
- internal surface

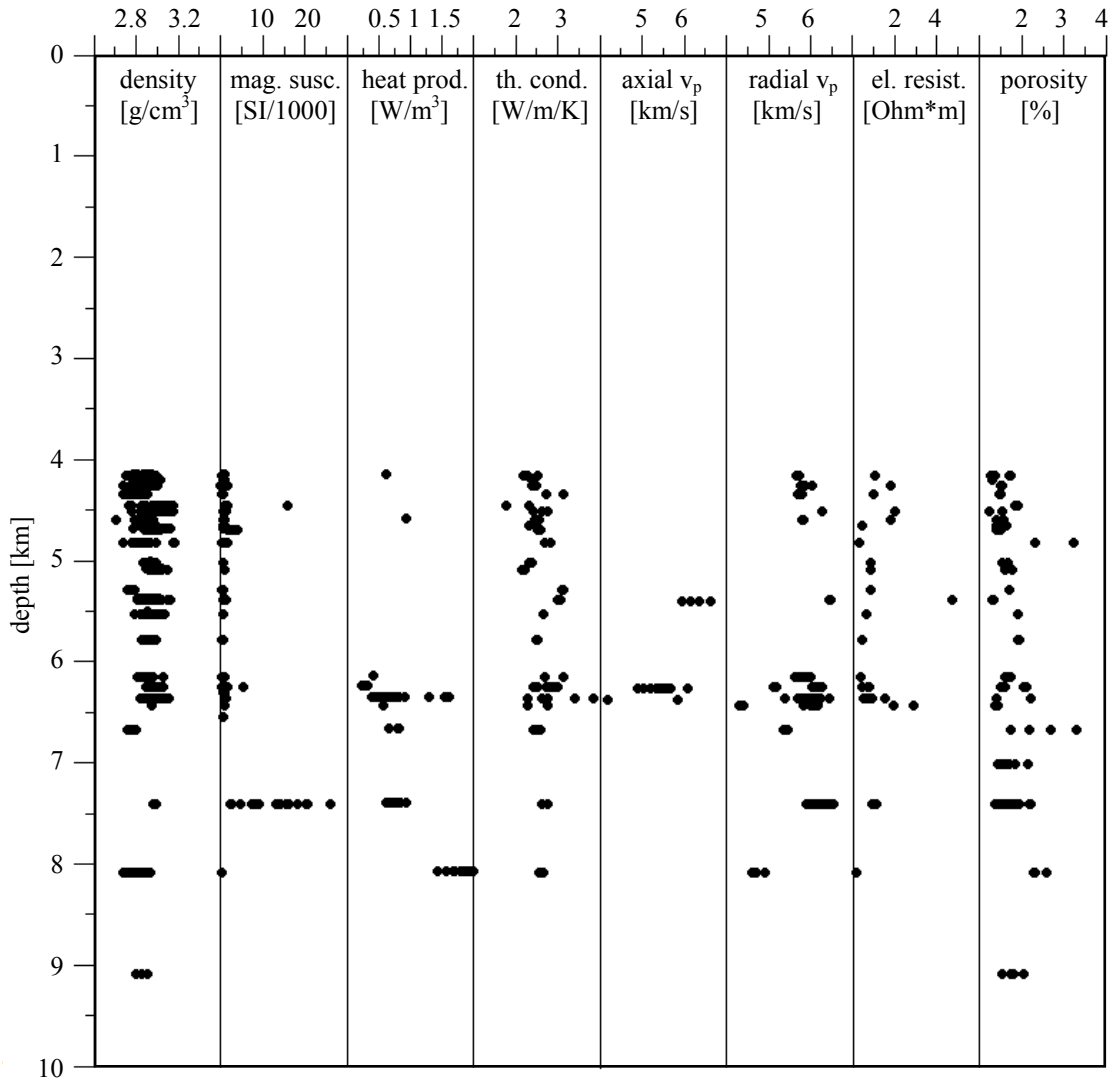

Fig. 3.3: *Some of the petrophysical properties measured on cores of the KTB main borehole.*

3.4 Summary

The German Continental Deep Drilling Program belongs to the largest scientific projects realised in Germany so far. From the great amount of data which has been gathered during the project period, only a small fraction is being processed and analysed within this thesis. The primary dataset, which is in the centre of the work, is the depth migrated 3-D reflection seismic dataset recorded in 1989 within the frame of the Integrated Seismic Oberpfalz (ISO89) survey. Covering the area of about 19 km x 19 km and reaching up to 16 km depth, this dataset provides a three-dimensional picture of the complex structures in the continental crystalline crust.

While a 3-D dataset offers a very good understanding of the complicated geology, a two-dimensional image of the area brings higher resolution, which due to the high financial costs is not possible at a three-dimensional spread. For this reason, we use the KTB8502 seismic profile recorded during investigations prior to the KTB project as a source of supplementary information. Both datasets have been processed and migrated by the DEKORP group in the DEKORP Processing Centre (DPC) Clausthal and were provided by the GFZ Potsdam.

While seismic data provide structural information, the downhole recordings performed in the two KTB boreholes offer a glimpse at the lithological composition of the penetrated rock and its properties. Together with the measurements done on cores, cuttings, rock flour, etc., these data are freely accessible at the GFZ Potsdam website.

Chapter 4

Lithological Units Identification

The ISO89 3-D reflection seismic dataset provides a very good image of the complicated geological and tectonic settings at the KTB site. From the analysed cross-sections it is obvious that numerous faults and fractures shifted the lithological blocks in different directions over different distances. To be able to work with the whole dataset, it had to be simplified by means of division into lithological units. As already described in Chapter 1, the main units at the site of the Continental Deep Drillhole are: the foreland Permo-Mesozoic sediments, granites (consisting mainly of the Falkenberg granite), the Erbendorf body, Zone of Erbendorf-Vohenstrauß (alternating layers of gneisses and metabasites), the fault zone and a unit of deep basement rocks.

4.1 Division of the Dataset into Main Lithological Units

The available seismic data alone did not provide sufficient information necessary for successful lithological unit identification in the complex geology of the KTB site. For this reason additional a priori information had to be taken into account.

The geological map of the KTB site's vicinity Oberpfalz (Geologische Karte des KTB-Umfeldes Oberpfalz 1:50 000) is a reliable source for the location of lithological units at the surface. Using coordinates defining the position of the 3-D seismic cross-sections, on-surface borderlines of the main lithological units have been transferred onto the network of inline and crossline seismic profiles. This meant a great help in the geological interpretation of the near-surface sections in the seismic dataset.

Downhole measurements, cores and cuttings from the two KTB deep drillholes provided input for the construction of continuous lithological profiles reaching from the surface to about 9000 m depth (Fig. 3.2). Both boreholes situated within the Zone of Erbendorf-Vohenstrauß show vertical and lateral variations of the gneissic and metabasic rocks, indicating the high structural complexity of the ZEV unit.

Hirschmann (1996) published a geological cross-section through the KTB site, in which he combined surface geology, findings from downhole measurements and seismic interpretation results (Fig. 4.1). This geological interpretation served as a kind of model or inspiration for the classification into different lithological units.

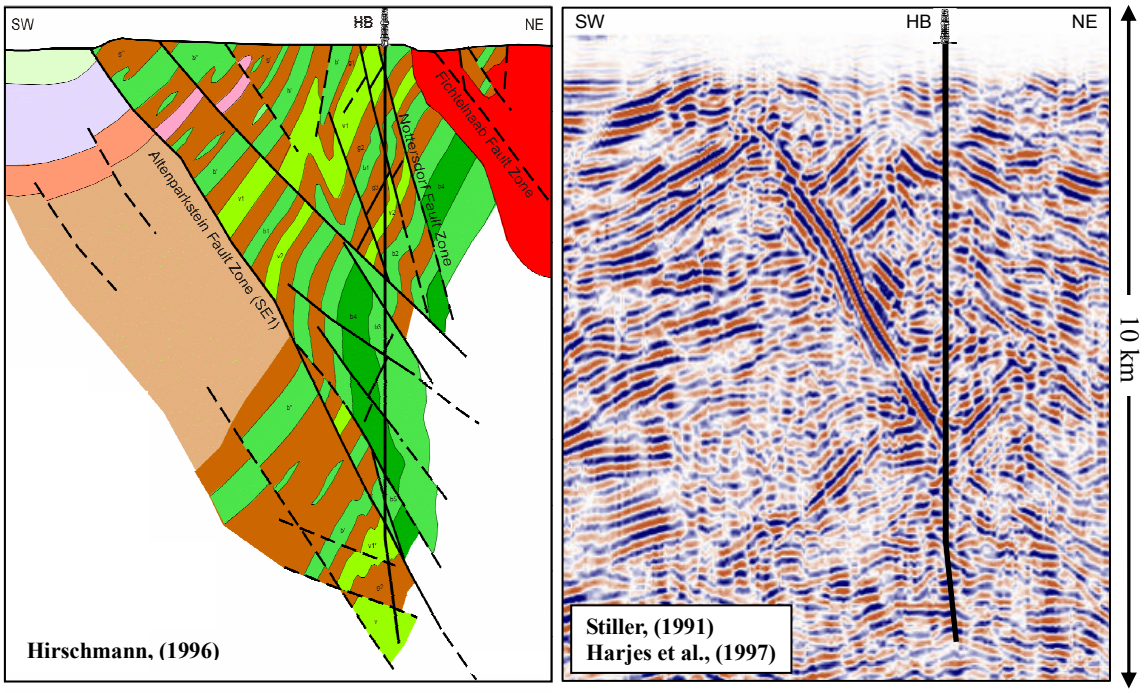

Legend:

- Upper Cretaceous
- Triassic
- Lower Permian
- Upper Carboniferous
- granites

ZEV:

- gneiss units
- variegated units
- amphibolite units
- amphibolite-metagabbro units
- undivided
- orthogneiss

Fig. 4.1: *Geological (left) and seismic (right) cross-section through the KTB site with the location of the KTB-HB borehole.*

All the above mentioned information has been combined and transferred to the 3-D seismic dataset to serve as guidelines during the rock zones identification process. Due to the complicated seismic image of the site, lithological units had to be identified and picked manually in a regular and dense grid. In order to keep the processing time of the considerable amount of data under an acceptable limit, only every 10^{th} profile has been processed in this way. The result is a database of point coordinates defining the outer surface of each lithological unit separately.

Triangulation of point clouds with the aim to construct unit surfaces was performed using the Cocone Software for surface reconstruction by Dey & Goswami (2003). This program basically uses picked points as vertices for the calculation of Delaunay triangles which together form the surface of a body.

The fact that different rock units are isolated by a surface, allows us to handle them as separate, independent bodies. Each of the bodies received a "rock identification number" as listed in Table 4.1 and shown in Figure 4.2. All lithological units were filled out with grid points on a regular equidistant grid, uniting the independently standing units again into one 3-D block.

Tab. 4.1: *Identification numbers of lithological units at the KTB site.*

rock identification number	**1**	**2**	**3**	**4**	**5**	**6**
lithological unit	sediments	fault zone	granites	Erbendorf body	ZEV	middle crust

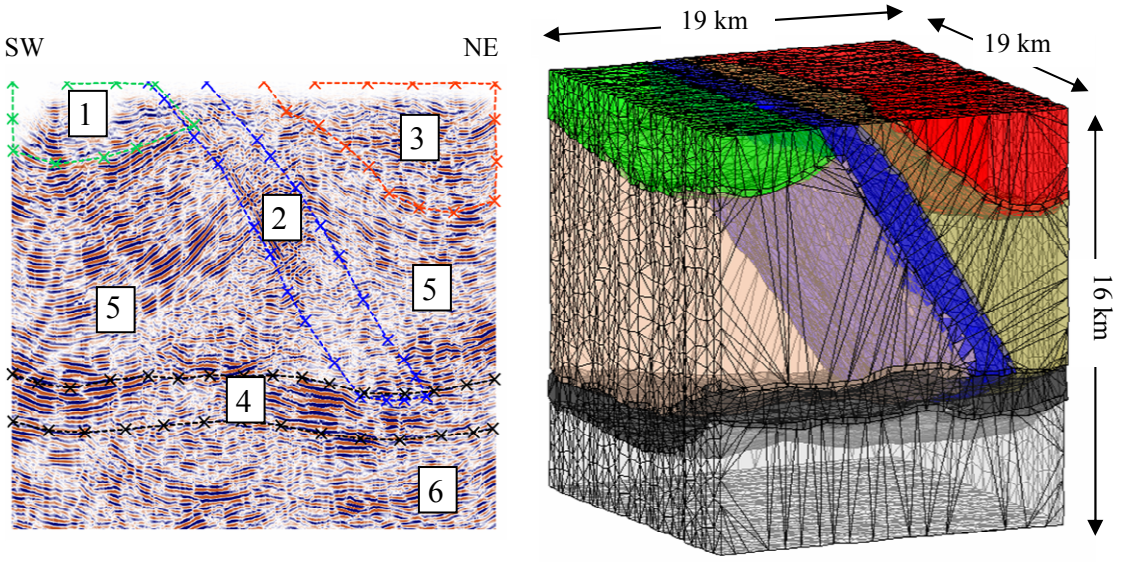

Fig. 4.2: *Lithological units identified at the KTB site projected onto a seismic cross-section (left) and the triangulated surfaces of the units forming the complete volume of the data block (right).*

4.2 Zone of Erbendorf-Vohenstrauß

After simplifying the geological situation at the KTB site, we can claim that except of the sedimentary unit in the SW, the granitic unit in the NE, the area consists mainly of the large ZEV unit, in other words, of alternating gneisses and metabasites (Fig. 2.1 & Fig. 4.1) (Pechnig et al., 1997). If we shall think of the KTB site as of a geothermal reservoir, the ZEV will become the lithological unit of interest and the zone in which the main hydro-geothermal processes take place. For this reason, compared to the other lithological units, the complex ZEV unit has to be treated in much more detail.

Distribution of thermal conductivities and heat productions measured in the KTB-HB borehole shows a clear bimodal behaviour (Fig. 4.3) reflecting the different thermal properties of the penetrated gneisses and metabasites. Knowledge about the position of gneiss and metabasit layers, or their accumulations within the data cube, might prove to be valuable during the process of hydrothermal modelling.

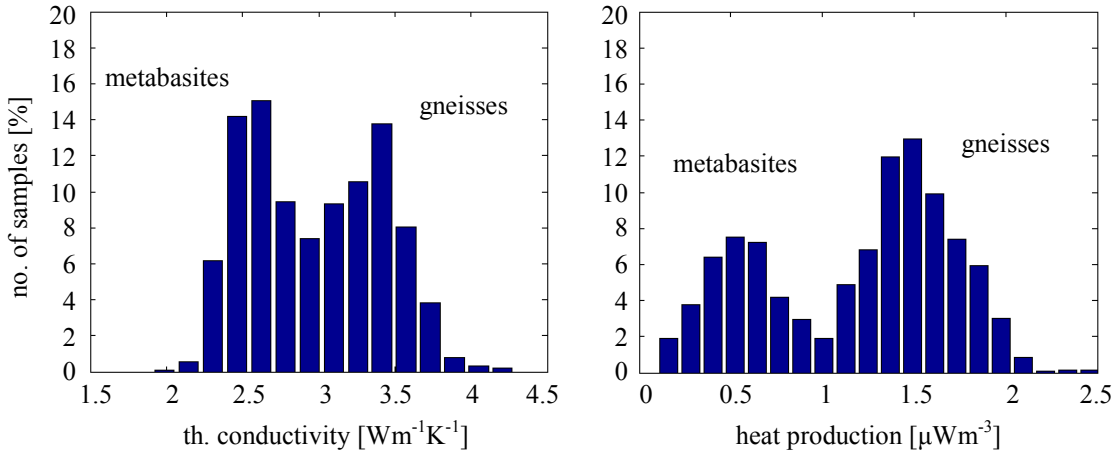

Fig. 4.3: *Thermal conductivity and heat production distribution within the ZEV unit penetrated by the KTB-HB. The bimodal behaviour can be explained by the presence of two different rock units: metabasites with lower values of thermal conductivity and heat production, gneisses with higher values.*

Logging performed at the KTB site brought highly accurate information about rocks penetrated by the boreholes and their close vicinity. In order to build a link between borehole information and the whole 3-D dataset, synthetic seismograms have been calculated using routines available within the Seismic Unix open source package (Fig. 4.4). 20 000 models of alternating gneiss and metabasit layers with different thicknesses, densities and compressional velocities have been generated on the basis of the Monte Carlo method. Intervals, from which density and velocity values were taken, were defined on the basis of log data gathered in the KTB-HB.

Reflection coefficients calculated for the different lithological models were subsequently convolved with a wavelet of the following characteristics:

sampling rate	4 ms
sweep	12 – 48 Hz upsweep
sweep length	20 s

In order to obtain synthetic traces correlating highly with the measured seismic traces, the used wavelet has the exact properties of the source signal used during the ISO89 campaign.

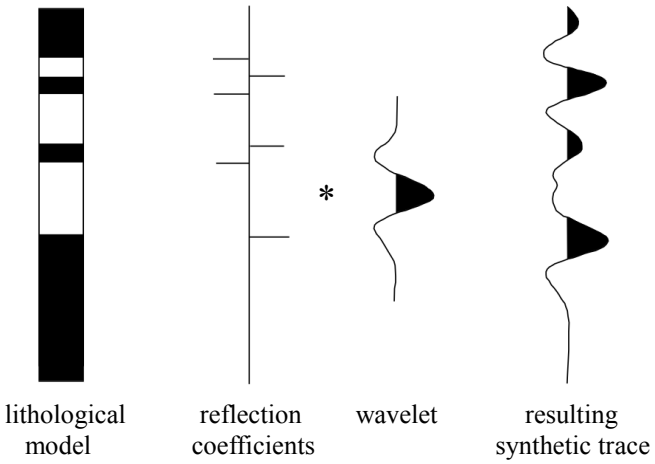

Fig. 4.4: *Schematic depiction of the process of synthetic trace calculation.*

After convolution with the source wavelet, a data base containing 20 000 synthetic traces of the length 1000 m was prepared for further processing. Likewise, all traces of the original measured dataset were split into 1000 m long segments, while still retaining the exact position coordinates. Each of the original traces has been compared with each of the synthetic traces with the aim to find the counterpart with the highest cross-correlation coefficient. During this time taking procedure synthetic traces with the highest correlation coefficients were thoroughly selected and placed into the correct position to assemble synthetic seismic sections (Fig. 4.5b).

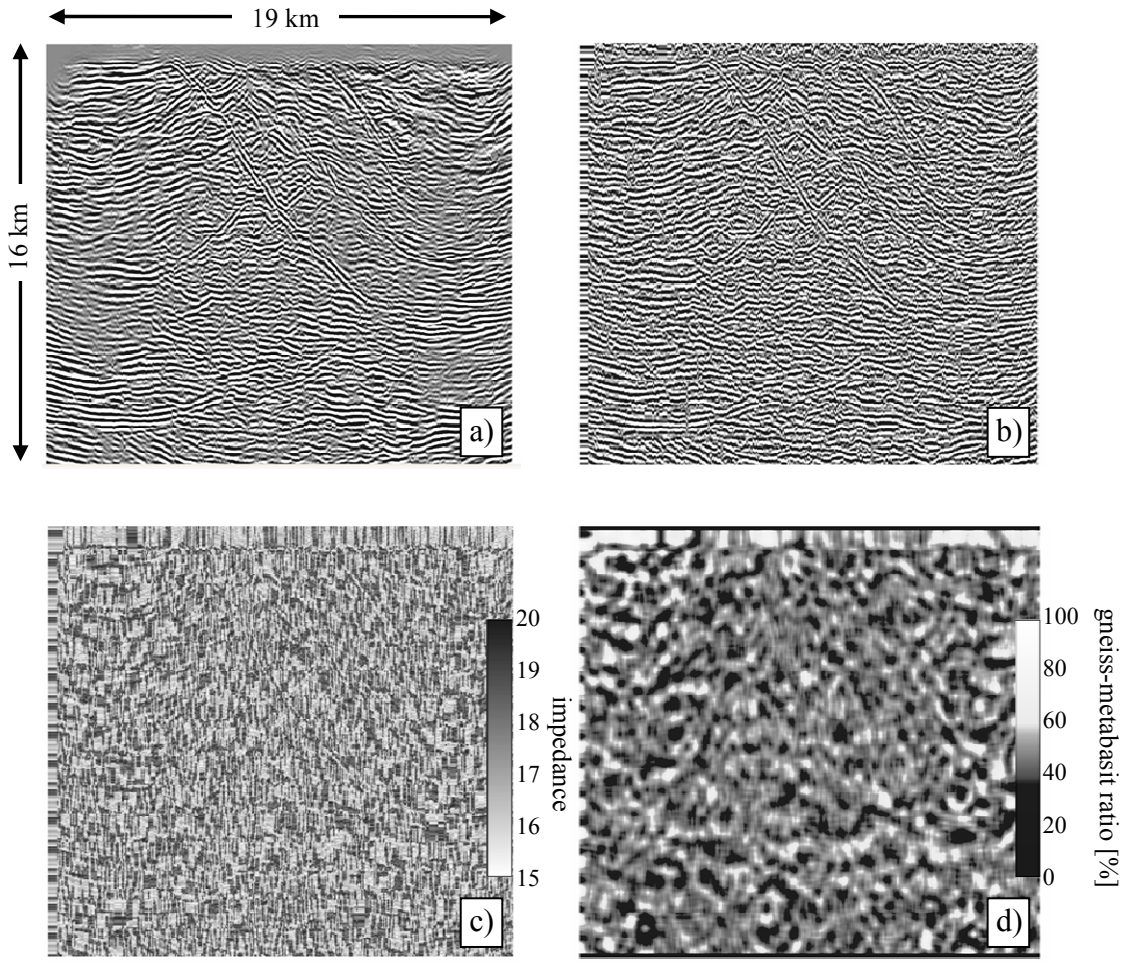

Fig. 4.5: *a) original measured seismic cross-section b) the corresponding synthetic cross-section c) impedance calculated from the parenting lithological models d) gneiss-metabasite ratio.*

Quality of the synthetic dataset is given by the value of the cross-correlation coefficient. As seen in Figure 4.6, distribution of cross-correlation coefficients is Gaussian with the peak at the value 0.89. This shows a very good similarity of measured and synthetic traces.

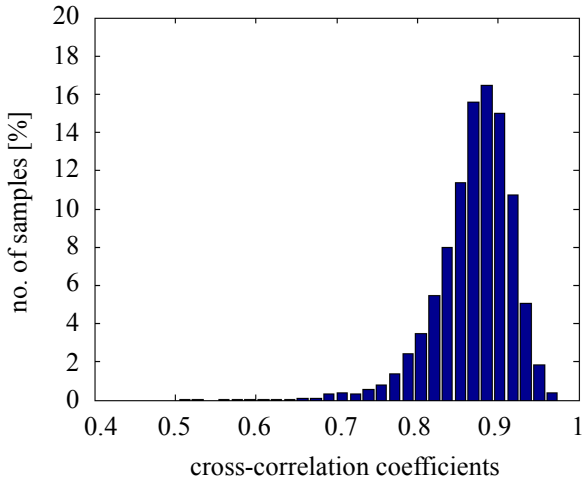

Fig. 4.6: *Distribution of cross-correlation coefficients between original traces and the best synthetic traces adopted for synthetic cross-sections.*

The link between synthetic traces and parenting lithological models still remains. This means that the produced synthetic sections not only carry the information of possible local lithology: position of gneissic and metabasic rock (Fig. 4.5d) in the whole volume of the site, but also give an overview of rock thermal properties (thermal conductivity, heat production).

Tests on core samples performed under simulated in-situ conditions show a high value of anisotropy concerning the thermal conductivity of gneissic rocks. Anisotropy caused by the rock structure: distinct foliation and lineation, leads to high values in the direction parallel to foliation and low thermal conductivities perpendicular to foliation. The average difference of values between parallel and perpendicular to foliation obtained in the KTB-field laboratory is 20% (Huenges et al., 1990). Considering this information, we separate the identified gneissic rocks according to their dip into three groups:

gneiss steep
gneiss intermediate
gneiss near-horizontal

and assign them different absolute values of thermal conductivity with respect to their foliation axes.

4.3 Summary

Simplified perception of the KTB site results in the definition of only six main lithological units. While seismic cross-sections give a clear image about the extent of Permo-Mesozoic sediments, identification of the granitic unit required more effort. The Erbendorf body lying in depths higher than 10 km, together with the underlying middle crust have been analysed only superficially, because of their minor contribution to the treated topic.

Zone of Erbendorf-Vohenstrauß is filling out the majority of the site's volume and represents the lithological unit in which hydrothermal processes of interest take place. For this reason, the ZEV has been analysed in much more detail compared to the previously mentioned units. It has been subdivided into the two main components: gneisses and metabasites. Joint analysis of seismic cross-sections and borehole data enabled the calculation of synthetic seismograms, which give an overview about the location of the particular layers within the ZEV. Due to the considerable differences in rock thermal properties, this processing step yields important input required for coupled hydrothermal simulations.

Thermal conductivity of gneisses is due to the pronounced foliation highly anisotropic. We combine the determined gneiss locations with dip calculations (Chapter 5.1.2) and define three gneissic subgroups. According to the specific foliation orientation, different values of thermal conductivity can be assigned to the subgroups.

Apart of the ZEV, also the other main lithological units were picked and their surfaces triangulated so that processing could continue on separate bodies designated by identification numbers.

Chapter 5

Faults and Fractures Identification

In the process of structural model construction, identification and spatial orientation of faults and fractures is one of the essential steps. Especially if hydraulic and thermal modelling is aspired, understanding of the flow pattern within the underground is crucial. Since porosities and permeabilities of crystalline rock are too low to enable fluid flow through the natural pores of the rock matrix, fluids tend to migrate through cracks and fractures. The term fracture is explained by Sausse et al. (2008) as two smooth and parallel planes separated by a constant hydraulic aperture.

The crystalline rock of the KTB site incorporates a vast amount of cracks, faults and fissures of different scales (Fig. 5.1). The main tectonic feature, the already mentioned Franconian Lineament, which is crossing the area in a NW-SE direction, is actually a bundle of large-scale faults with a significant downward continuation. This zone was crossed by the KTB-HB borehole in the depth interval 6850 m to 7260 m and in the seismic data it can be followed even up to depths of about 10 km. In order to track the structure's three-dimensionality, 3-D reflection seismic measurements were required. The geological history of the Franconian Lineament, or the so called SE reflectors, has been described in more detail in Chapter 2.

While closely examining the available 3-D seismic cross-sections, the question concerning the linear structures with zero and close to zero amplitudes and zones of low reflectivity comes up. The linear structures seem to be associated with a shift of layers which would suggest the presence of a fault. If these fractures prove to be real, they will belong to another group of faults, of a middle-scale. Investigation whether these alleged fractures are real or just residuals of processing applied to the data, was a part of this thesis.

Fractures smaller than one wavelength belong to the site's fracture inventory as well, but because of their size, they can not be detected in the seismic cross-sections and therefore their interpretation is not included in this work.

Fault systems of diverse scales and characteristics require individualised approaches of identification. Also, due to the huge amount of tectonic structures in the data, a special focus had to be put on the automatisation of the fracture detection process.

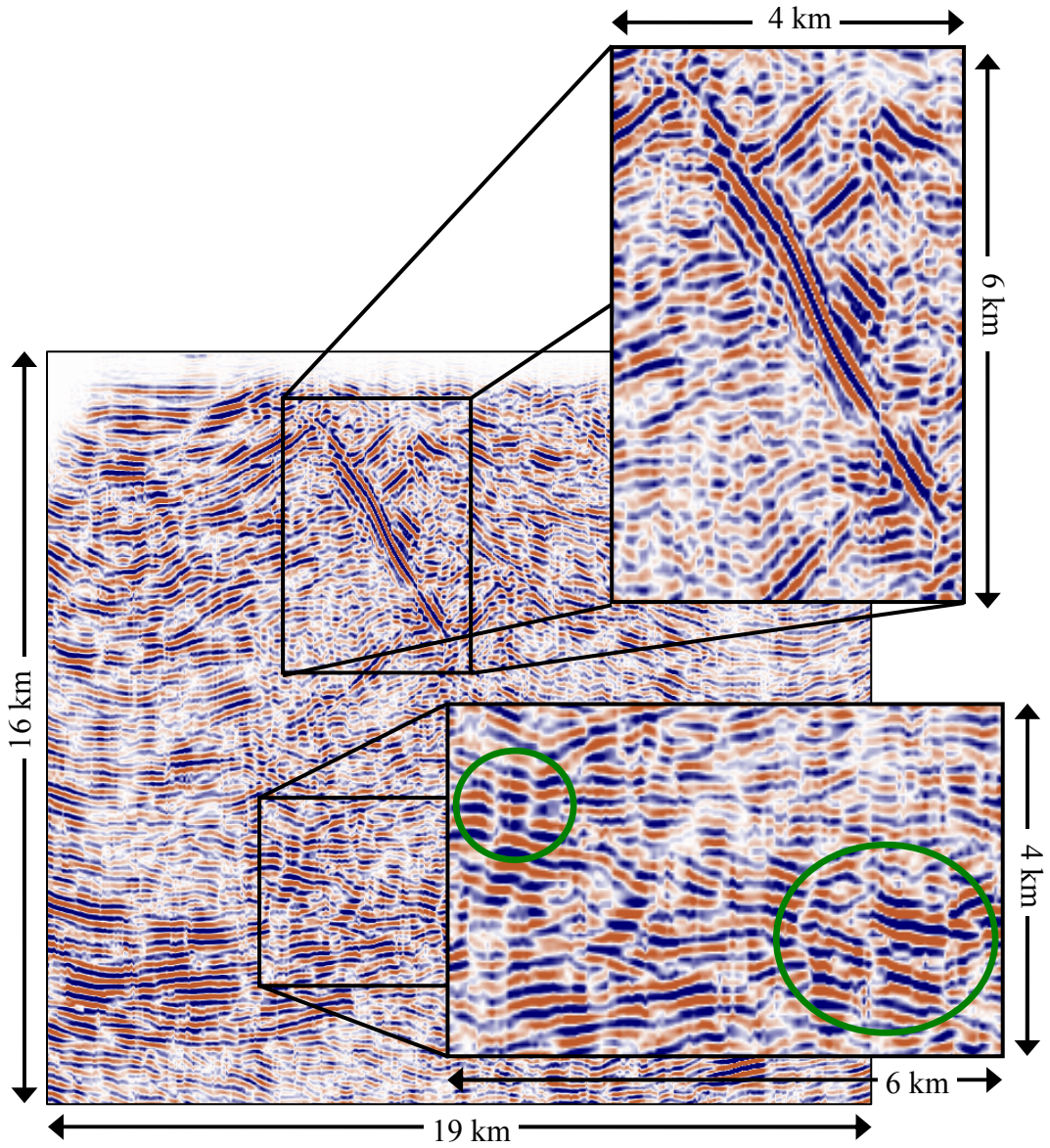

Fig. 5.1: *Seismic section displaying fault zones of two different scales. a) the large-scale fault zone (SE1 reflector) b) the possible middle-scale fractures, best examples are denoted by the green circles.*

5.1 Large-scale Faults

The major fault system of the KTB site is related directly to the Franconian Lineament. Because of the significant size and extent, this fault zone can play an important role in the flow of hot fluids within the crystalline rocks. Precise structure identification is necessary in order to include this fault system into the structural model of the site.

As seen on the seismic sections, the SE1 reflector, which is the most pronounced fault of the Franconian Lineament fault system, is not a mere shift of horizons, it itself can be considered as a seismic event. While the SE1 reflector is intersecting the whole dataset and is visible on all cross-sections, the other reflectors belonging to the fault system are less dominant and can be identified only on particular profiles. Already to the bare eye it is obvious that the reflectors have a unique dip if compared to the surrounding structures. This typical and distinct dip of faults belonging to the Franconian Lineament, allowed a dip calculation based processing.

5.1.1 Wavenumber – Wavenumber (k-k) Filtering

Particular events which are characterised by a unique dip can often be more easily identified in the *f-k* domain. Normally, seismic data are available in the form of time-distance (*t-x*) profiles, or if depth migrated, in depth-distance (*z-x*) profiles. In order to take advantage of the *f-k* domain, these data need to be transformed. The tool to do this is the two-dimensional Fourier transform. When applying a two-dimensional Fourier transform to a *t-x* dataset, the time axis is transformed into frequency (*f*) and the distance axis becomes the wavenumber (*k*) axis (Yilmaz, 2001). The Fourier transform is decomposing the input *t-x* data into a series of lines, which are mapped to straight lines in the *f-k* space. Therefore, an unwanted range of dips can be identified in the *f-k* space, suppressed by muting and the data can be inverse transformed back to the *t-x* domain for further processing or interpretation.

We usually talk about the *f-k* domain and *f-k* filtering, because normally, the seismic data are available in the form of time-distance profiles. Occasionally, seismic data in the form of depth-distance are available. This is also the case of the seismic data of the KTB site which are being analysed within this work. These depth-migrated data are Fourier transformed into the wavenumber-wavenumber (*k-k*) domain.

Applied to the KTB data was the 2-D Fourier transform incorporated in the commercial seismic data processing software GEDCO VISTA®. After a thorough viewing of the seismic cross-sections and their *k-k* spectra, one spectrum has been selected as representative. This spectrum and the corresponding seismic cross-section are plotted in the Figure 5.2. As seen, the majority of the features exhibit a sub-horizontal dip and in the *k-k* spectra are plotted in a range near *k=0*. The inclined large-scale faults can be easily sorted out from the rest of the events. A filter which mutes all unwanted events and leaves only the desired structures was then constructed and applied to the dataset. In this case, the only desired structures are the large-scale fault and all other events can be considered as unwanted. The filter was applied consecutively on each of the cross-sections of the KTB seismic dataset.

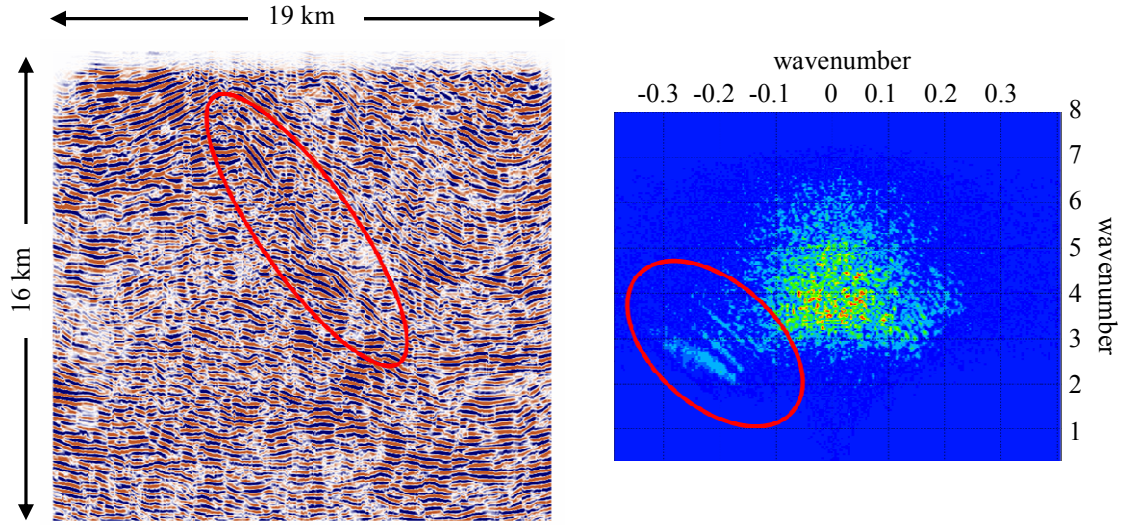

Fig. 5.2: *Seismic data in the offset-depth domain and the corresponding k-k spectra. The red ellipse depicts the position of large-scale faults.*

Finally, the inverse Fourier transform, which brings the data back into the depth-distance domain, is the last step of the *k-k* filtering. The data before and after *k-k* filtering are plotted in the Figure 5.3a and 5.3b. As seen on Figure 5.3b, steeply dipping reflectors have been preserved, while the structure of the surrounding reflectors is significantly degraded.

Additional envelope calculations strengthen the compactness of the fault image and enable a simple data value classification. Values outside a defined interval were substituted by a single value representing the unbroken background and received the white colour in the colour scale. Values inside the defined interval, representing the faults are plotted in black. This simple binary coding gives a clear statement about the position of the fault system belonging to the large-scale set of faults (Fig. 5.3c).

5.1.2 Dip Calculations

Another way to make use of the unique dip of the large-scale fault system is to calculate dips throughout the whole dataset and then extract only the values which agree with the dip of the SE reflectors.

From the numerous methods of dip calculations, we chose the structural tensor (*ST*) approach (Jahne & Hausbecker, 2000). Luo et al. (2006) showed how a structural tensor method improved by a data-adaptive weighting function can be used for calculations of dips and azimuths in seismic data. The mentioned weighting function was added to avoid erratic dips and uninterpretable orientations which might result from structural tensor calculations in noisy data or complex geology. The term “complex” is appropriate also for the description of the geologic situation at the KTB site and thus the weighted *ST* method seems to be suitable.

In order to compute the structural tensor, firstly the gradient vector *V(Vx,Vy,Vz)* at every sample of the dataset has to be calculated. Then, the structural tensor is constructed as follows

$$ST = \begin{bmatrix} \sum VxVx & \sum VxVy & \sum VxVz \\ \sum VyVx & \sum VyVy & \sum VyVz \\ \sum VzVx & \sum VzVy & \sum VzVz \end{bmatrix}. \tag{5.1}$$

With a summation in a 3-D moving window, already the first smoothing of the elements is performed. The problems which arise in complicated datasets are the unstable gradient directions. For such data, conventional smoothing methods might not be successful and the resulting dips are scattered and unrealistic. Luo et al. (2006) recommended using an additional weighting function (*w*), which would overcome the instability associated with gradient directions. The weighted structural tensor is then calculated with (Luo et al., 2006)

$$ST = \begin{bmatrix} \sum wVxVx & \sum wVxVy & \sum wVxVz \\ \sum wVyVx & \sum wVyVy & \sum wVyVz \\ \sum wVzVx & \sum wVzVy & \sum wVzVz \end{bmatrix}. \tag{5.2}$$

Here, *w* is the weighting function, calculated as squared power of complex traces:

$$w = \left(R^2 + I^2\right)^2. \tag{5.3}$$

R	real part of a complex trace (seismic amplitude)
I	imaginary part of a complex trace (Hilbert transform)
$V(Vx,Vy,Vz)$	gradient vector.

The weighting factor, which is due to its definition data dependent, increases the signal/noise ratio of the whole dataset.

After calculating the eigenvalues of the weighted ST, we select the largest eigenvalue and calculate its eigenvector. This eigenvector is actually the normal to the particular seismic event. In this way, we directly obtain the size of dips at every point of the data volume.

Figure 5.3c shows the result of dip calculation with the weighted structural tensor method applied to the KTB dataset. Same as in the case of the *k-k* filtering method, an additional envelope calculation gives a more compact picture. With the aim to depict only the large-scale faults, we perform a restriction of unwanted dip values. Again, we aim to obtain a simple binary system and separate therefore the data into the unbroken background and faults.

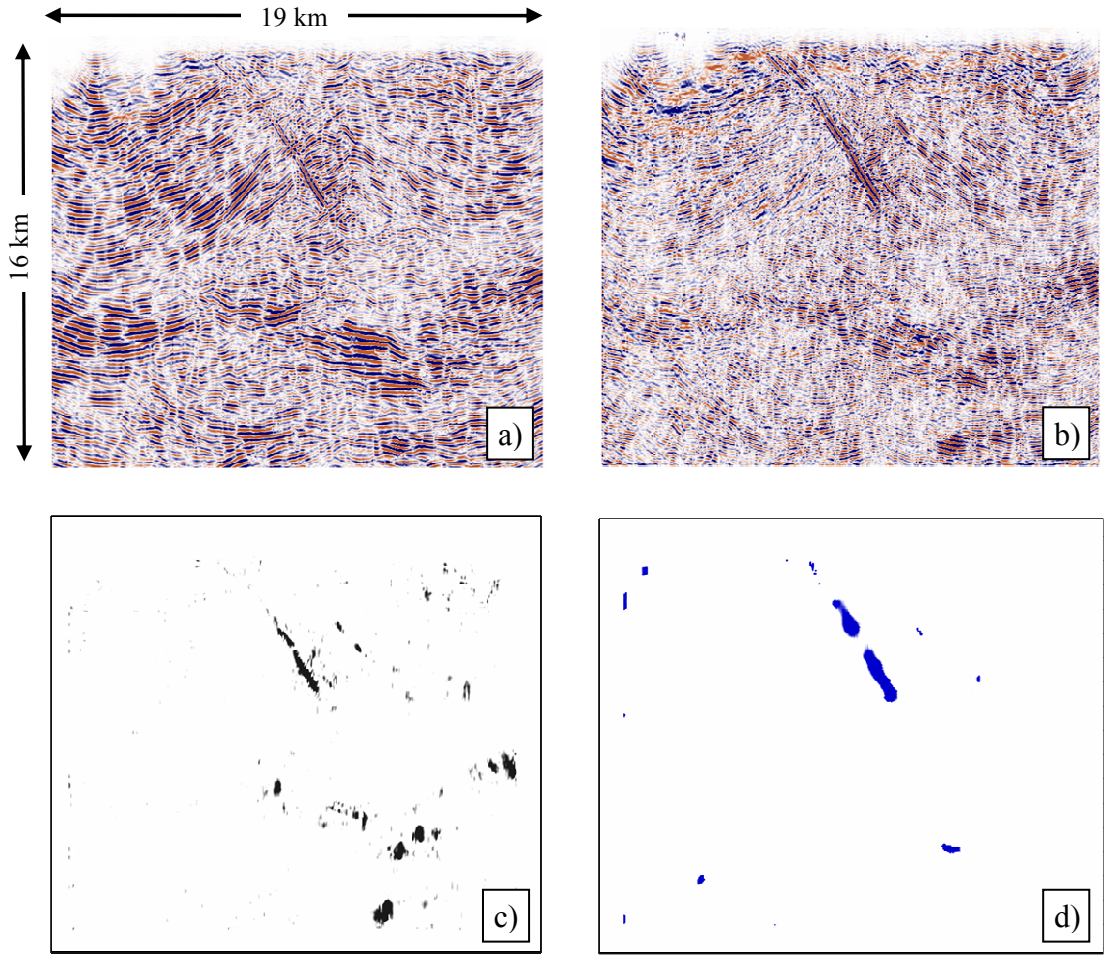

Fig. 5.3: *Identification of the large-scale faults. a) original measured seismic data, b) k-k filtered data, c) envelopes of the k-k filtered data, d) envelopes of the dip calculation.*

Results of both described fault identification methods give comparably satisfying results. While the *k-k* filtering is making use of 2-D sections, the dip calculations with the help of weighted structural tensor is taking advantage of the three-dimensional data. Combination of both results gives the most reliable information about the location of the large-scale fault system.

Of course, with the dip analysis approach, only the structures with the dip lying within the chosen interval were identified. Sections, where the large-scale faults are being intersected by horizons or structures of a different dip and thus interrupt the fault's continuity, cause the formation of gaps also in the results of the dip calculation.

5.2 Middle-scale Faults (Log-Gabor Filtering)

While there is no doubt that large-scale faults linked to the Franconian Lineament are in fact intersecting the KTB site, the fractures which were within this work classified as middle-scaled (Fig. 5.1), might be described as questionable. While this chapter covers the identification and the following separation of the middle-scale fractures from the rest of the data, attempts to determine their plausibility are described in the verification section (Chapter 5.3).

We firstly make the assumption that the zero amplitude linear structures really indicate cracks. Due to the considerable amount of these fractures in the dataset, a manual identification approach is not possible. Properly chosen filtering process is a better choice. From the tested methods, the best results have been achieved with the application of log-Gabor filters.

In the field of image processing, the Gabor filters are known already since 1980. They proved to be useful in different image processing applications, such as fingerprints, iris and face recognition, image coding, texture segmentation etc. (e.g., Field, 1987; Kovesi, 1999; Kruizinga & Petkov, 1999; Grigorescu et al., 2002; Cook et al., 2006). Gabor filters are basically band-pass filters with an adjustable centre frequency, orientation and bandwith. If properly adjusted, they react strongly to specifically oriented structures and weakly to all others (Levesque, 2000). This ability makes the Gabor filters suitable also for faults identification in seismic datasets (Admasu & Tönnies, 2005; Admasu, 2008).

Consider the image of the letters CAU (Christian-Albrechts University) shown in Figure 5.4a. Application of a horizontally oriented Gabor filter to this image results in a strong response to its horizontal features and at the same time, there will not be any response to the vertical elements. The result of horizontal filtering is seen in Figure 5.4b. If a vertical Gabor filter is applied to the same image, vertical features will be highlighted, while the horizontal ones will be neglected (Fig. 5.4d). The filter can be constructed in every desired direction. In order to highlight the inclined structures, it is necessary to construct a filter with the same angle as is the angle of the particular inclined element (Fig. 5.4c). It is also possible to construct a so called bank of Gabor filters consisting of several filters of various directions. Application of such filter banks captures features inclined with the defined angles (Fig. 5.4e).

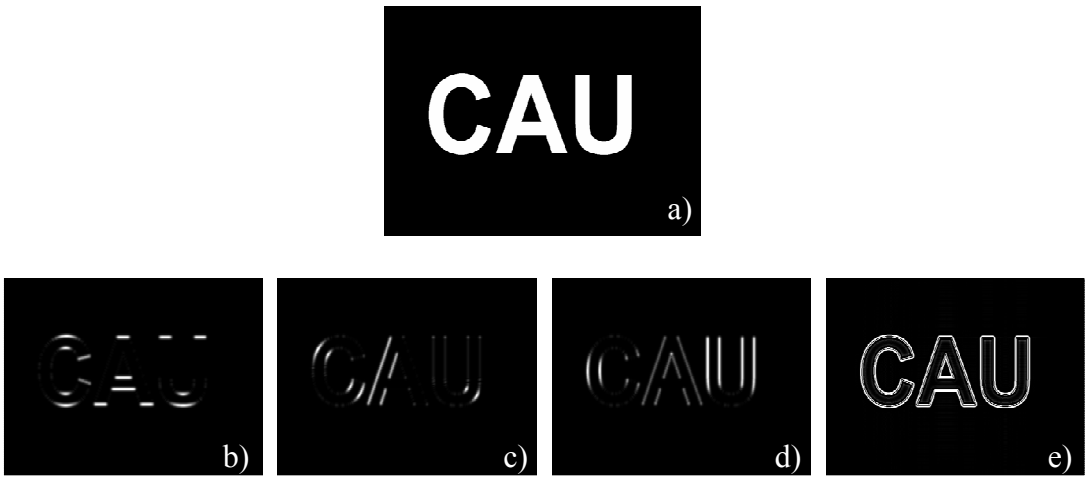

Fig. 5.4: *An example of log-Gabor filter application. The sample figure a) was filtered with log-Gabor filters of the following directions: b) horizontal, c) diagonal, d) vertical and e) a bank of filters including all possible directions.*

The Gabor filter is composed of two main components: the complex sinusoidal carrier and the Gaussian envelope which modulates its amplitude (Field, 1987)

$$g_{\lambda,\theta,\varphi,\gamma}(x,y) = \exp\left(-\frac{x'^2+\gamma^2 y'^2}{2\sigma^2}\right)\cos\left(2\pi\frac{x'}{\lambda}+\varphi\right) \tag{5.4}$$

$$x' = x\cos\theta + y\sin\theta$$
$$y' = -x\sin\theta + y\cos\theta\,.$$

The following parameters need to be specified for the application of a Gabor function:

λ wavelength
θ orientation of the filter
φ phase offset (calculated from the wavelength and bandwidth & determines the symmetry)
γ spatial aspect ratio (ellipticity)
σ standard deviation

A Gabor filter bank, incorporating all filter orientations has been applied to the KTB dataset with the aim to enhance the middle-scale fractures (Fig. 5.5b). After an inversion of the colour scale, the fracture network becomes clearly visible even though rests of unwanted structures are still present in the data (Fig. 5.5c). These structures, mainly rests of horizons were eliminated by additional image processing methods, such as thin subhorizontal line detection and elimination.

As seen in Figure 5.5d, which shows the final stage of the middle-scale fault detection, the resulting data do not include only linear fractures, but also wider "spots". This is not necessarily a failure of the method. The fact that these structures have also been detected with the above described filtering only shows that they have same or similar characteristics as the linear structures. With this kind of approach we possibly detected areas of destroyed structure and comparable petrophysical characteristics as those of the middle-scale fractures.

During the following work, may it be for further processing or simply for plotting of the fractures, often data in a skeletonised form (Fig. 5.6b) are being used. We obtained the skeleton of the dataset through "thinning" of the structures using the MATLAB ® image processing functions. With this method, the image (in our case a cross-section with the detected fractures) is being searched for objects of the width more than one pixel (sample). The outer pixels are then being removed during an iterative process until the object's width is only one pixel.

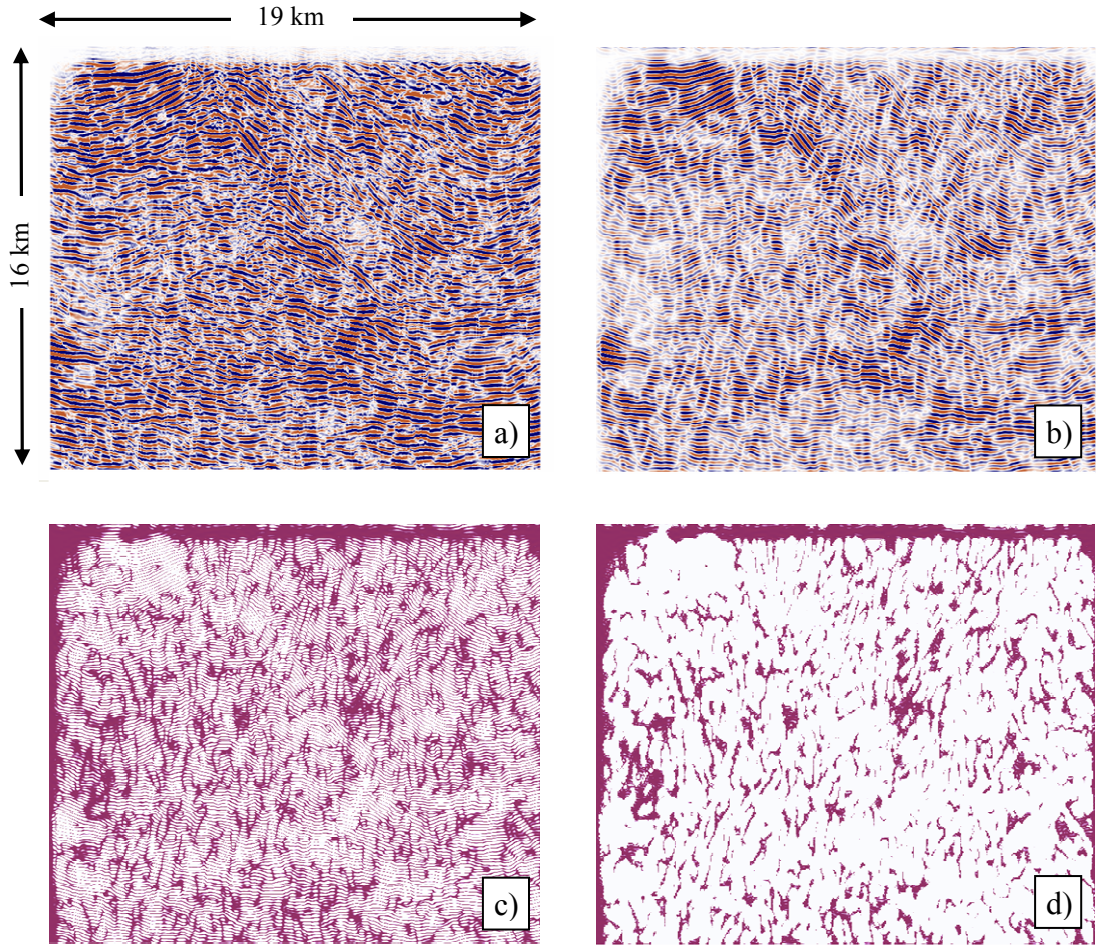

Fig. 5.5: *Middle-scale fractures identification. a) original measured seismic data, b) log-Gabor filtered data, c) inversion of the colour scale of the log-Gabor filtered data, d) resulting fractures after additional image processing steps (such as horizontal lines removal).*

5.3 Faults and Fractures Verification

An important step of the faults and fractures identification process, which must not be neglected, is the verification of results. This important part of the workflow gives estimation about the reliability of the results. Various methods are available to determine whether the detected structures are realistic. Within this work, we chose to examine fractal dimensions of the detected fracture network, comparing sections of the dataset with results of different authors, focal plane solutions of induced microearthquakes and a simple visual analysis.

5.3.1 Visual Evaluation of Results

The simplest way to check the quality of fracture detection is to compare the results visually with the original data. Figure 5.6a shows one sample original cross-section and the corresponding detected fractures in a skeletonised form laid over the seismic section (Fig. 5.6b). Most of the skeletonised fractures have a good counterpart among the structures seen in the original data, which suggests that the fracture detection was successful.

As seen in the Figure 5.6b, outer edges of the skeletonised data cube have also been detected during the filtering process and in the final picture give the false impression of highly fractured areas. Due to the necessity of muting of these boundary effects, the final structural model covers a slightly smaller area than the one originally measured during the 3-D seismic campaign.

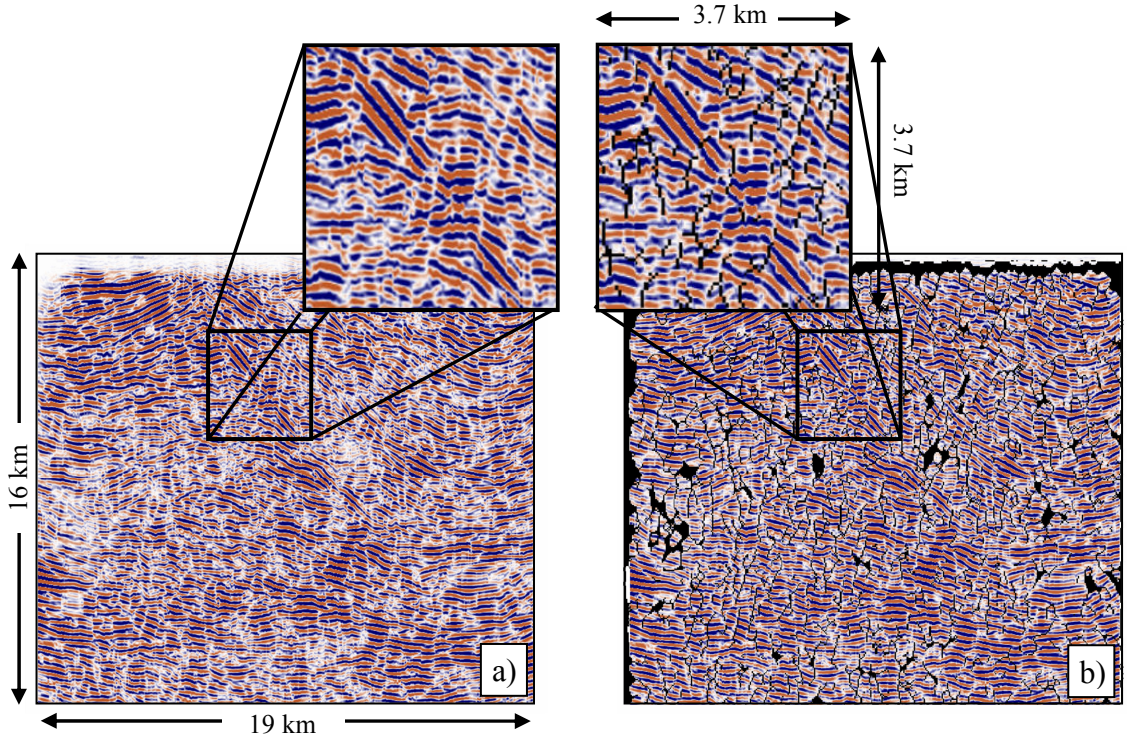

Fig. 5.6: *Sample cross-section showing the original data (a) in comparison with the detected skeletonised middle-scale fractures (b).*

Another possibility for visual comparison offer the KTB85 2-D reflection seismic lines recorded during the DEKORP survey. These seismic lines were part of the KTB pre-site investigation period and represent a valuable source of additional structural information. The latter 3-D seismic measurements were placed into the centre of the broad net of 2-D profiles (Fig. 2.3), making sections of the 2-D lines comparable with inlines and crosslines of similar location from the 3-D dataset. While both datasets were recorded with a 4 ms sampling rate, the DEKORP data have a much higher resolution (100 fold coverage) than the later 3-D seismic data (15 fold). Processing steps of both datasets were performed by the DEKORP Processing Centre (DPC) Clausthal and are comparable as well.

In order to make a simple check of the existence of the alleged middle-scale fractures, a purely visual comparison of corresponding sections from the 2-D and the 3-D seismic dataset has been performed. These requirements are met by the KTB 8502 seismic line, which is crossing the KTB site in the SW-NE direction (Fig. 2.3) and by the corresponding 3-D cross-section, the inline 368. Even though up to now depth migrated cross-sections have been analysed within this work, since the KTB 8502 line is available only as time migrated, also a time migrated version of the Inline 368 has been chosen for comparison. Figure 5.7 shows a sample cut-out of approximately the same coordinates in both profiles.

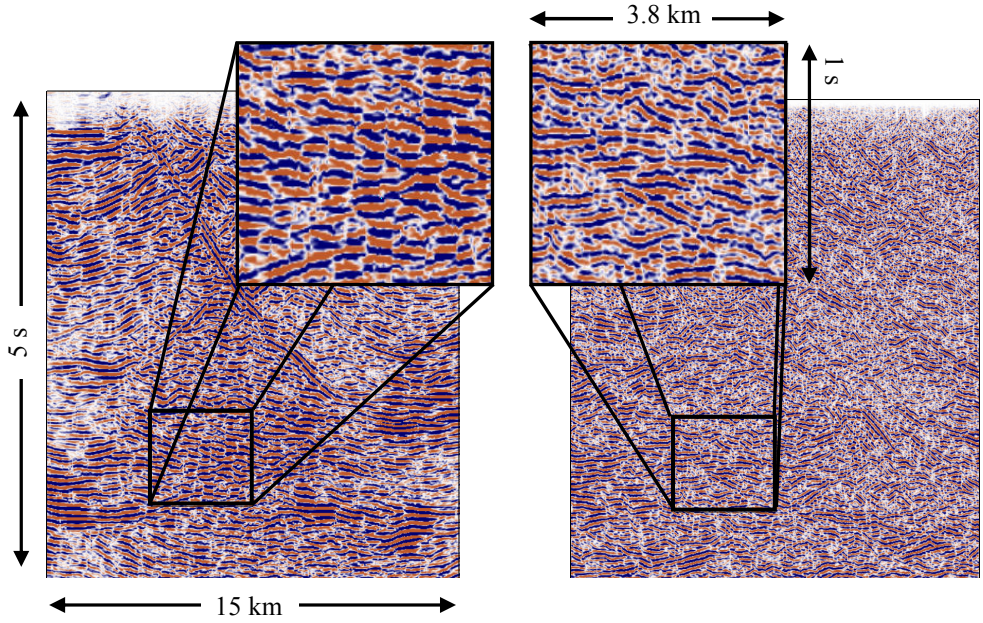

Fig. 5.7: *Visual comparison of 3-D (left) and 2-D (right) cross-sections with the focus on the possible middle-scale cracks.*

While we can state that as well as in the 3-D sections, also in the higher resolution 2-D data can be found structures of similar characteristics (low reflectivity) at roughly the same position, we can hardly talk about a perfect correlation. There can be several reasons for the observed mismatch. The most obvious ones are the not perfectly matching coordinates of the plotted section, the difference in survey geometry of the compared profiles, as well as the different approach during processing of the data. Additionally, it is necessary to stress that a three-dimensional dataset is being compared to a two-dimensional profile. While the 3-D migration of 3-D data provides a correct and detailed image of the subsurface, a 2-D seismic section contains signals from all directions, including those in the surroundings of the profile. During a 2-D migration it is being assumed that the entire recorded signal comes from the structures directly beneath the profile. This is of course not true especially in geologically complex areas (Yilmaz, 2001).

On the other hand, the comparison result could of course be also the indication that the middle-scale fractures are not as continuous and linear as they seem in the 3-D dataset.

5.3.2 Faults and Fractals

Another way to evaluate the plausibility of the detected fractures is the calculation of their fractal dimensions (Mandelbrot, 1983; Turcotte, 1997). While in the classical geometry (the Euclidean space) a point is zero-dimensional, a line one-dimensional, a plain two-dimensional and a volume three-dimensional, fractals with their complicated structure do not fit in any of these strictly defined categories. As the classical examples of fractals: a coastline, Koch snowflake, Sierpinski triangle, Menger sponge, space-filling curve, also faults and fractures fall under the definition of fractals. It is highly problematic to describe the shape of these complex objects quantitatively. Nevertheless, in all fractals it is possible to identify so called self-similar structures, which can be used for the characterisation of the fractal's geometry. Character of fractals can be defined by their fractal dimension. This value can also be used to compare fractals among each other.

5.3.2.1 Fractal Dimensions

While the Euclidian dimensions are always an integer, the fractal dimension can be a rational number. A line and the Sierpinski triangle can be mentioned to explain the fractal dimension calculation. A line is a one-dimensional object, which can be separated into N_i self-similar objects of the same dimension (Fig. 5.8). Each of the pieces is then of the factor $r_i = 1/N_i$ smaller than the original line. The mentioned factor r can be also understood as the linear dimension of the segment. In the case of a two-dimensional square, the factor is $r_i = 1/N_i^{\frac{1}{2}}$ and for a three-dimensional cube, it is $r_i = 1/N_i^{\frac{1}{3}}$. Generalised, it can be said that for a D-dimensional object, the factor will be $r_i = 1/N_i^{\frac{1}{D}}$.

Therefore, dimension of the object can be calculated (Turcotte, 1997)

$$D = \frac{\log(N_{i+1}/N_i)}{\log(r_i/r_{i+1})} \tag{5.5}$$

where $i = 1,2,...n$ and $n \to \infty$.

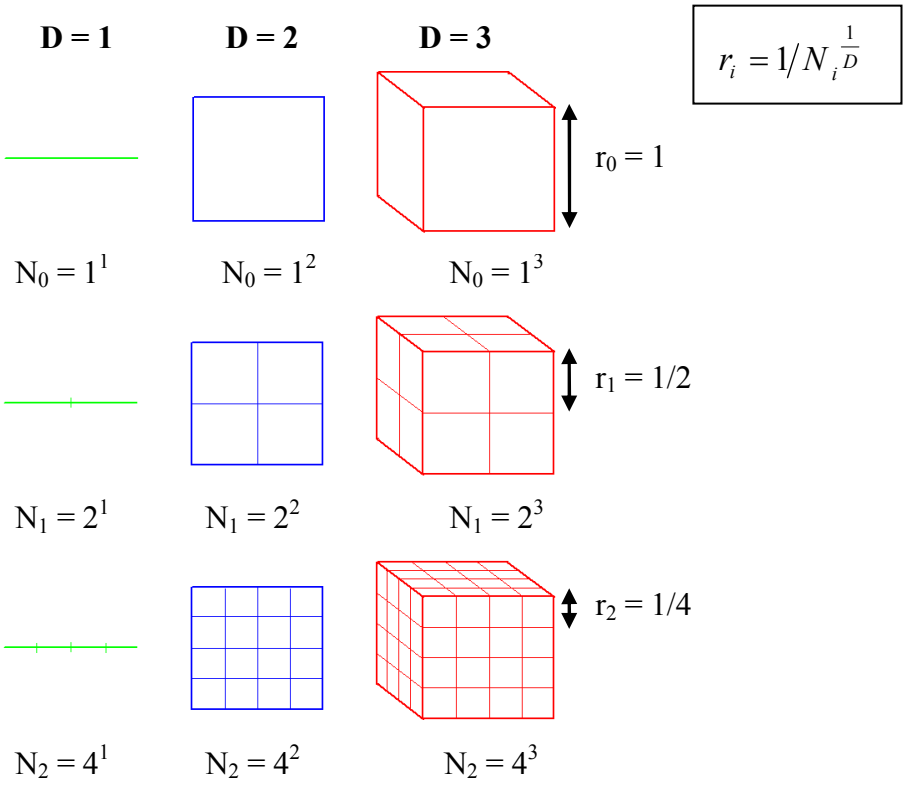

Fig. 5.8: *Explanation of the terms and variables for fractal dimension calculation (figure source http:/www.wikipedia.org/wiki/fractal_ dimension). N is the number of self-similar segments of the size r.*

We now consider a fractal object, for example the Sierpinski triangle and follow the same strategy of the search for self-similar segments (Fig. 5.9). It is possible to separate the Sierpinski triangle into four triangles, which are of the factor $r_1 = 1/2$ smaller than the original. However, the shape of the original triangle is defined by the three outer triangles and therefore $N_1 = 3$. The fractal dimension of the Sierpinski triangle can then be calculated as follows

$$D = \frac{\log(N_{i+1}/N_i)}{\log(r_i/r_{i+1})} = \frac{\log(3)}{\log(2)} = 1.585 \tag{5.6}$$

Fig. 5.9: *Calculation of the fractal dimension of the Sierpinski triangle.*

Other than the above mentioned deterministic examples (Koch snowflake, Sierpinski triangle (Fig. 5.9), Menger sponge), faults and fractures belong to statistical fractals. While the deterministic fractals are exactly scale invariant (fractal), the scale invariance in the case of faults and fractures is only approximate. This means that there will be statistical fluctuations in the measure of their fractal dimensions. (Turcotte, 1997) To calculate the fractal dimension of the KTB fracture network we use the "box-counting" or the Minkowski-Bouligand method (Fig. 5.10). The dataset is divided into equidistant grids of decreasing sizes in several steps. During each step, boxes which are containing a fracture are counted. To get a statistical model, the cumulative number (N_c) of the boxes is then plotted against the linear box dimension (r) on a double logarithmic scale (Fig. 5.11).

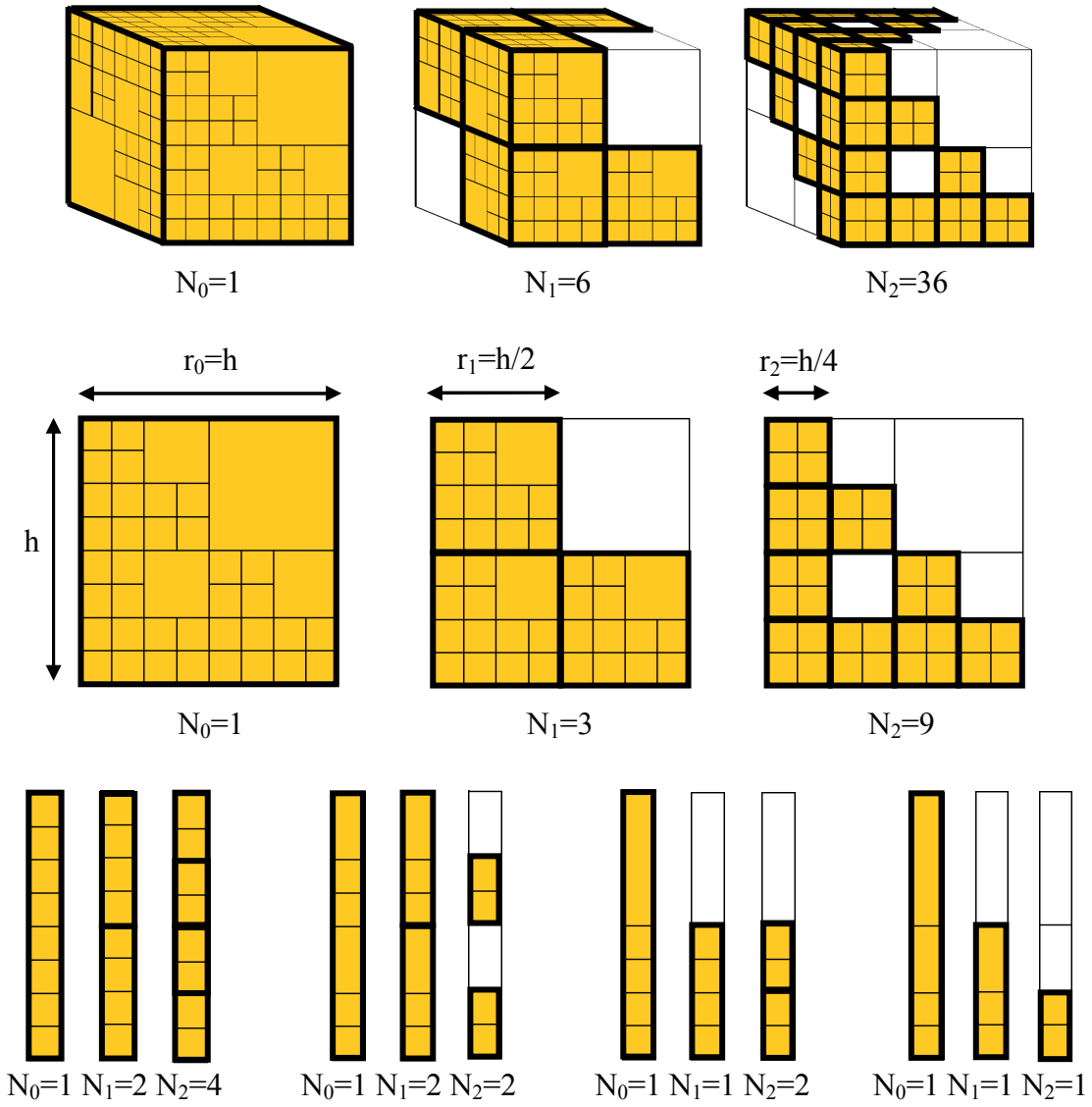

Fig. 5.10: *The principle of the box-counting method. The areas (3-D, 2-D and 1-D) are being stepwise overlaid with boxes of decreasing dimensions (r_i). Boxes of different sizes are marked by yellow colour and bold border line. Thin lines inside the boxes represent faults. The number of boxes which contain a fault is counted (N_i) (after Turcotte, 1997).*

Turcotte (1997) showed that it is possible to relate one-dimensional and two-dimensional distributions to three-dimensional distributions of faults (Fig 5.10 & Fig. 5.11). Figure 5.10 shows a fractal model on which this relation can be demonstrated using the box-counting method.

Fractal dimension calculation of faults in a three-dimensional cube is performed as follows. Using the box-counting method, we overlay the model with grids of decreasing dimensions and count the number of boxes which include a fault. During the first step, there is only one box of the size $r_0=h$ and it is covering the whole volume of the model including the faults, therefore $N_0=1$. We then reduce the dimension of the boxes to $r_1=h/2$ and count the boxes containing faults ($N_1=6$). The box size is reduced again so that $r_2=h/4$ and counting the boxes containing a fault gives the value $N_2=36$. Using the formula (5.5) it is now possible to calculate the fractal dimension of the three-dimensional model

$$D_3 = \frac{\log(6)}{\log(2)} = 2.585\,. \tag{5.7}$$

The two-dimensional cross-section through the model is being treated in the same way. During the first step (zero order), the box of the largest size $r_0=h$ covers all faults and gives the value $N_0=1$. We then reduce the dimension of the boxes to $r_1=h/2$ and count the boxes which cover a fault ($N_1=3$). Again, the dimension of the boxes is reduced to $r_2=h/4$ and the number of boxes of this size containing a fault is $N_2=9$. The fractal dimension of this two-dimensional area can now be calculated using (5.5)

$$D_2 = \frac{\log(3)}{\log(2)} = 1.585\,. \tag{5.8}$$

One-dimensional sections through the fracture model yield four different fault distributions (Fig. 5.10). The box-counting method is applied to each of the distributions. The resulting numbers of boxes containing faults are

$N_0=1,1,1,1$ from which $N_{0average}=1$
$N_1=2,2,1,1$ from which $N_{1average}=1.5$
$N_2=4,2,2,1$ from which $N_{2average}=2.25$.

Using the average values in the formula (5.5) gives the value

$$D_2 = \frac{\log(1.5)}{\log(2)} = 0.585\,. \tag{5.9}$$

The calculations show the following relation between fractal dimensions of one-dimensional, two-dimensional and three-dimensional sections of data containing faults (Turcotte, 1997)

$$D_3 = D_2 + 1 = D_1 + 2\,. \tag{5.10}$$

We can now state that in order to declare a fracture network as realistic, the difference between fractal dimensions of different segments of a dataset shall (as in the case of Euclidean dimensions) be 1.

The range of fractal dimensions can be related to the total volume of fragments and to their surface area (Turcotte, 1997). The general expected values of fractal dimensions are as shown in the case of the fractal model in Figure 5.10 using the equations (5.7) to (5.9). Values of fractal dimensions generally lie between 0 and 1 for a 1-D data segment (data recorded in a borehole), between 1 and 2 for a 2-D data segment (data on a cross-section or a depth-slice) and between 2 and 3 for a 3-D data segment (a three-dimensional sub-volume). However, the values strongly depend on the data and for example, fractal dimension of the value higher than 3 is also possible. As the fractal fills up the line (1-D case), plane (2-D case) or space (3-D case) progressively more, its fractal dimension approaches the higher of the mentioned values.

5.3.2.2 Fractal Dimensions of the KTB Fracture Inventory

Fractal dimensions of the middle-scale fractures detected at the KTB site have been calculated and analysed in order to evaluate the authenticity of the fractures. Within the KTB data cube, we select a number of 3-D subvolumes (of the size 64 x 64 x 64 samples) covering the inner area. Outer border areas of the data cube are affected by boundary effects and were not taken into consideration during the fractal dimension calculation. The box-counting method (Fig. 5.10) is then applied to the subvolumes with of the box sizes $r = h, \frac{h}{2}, \frac{h}{4}, \frac{h}{8}, \frac{h}{16}, \frac{h}{32}, \frac{h}{64}$. Formula (5.5) is then used to calculate the fractal dimensions.

We then also analyse 2-D cross-sections and 1-D line segments through the selected subvolumes. The box-counting method with the above mentioned box sizes applied on the segments yields values for the calculation of fractal dimensions. The cumulative number (N_c) of boxes is plotted against the linear box dimension (r) on a double logarithmic scale for a statistical model. The obtained average fractal dimensions for the middle-scale fracture inventory of the KTB site and their standard deviations (±) are (Fig. 5.11)

$$\begin{aligned} &\text{1-D:} \quad D_1 = 0.76 \pm 0.08 \\ &\text{2-D:} \quad D_2 = 1.87 \pm 0.20 \\ &\text{3-D:} \quad D_3 = 2.81 \pm 0.11. \end{aligned} \tag{5.11}$$

As already mentioned in Chapter 5.2, the automated search allowed us to identify not only linear structures possibly representing middle-scale fractures, but also areas and bodies of characteristics similar to those of the fractures. This fact explains the high occurrence of “spots” in the fracture network dataset and consequently also their effect on the fractal dimension calculation. The presence of such a body (treated here same as the linear structures) in the data leads to a higher number of cells containing a fault of and is therefore increasing the fractal dimension of a fault zone unnaturally. For this reason, the largest cells were omitted during the calculation of fractal dimensions.

Since the relation (5.10) between the fractal dimensions of one-dimensional, two-dimensional and three-dimensional sections of the KTB dataset is fulfilled,

$$D_3 \approx D_2 + 1 \approx D_1 + 2 \qquad (5.12)$$

$$2.81 \approx 1.87 + 1 \approx 0.76 + 2$$

we can claim that the fracture network identified at the KTB site can be considered as realistic.

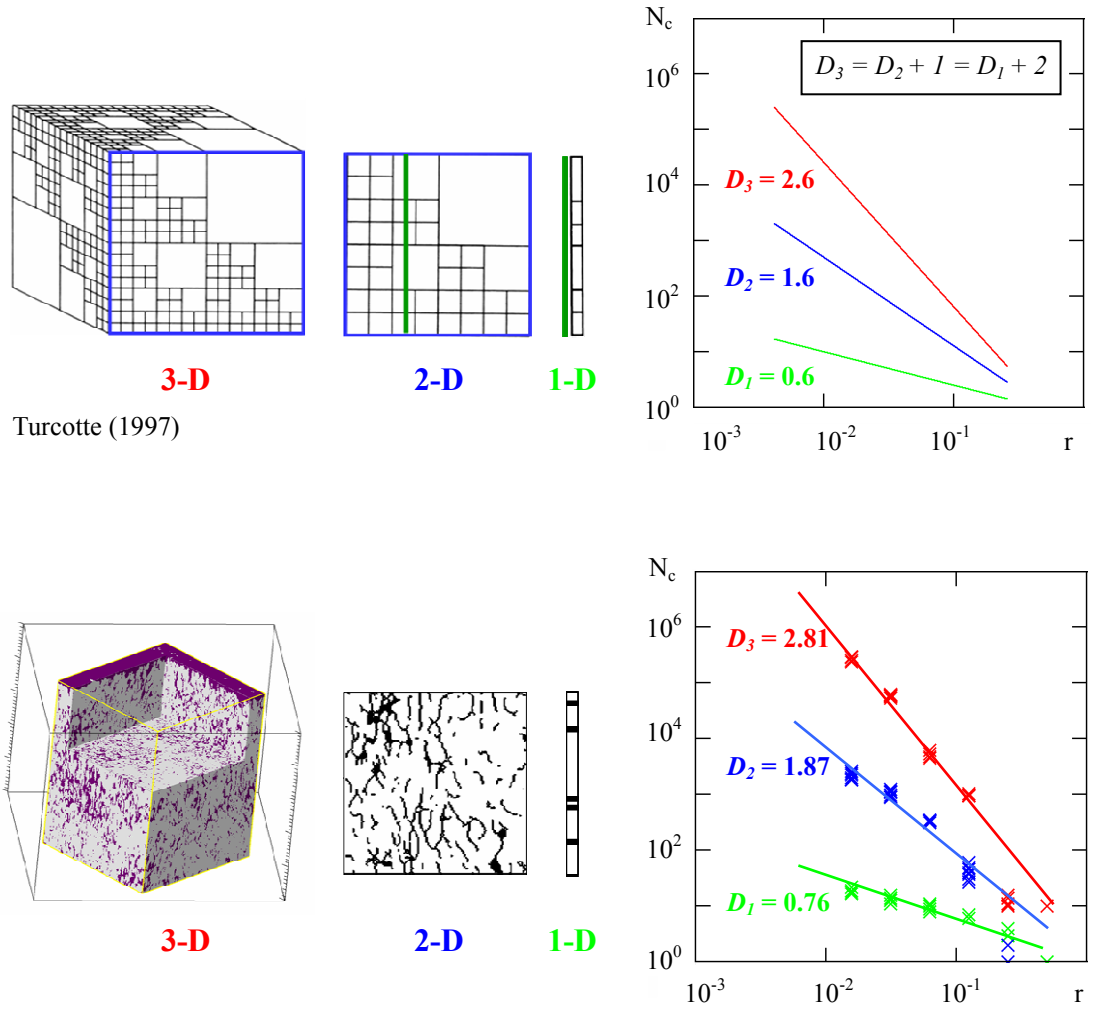

Fig. 5.11: *Theory of fractal dimension calculation according to Turcotte (1997) and its application to the middle-scale fractures detected in the KTB dataset. Average fractal dimension of 3-D subvolumes is D_3=2.81, of 2-D cross-sections D_2=1.87 and of 1-D segments D_1=0.76. Nc is the cumulative number of boxes of the linear dimension r.*

The KTB super-deep borehole offers a number of miscellaneous information concerning the penetrated rock. Interestingly, the evaluation of some other features and properties showed that they also fulfil the requirements of fractal distribution. Calculation of fractal dimension of 1-D profiles extracted from the KTB lithology, P-wave velocity minima, as well as fracture density maxima, reveals the value $D_1 = 0.6$ (Fig. 5.12). This value is also very close to the average fractal dimension calculated for one-dimensional segments of the KTB fracture dataset (5.11). This demonstrates the importance of fractals and shows that they indicate the interdependence of diverse features in nature.

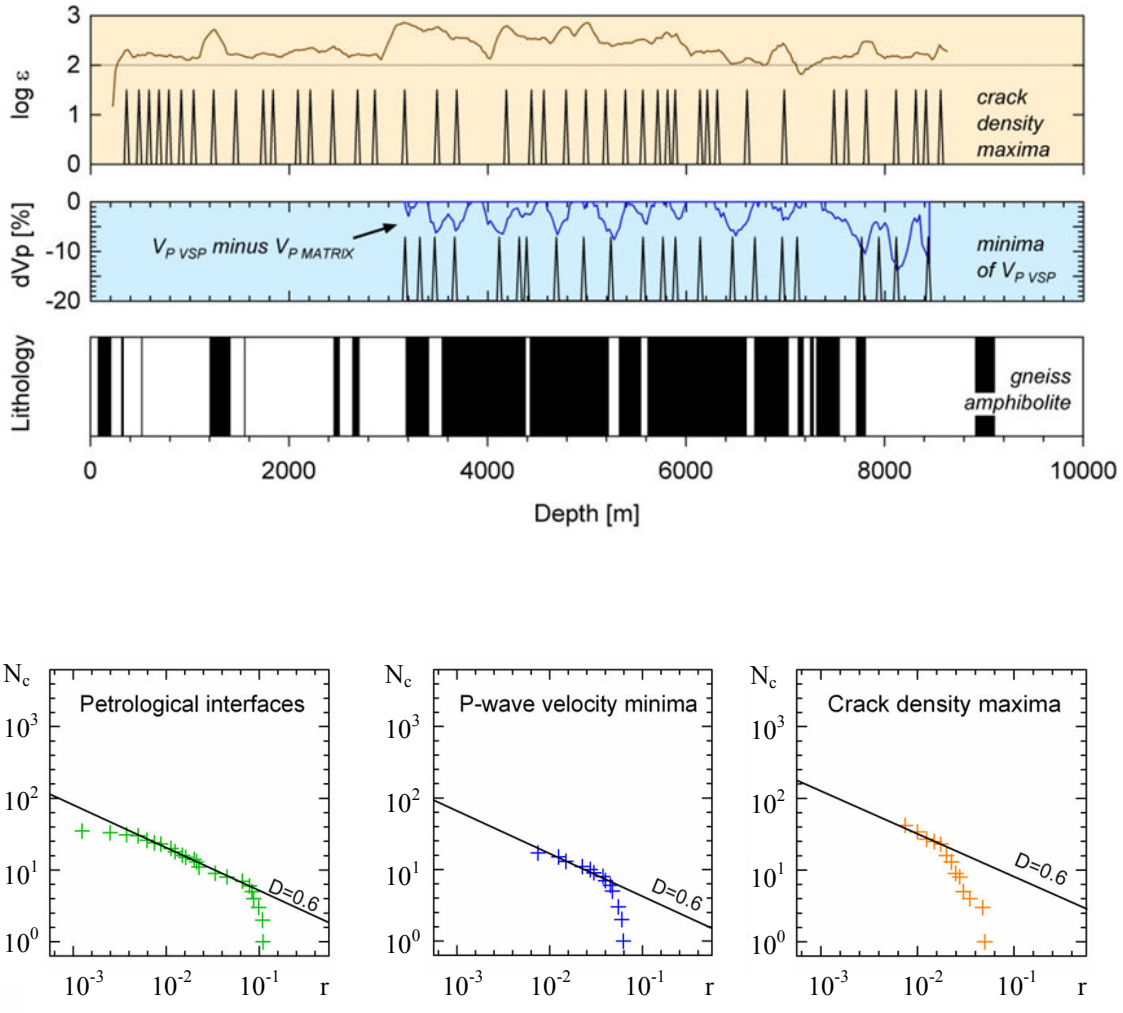

Fig. 5.12: *Fractal dimensions of 1-D lithological, P-wave velocity minima and fracture density maxima profiles. (W. Rabbel personal communication).*

5.3.3 Fault Mechanisms of Induced Seismicity at the KTB

Plausibility of middle-scale fractures identified by log-Gabor filtering can be evaluated also through the analysis of focal mechanisms calculated for microearthquakes induced during fluid injection experiments. This approach is based on the assumption that tectonic stress is released on pre-existing fractures when fluid pressure is being increased (Healy et al., 1968). Therefore we examine the link between middle-scale fractures detected at the KTB site and the induced microearthquakes.

The connection between "man-made" earthquakes and fluids has been first realised in the 1940s, during a lake impoundment. Explanations of mechanisms triggering fluid induced seismicity are several. The one most applicable to the crystalline environment of the KTB site was presented by Healy el al. (1968), who explained increased seismicity during injection of fluids into crystalline rock near Denver, Colorado. Healy el al. (1968) proposed that the increasing fluid pressure along pre-existing fractures reduced the effective normal stress on the fractures and initiated a release of tectonic stress.

The Continental Deep Drillhole project incorporated two fluid injection experiments. In 1994 a short-term injection experiment has been conducted immediately after drilling was terminated. The second, long-term experiment followed in the year 2000. An overview of the long-term injection experiment carried out in the KTB borehole gives Baisch et al. (2002). Seismic activity was monitored by a temporary seismic network consisting of a borehole sonde in the pilot hole (at depth 3827 m) and a surface network with 39 seismologic stations. Over the period of 3 months a total of 2799 microearthquakes were detected by the borehole sonde. The average location accuracy for these events is ±147 m, ±127 m and ±26 m for eastern, northern and vertical direction respectively (Baisch et al., 2002).

Bohnhoff et al. (2004) analysed a set of 192 microearthquakes induced during the long-term injection experiment, located between 5000 m – 6000 m depth and determined accurate fault plane solutions for 125 events. Magnitudes of these events range from -1.2 to +1.1. Figure 5.13 shows fault plane solutions which are representative for the entire dataset. Orientation of tension (T) and pressure (P) axes, as well as dilatation and compression are plotted in the figure. The weakest of these four events (Fig. 5.13a) is of the magnitude -0.6 and its fault plane solution is the least constrained. The strongest event (magnitude 0.9) is in Figure 5.13d.

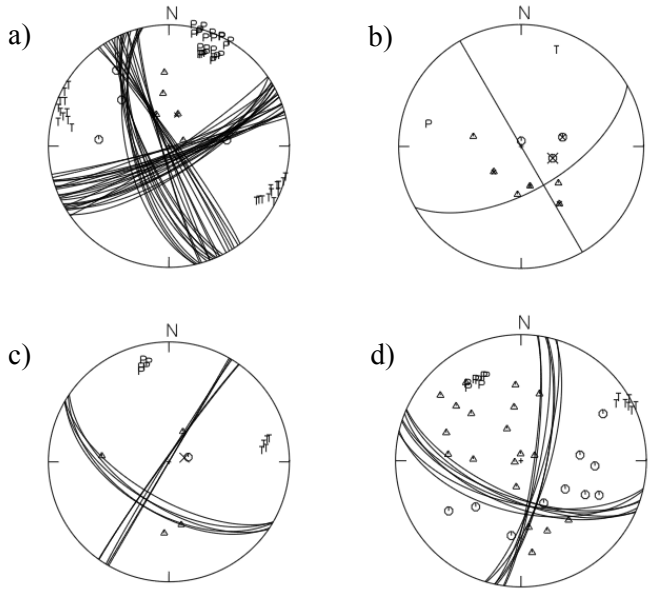

Fig. 5.13: *Fault plane solutions chosen as representative for the microearthquakes induced during the long-term experiment in the year 2000. P and T stands for the pressure and tension axes respectively,* ▵ *represent dilatation and* ○ *compression Bohnhoff et al. (2004).*

We attempt to compare the fault plane solutions determined by Bohnhoff et al. (2004) with the general direction of the middle-scale fractures detected by log-Gabor filtering. Since the direction of fractures can vary with depth, we select the depth-slices which coincide with the location of the microearthquakes. In their work, Bohnhoff et al. (2004) searched for planar structures within the examined seismic cloud through hypocenter distribution analysis. This approach was based on the assumption that the most effective coupling of injection pressure occurs along planar fracture planes (e.g., Fehler et al., 1987; Phillips et al., 2002). By taking into account also the source mechanisms, Bohnhoff et al. (2004) selected 66 events and grouped them into four planar structures as presented in Figure 5.14 & Figure 5.15.

Figure 5.14 shows map views of the focal mechanisms together with corresponding depth-slices from the middle-scale fracture dataset. The KTB fracture dataset does not show an image equally detailed as is the case of the induced microearthquakes, therefore scales of the compared images do not match. The depth-slices show a much larger area. Nevertheless, if we transfer the nodal planes of each of the available fault plane solutions onto the depth-slices, we can make the following conclusions. Even though the image of small-scale fractures is complex, one can say that the majority of fractures is lined up in the NW-SE direction. This direction corresponds very well with one of the nodal planes (red) of the fault plane solutions which thus possibly represent the fault planes. The other nodal plane, in Figure 5.14 depict in green, would then be the auxiliary plane.

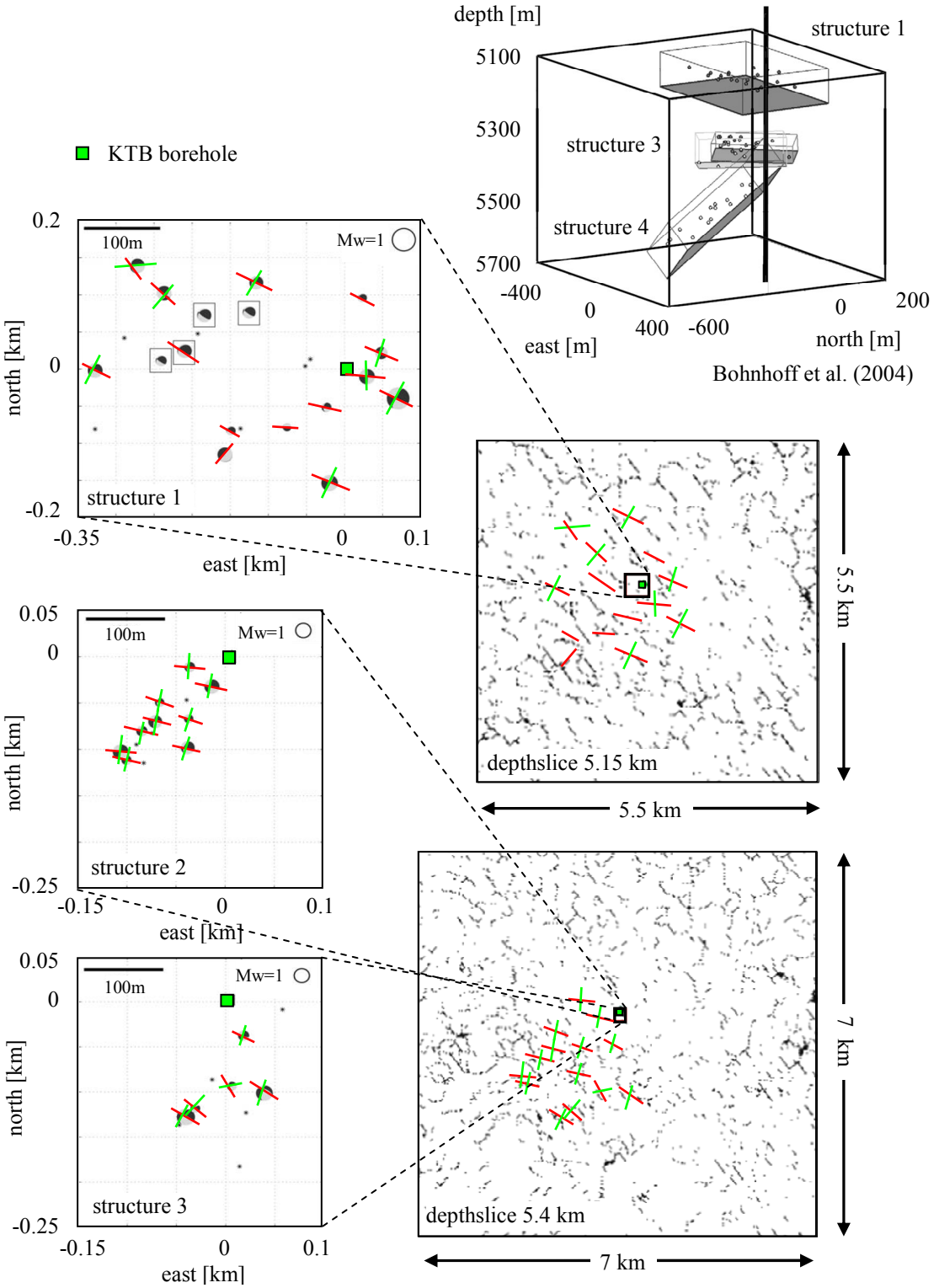

Fig. 5.14: *Comparison of fault plane solutions of induced microearthquakes by Bohnhoff et al. (2004) with the direction of small-scale fractures detected by log-Gabor filtering. Size of the beachballs is scaled to the magnitude M_w. Fault plane solutions marked by a rectangle in structure 1 are compound solutions for repeating earthquakes.*

Another way to compare the induced microearthquakes with the detected fractures takes advantage of the planar structures defined by Bohnhoff et al. (2004). A volume of the same size and the exactly the same position has been extracted from the dataset containing middle-scale fractures. Figure 5.15 shows a 3-D section of the KTB dataset of the size 800 m x 800 m x 6000 m with the four planar structures (left) defined through hypocenter distribution analysis and a 3-D section with fractures detected by the log-Gabor filtering (right). In order to plot the fractures in 3-D, it was necessary to calculate an isoplane which covers the fractures and creates a kind of planar structures.

While examining these images, it is important to remember that there might be fractures on which microeathquakes were not triggered during the injection experiment. These fractures would then not be included in the data. It is also necessary to keep in mind the microearthquake location uncertainties. Nevertheless, even though it was not possible to break the middle-scale fractures into four separate structures, similarities to Bohnhoff et al. (2004) results are obvious. It seems that both approaches uncover hints of a subhorizontal structure in the upper part of the section (5100 m – 5200 m) and a structure dipping towards SW located in the lower part. Equivalents of structure 2 and 3 can also be identified in the middle-scale fracture dataset, but they seem to form one fault plane rather than two isolated ones.

The fractures, as they were depict by log-Gabor filtering could then be responsible for microearthquakes induced during the fluid injection experiment. Results of this comparison speak again for the authenticity of the middle-scale fracture network.

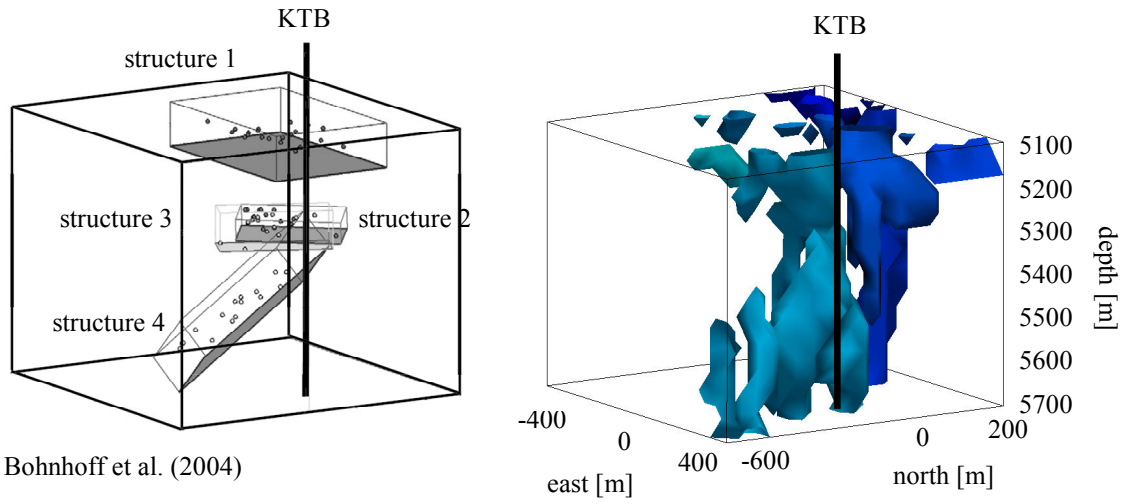

Fig. 5.15: *Selected hypocenters in the depth interval 5100 m – 5700 m grouped into four planar structures by Bohnhoff et al. 2004 (left). Middle-scale fractures as identified by log-Gabor filtering in the same depth section (right).*

5.4 Fracture Connectivity

Resolving the fault and fracture network of a site is only the first step towards understanding of the fluid-flow paths. In order to have an effect on the temperature and flow field, fluids existing in the underground rock need to be percolating through an interconnected net of fractures. Isolated fractures and fracture clusters with no connection to the neighbouring clusters do not contribute to the total flow field. Connectivity of fractures is thus a key factor in fluid flow prediction and modelling.

Fracture connectivity of the network within the examined data volume was analysed by means of the percolation theory (e.g. Flory, 1941; Stockmayer, 1943; Stauffer & Aharony, 1994; Turcotte, 1997). The percolation theory describes complex, mostly unsorted structures composed of simple elements and explains the origin of macroscopic structures which are creating connections between the distant elements or areas.

Every dataset can be understood as a set of points or cells. During percolation modelling, we concentrate on the connections between the neighbouring cells. If we determine the fracture connectivity of a system, we can talk about "open" or "closed" cells. A cell can be called open if, for a hypothetical particle, it is possible to pass through it and enter a neighbouring cell. Considering the processed fracture network dataset, a cell is "open" or "closed" for fluid flow depending on whether it is crossed by a fracture.

We calculate the probability of the existence of a path through which fluids can travel infinitely far. Probability (p) can reach values between 0 and 1, where $p = 0$ means that every cell is closed and thus no fluid movement can occur and $p = 1$ that every cell is open and so there must be an infinite open path (Fig. 5.16). The critical probability (p_c) sets a threshold above which percolation occurs (Austin, 2009).

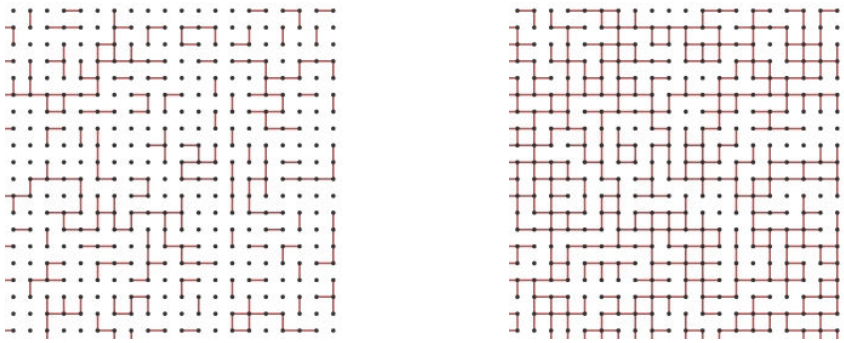

p = 0.3 p = 0.7

Fig. 5.16: *An example of a hypothetical media with a different number of open cells. Probability that there is an infinite path through which fluids can travel is 0.3 (left). Probability of an infinite path is 0.7 (right) (Austin, 2009).*

In the case of crystalline rock which is characterised by rather low porosities and permeabilities, the question whether a cell is open is closely related to the presence of fractures. According to Turcotte (1997), if the fractures are filling out a cell to at least 30%, it is an indication that the cell is open. We therefore perform calculations of fracture densities which can then be directly related the fracture connectivity.

In the case of the KTB dataset, both, the middle-scale fractures and the large-scale faults were taken into account for the calculation of fracture connectivity. Cells of different sizes were chosen in order to observe the behaviour and extent of areas with the relevant fracture densities. Figure 5.17 (left) shows a cross-section with the fracture network in black and the calculated probabilities of fluid flow in colour code. Probability values below 0.3 are plotted in white and mark areas of very low or even not existent flow. In agreement with results of fracture connectivity calculations, the dataset was divided into units of relative fracture permeabilities (Fig. 5.17 right).

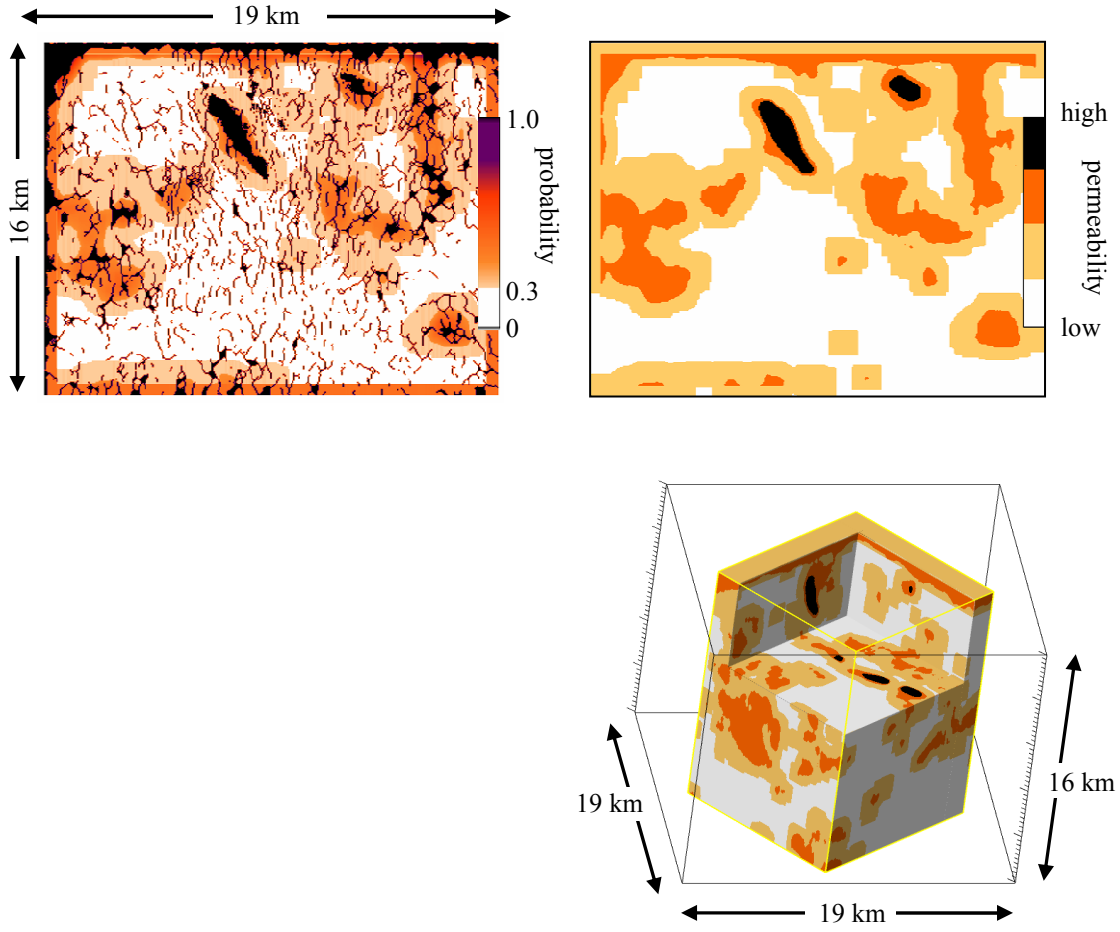

Fig. 5.17: *Left: A cross-section with the fracture network in black and the calculated probabilities of fluid flow in colour. Right: Dataset separated into units of relative permeabilities.*

5.5 Fracture Orientation

Throughout the complicated tectonic history of the Oberpfalz, faults and fractures of various directions originated in the crystalline rocks of this area. Results of the before mentioned fracture connectivity calculations are valid only for the assumption that all the identified cracks and fractures with their different orientations provide pathways open for fluid flow. Since seismic data alone do not distinguish between an open and a closed (healed) fracture, the fracture network identified with the previously described methods may contain both. In order to evaluate fracture connectivity and the consequent fracture permeability correctly, it is necessary to consider only fractures open for fluid flow.

It has been shown before that permeability of critically stressed fractures is much higher than of those not critically stressed in the current stress field (Barton et al., 1995; Hickman et al., 1997). Similar, as Ito & Zoback (2000), who examined the relationship among fracture connectivity, fracture orientation and the state of in situ stress, we also attempt to analyse the fracture network of the KTB site in the same way. While Ito & Zoback (2000) worked with a dataset of small-scale fractures detected by the formation micro scanner (FMS) in a limited depth interval (3000 m – 7000 m), we are analysing the whole volume of KTB data. It is important to remember that the fracture network identified on the basis of the processed 3-D seismic measurements is of a different scale than the FMS detected fractures and thus the results can not be put into comparison. Sampling interval of the ISO89 3-D seismic measuring campaign was 50 m, which means that disturbances finer than this interval could not be detected.

To decide whether a fracture is critically stressed in the current stress field, it is necessary to determine the shear (τ) and normal stress (σ_n) acting on it and compare it with the Coulomb criterion for frictional sliding of fractures

$$\tau = \mu(\sigma_n - P_p), \tag{5.13}$$

where μ is the coefficient of friction along a fracture plane and P_p is the local pore pressure.

Fracture planes, which have a ratio of shear to normal stress higher than 0.6 are optimally oriented in the stress field and thus are most probably permeable (Byerlee, 1978).

Normal stress and shear stress can be calculated with (Ito & Zoback, 2000)

$$\sigma_n = E^2\sigma_1 + F^2\sigma_2 + G^2\sigma_3 \tag{5.14}$$

$$\tau = \left[E^2F^2(\sigma_1 - \sigma_2)^2 + F^2G^2(\sigma_2 - \sigma_3)^2 + G^2E^2(\sigma_3 - \sigma_1)^2\right]^{\frac{1}{2}}. \tag{5.15}$$

E,F,G are the direction cosines between the normal of the fracture plane and axes of σ_1, σ_2 and σ_3 (the three principal stresses) respectively.

In order to determine the orientation of each fracture within the 3-D dataset and so the needed direction cosines (*E,F,G*), normals to fracture planes had to be calculated within a moving window of an thoroughly chosen size centred around the fracture. A crude description of the shape and orientation of the fracture offers the covariance matrix,

which can be also viewed as an ellipse. Diagonalising of the covariance matrix causes the change of the original coordinate system *x'y'* to the *xy* coordinate system. Essentially, the ellipse is being rotated around the coordinate system origin as showed in Figure 5.18 so that ellipse axes are aligned with the new coordinate system. Diagonal elements of this new, diagonalised covariance matrix are the eigenvalues and the eigenvector of the largest eigenvalue represents the normal direction of the fracture plane (Luo et al., 2006).

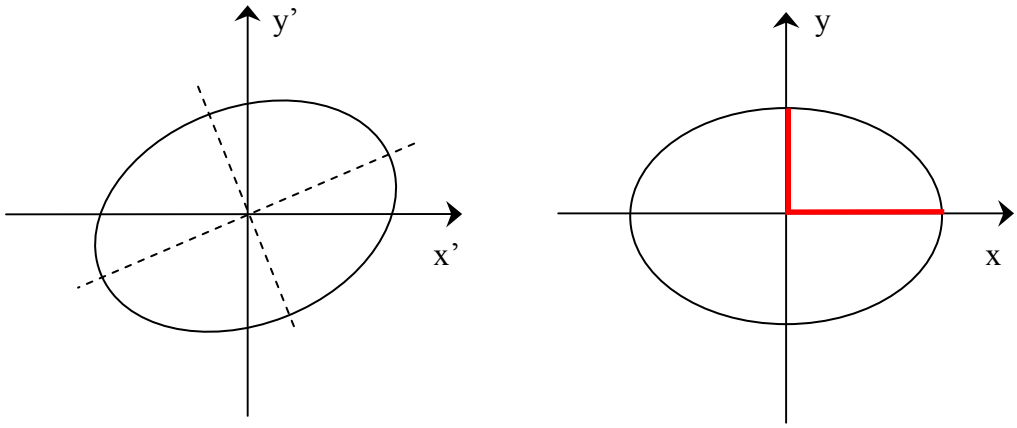

Fig. 5.18: *Ellipses representing a covariance matrix (left) and the diagonalised covariance matrix (right). Axes of the diagonalised ellipse (marked in red) represent the eigenvectors.*

In the case of a three-dimensional system, the axes rotated are those of an ellipsoid. These axes, which form the new coordinate system, are the three eigenvectors. As described above, we calculate the normal to the fracture plane with the help of the covariance matrix (C) of a three-dimensional system

$$C = \begin{bmatrix} \mathrm{cov}(x,x) & \mathrm{cov}(x,y) & \mathrm{cov}(x,z) \\ \mathrm{cov}(y,z) & \mathrm{cov}(y,y) & \mathrm{cov}(y,z) \\ \mathrm{cov}(z,x) & \mathrm{cov}(z,y) & \mathrm{cov}(z,z) \end{bmatrix}, \tag{5.16}$$

where

$$\mathrm{cov}(x,y) = \frac{1}{N}\sum_{i=1}^{N}(x_i - \bar{x})(y_i - \bar{y})\,. \tag{5.17}$$

N cell size

$\bar{x}, \bar{y}$ variable means

The current stress field has been estimated in the KTB borehole by Brudy et al. (1997) and was further simplified by Ito & Zoback (2000) by assuming linear stress profiles of the depth range (d in metres) 3000 m to 7000 m as follows

$$\sigma_H = 0.045d, \quad \sigma_h = 0.02d, \quad \sigma_v = 0.028d, \tag{5.18}$$

where σ_H and σ_h are the principal stresses (in MPa) in a horizontal plane ($\sigma_H > \sigma_h$) and σ_v is the vertical principal stress.

Direction cosines E,F,G between the normal of the fracture plane and axes of the three principal stresses respectively can then be calculated and used for determining of the normal and shear stress.

It is also necessary to consider the pore pressure, in other words the pressure acting on fluids filling out pores of the rock. Since pore pressure is effective in all possible directions, all normal stresses acting on the rock matrix are reduced by its value to create the effective normal stress ($\sigma_n - P_p$). Huenges et al. (1997) report both direct and indirect estimates of pore pressure P_p in the KTB drillhole that indicate an essentially hydrostatic gradient to 9.1 km depth with a mean formation pore pressure gradient of 11.5 MPa.km^{-1} and the value 103 ± 3 MPa at 9101 m depth.

Calculated shear and effective normal stresses acting on the fractures at the KTB site have been plotted into 3-D Mohr diagrams. A sample Mohr diagram in Figure 5.19 shows shear and normal stresses of fractures identified in a 15 km x 15 km sub-section of the KTB data in 3 to 7 km depth. Because of the variation of stress magnitudes over the depth range, the Mohr diagrams have been normalized by the vertical stress σ_v. The values do not show any signs of clustering; they are distributed evenly over the whole area of the diagram. Stresses lying close to and above the Coulomb failure line (> 0.6) belong to fractures which are critically stressed in the current stress field and are thus possibly permeable.

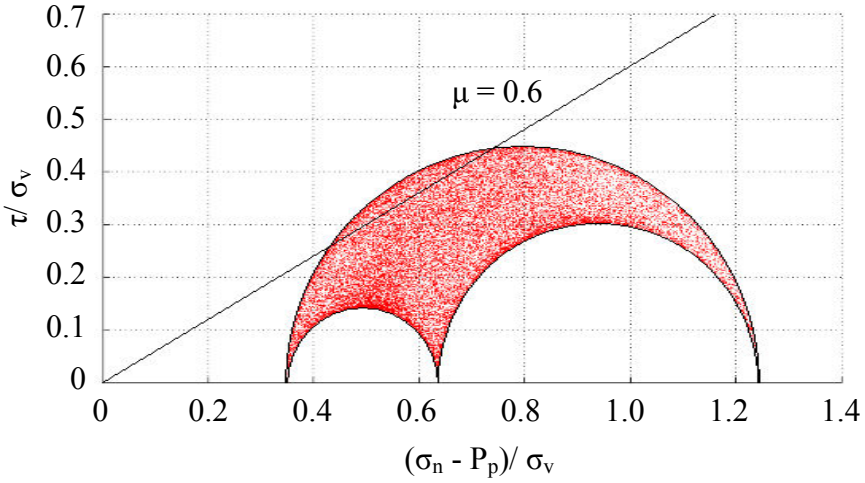

Fig. 5.19: *3-D Mohr diagram of shear and effective normal stresses acting on fractures in a KTB sub-volume.*

Fracture network of the whole KTB site has been further analysed by means of elimination of the fractures laying below the Coulomb failure line, in other words, the impermeable fractures. As can be seen in Figure 5.20, the above described stress-field analysis led to a considerable reduction of the small-scale fracture inventory. Not only that a large number of fractures was divided into segments of shorter extent, which lead to the loss of their continuity, many fractures were eliminated completely. Fracture connectivity based on the percolation theory as described in the Chapter 5.4 has been applied also to this, "corrected" fracture network in order to receive new units of relative permeabilities. However, due to the now very small amount of continuous and connected fracture, the dataset does not show any noteworthy fracture connectivity. This means that in the site of the KTB, no remarkable groundwater flow should be observed. This finding is supported by the coupled hydraulic and thermal simulations of the area, which are presented in the Chapter 6.2.1.

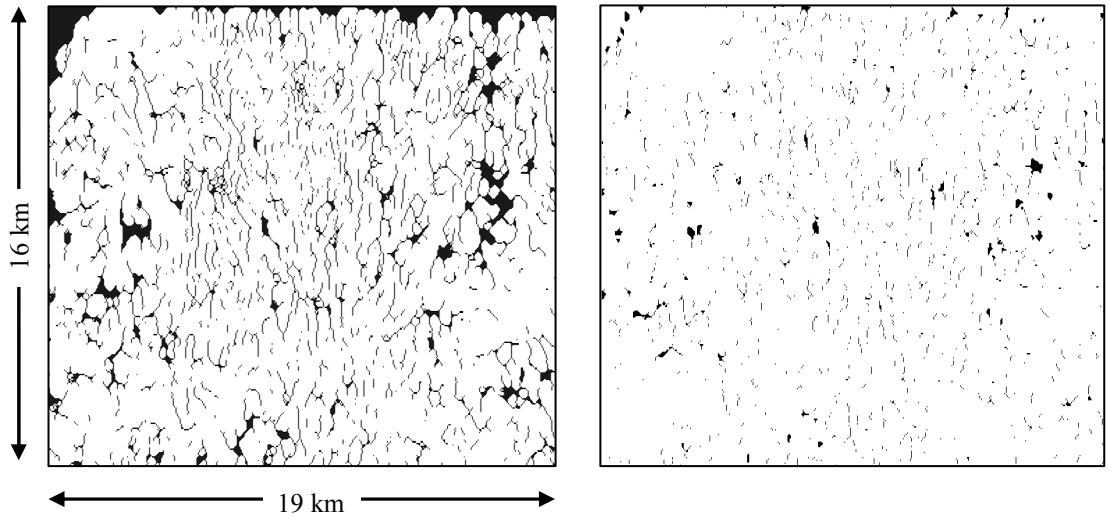

Fig. 5.20: *Small-scale fractures plotted on a vertical cross-section through the dataset. Left: All fractures detected by the Log-Gabor filtering method. Right: Fractures, which were defined by the stress-field analysis as favorably oriented. These fractures are assumed to be hydraulically open.*

5.6 Summary

A fracture network belongs to the main and most important segments of a structural model. Especially if hydrothermal modelling of a reservoir located in crystalline rock is aspired, fractures, faults and cracks are of special importance. If low porosity and low permeability values characterise the rock matrix, fluids travel preferably through the pathways represented by hydraulically open fractures.

At the KTB site, fault families of different scales have been detected. We distinguish three groups which in the further processing are being treated differently according to the expected influence of the particular fracture group on the flow field. The vast amount of fractures crossing the rock matrix required an automated identification approach. A binary representation of the fracture network which simply differentiates between the matrix rock and fracture has been chosen.

The Franconian Lineament, in the seismic datasets named seismic event (SE), falls under the group of large-scale faults. As one of the most distinct features of the KTB site, it separates foreland sediments in the SW from the crystalline rock. Being a bundle of faults rather than a single shift of horizons, the available seismic cross-sections provide a very good image of this deep reaching zone. Steep inclination as the main characteristic feature has been used in the recognition process of large-scale faults. *K-k* filtering provided good results especially when combined with three-dimensional dip calculations. With the help of a restriction interval of dip values, the data were converted into binary coding, clearly identifying fault-affected areas.

Apart to the presence of SE faults, another structures characterised by horizon shifts accompanied by low reflectivity have been detected in the seismic cross-sections. We attempt to confirm the assumption that these elements represent middle-scale fractures. After isolating them from the surrounding matrix with the help of log-Gabor filtering and image processing, we apply several approaches to analyse their authenticity. Fracture dimension calculations, visual comparisons with the higher resolved KTB8502 profile and comparisons with the interpretation of injection experiments were performed to evaluate the alleged middle-scale fractures. Results of all these methods speak for their plausibility.

In order to enhance rock permeability, the mere presence of a fracture is not sufficient. Only fractures interconnected in a way that allows hydraulic communication can result in pathways affecting the thermo-hydraulic flow field. With increasing density of fractures, also the probability of fracture connectivity increases. The percolation theory states that if a medium consists at least to 30 % of fractures, fluids start to percolate. Following this theory, we define zones of different fracture densities and relate them to relative fracture permeabilities.

Information about the presence of faults and fractures has been saved onto the same grid which has been already produced during the identification of lithological units. This means that the resulting list of grid points will incorporate information about both, lithological unit and presence of a fault.

Chapter 6

Coupled Thermo-Hydraulic Processes

In order to get a better understanding of hydrothermal processes taking place in the underground and to assess the reservoir‘s geothermal potential, we perform heat and fluid flow simulations. The structural model of a site containing the necessary information about the fracture network, lithological units and petrophysical rock properties serves as input for the simulations. The following hydraulic and thermal properties were required for the modelling:

porosity
permeability
thermal conductivity
heat production.

Porosity, as one of the primary factors controlling movement of fluids within rocks, defines spaces between grains of the matrix. An accurate porosity value of the different rock units can be determined by logging, or directly on core samples in a laboratory. At the site of the Continental Deep Drillhole, the only lithological unit with a higher porosity is the unit of Permo-Mesozoic sediments in the SW; the other rock units show only low porosity values. Porosity is closely related to permeability as pores hydraulically connected to the surroundings contribute to the general fluid flow.

Permeability, as the central factor describing hydraulic properties of rocks can be divided into matrix permeability and fracture permeability. Contribution of the matrix in porous rock (such as sedimentary locations) is considerable and is, at the absence of open cracks, the dominant factor for fluid transport. In the case of a crystalline underground, contribution of matrix permeability to fluid transport is only minor and hydraulic properties of the site are defined mainly by preferred fluid paths represented by cracks and fractures. Quantitatively this means low rock matrix permeability compared to fracture permeability. The main factors affecting fracture permeability are density and orientation of fractures, but also the extension and hydraulic conductivity of the different fracture planes (Barton et al., 1995). In the case of the KTB gneisses which are characterised by distinct foliation, also permeability anisotropy has been observed (Huenges et al., 1997).

Thermal conductivity, another required petrophysical rock property, describes the ability to conduct heat and varies with rock composition. It is usually measured in a laboratory on cores, cuttings or rock flour. While metabasites penetrated by the KTB borehole show predominantly isotropic thermal conductivities, gneisses are highly anisotropic (Huenges et al., 1990; Pribinow et al., 1993). Anisotropy is related to the foliation and lineation of the rock, where in the direction parallel to foliation, same as in the case of permeability, thermal conductivity values are higher.

Heat production, just as thermal conductivity, is influenced by rock composition. It reflects geochemical conditions prevailing during rock formation and is temperature and pressure independent (Rybach, 1976). The heat produced by naturally radioactive elements in rocks is a very important factor in geothermal studies. Generally, heat production rate decreases with increasing depth and this variation is often described by a simple exponential or linear approximation (Lachenbruch, 1970). As already mentioned in the Chapter 2.3, distribution of heat production at the KTB site does not follow this law, although a slight decrease with increasing depth could be detected (Emmermann & Lauterjung, 1997).

Aim of geothermal simulations is to evaluate the reservoir's potential with respect to geothermal energy or heat production. The above mentioned rock parameters known or estimated are inputted into a geothermal simulation software to calculate the temperature distribution, fluid and heat flow. The modelling strategy involves the calculation of hydrothermal processes in an area which is considerably larger than the area of interest. This is done to predict the interacting processes in the underground and to evaluate the importance of various input factors. The resulting temperature distribution and the local heat-flow serve then as boundary conditions for models of a smaller scale. The question of geothermal energy production is being addressed on these more detailed models of smaller areas, where various production schemes can be simulated. The main focus is laid on the amount of extracted heat and the possible lifetime of the different designs (Ondrak et al., 1998).

6.1 Simulation Algorithm and Governing Equations

Geothermal reservoir simulation is a complex task due to the number of processes involved, such as geometry, hydraulics, thermal effects and possible geochemical reactions. The simulation tool used within this work was the new simulation package SHEMAT-Suite (Rath et al., 2006), a further developed version of the modelling code SHEMAT (Simulator for Heat and Mass Transport) (Clauser (ed.), 2003). This software is capable of performing coupled thermal and hydrogeological simulations involving fluid flow, heat transfer, species transport and chemical reactions between reservoir rock and the fluid in porous media. SHEMAT-Suite incorporates both, a two-dimensional and three-dimensional finite difference simulation solver and is able to solve forward, as well as inverse computations. However, this work is limited to forward calculations of three-dimensional models.

The process of groundwater flow through the underground is determined by the properties of the fluid, the properties of the porous media and the gradient of the hydraulic head. The ability of a fluid to flow through porous media is described by Darcy's law (6.1) and quantified by the Darcy velocity (Darcy, 1856)

$$q = -\lambda_f \nabla H \,. \tag{6.1}$$

q	specific discharge (Darcy velocity, Darcy flux)
λ_f	hydraulic conductivity of the porous medium
∇H	hydraulic gradient
H	hydraulic head

The specific discharge or Darcy velocity should not be confused with the microscopic velocities associated with the actual paths of water particles through the media. It is rather a fictitious velocity defined as the fluid flow per unit cross-sectional area of a porous medium. In other words, there is an assumption that flow occurs across the entire cross-section of a soil sample, while in real, flow actually takes place only through interconnected pore channels (Clauser (ed.), 2003).

In order to obtain the transient ground water flow, the equation of mass conservation has to be used along with the Darcy's law. The law of mass balance (6.2), also called the Lomonosov-Lavoisier law, states that mass in a closed system will remain constant, no matter what processes are acting inside of the system. In other words, it describes the balance between fluid inflow and outflow. Law of mass balance:

$$\nabla q = -S_s \frac{\partial H}{\partial t} + W_f \,, \tag{6.2}$$

S_s	specific storage coefficient
W_f	source term (positive for sources and negative for sinks)
t	time.

After substituting (6.2) into (6.1), the governing equation of groundwater flow can be expressed as

$$\nabla\left(\lambda_f \nabla H\right) = S_s \frac{\partial H}{\partial t} - W_f \,. \tag{6.3}$$

For a subsurface system saturated with a fluid, the hydraulic conductivity can be defined as follows (Bear, 1972)

$$\lambda_f = \frac{\rho_f g}{\mu_f} k \,. \tag{6.4}$$

ρ_f	density of the pore fluid
μ_f	dynamic viscosity of the pore fluid
g	gravitational acceleration
k	permeability

The general groundwater flow equation, which mathematically describes the movement of groundwater through an aquifer, can then be written as

$$\nabla\left(\frac{\rho_f g}{\mu_f} k \cdot \nabla H\right) = S_s \frac{\partial H}{\partial t} - W_f . \tag{6.5}$$

The hydraulic head (H) represents here the primary variable and is defined as

$$H = \frac{P}{\rho_0 g} - z . \tag{6.6}$$

P	pressure
ρ_0	reference density given at corresponding reference values of pressure
z	depth

In hydrogeologic practise, the driving force for groundwater flow is generally expressed in terms of the hydraulic head, which can be understood as the elevation of a water body above a particular datum level. Specifically, the hydraulic head can be explained as the energy possessed by a unit weight of water at any particular point (Allaby & Allaby, 1999). Groundwater movement is always in the direction of decreasing hydraulic head. The rate of movement on the other hand is dependent on the hydraulic gradient, which is the change in head per unit distance.

In the case of a transient flow, when the fluid inflow equals outflow +/- change in storage, the hydraulic head changes in time. For a homogeneous, but anisotropic aquifer the groundwater flow equations is

$$\lambda_{fx} \frac{\partial^2 H}{\partial x^2} + \lambda_{fy} \frac{\partial^2 H}{\partial y^2} + \lambda_{fz} \frac{\partial^2 H}{\partial z^2} = S_s \frac{\partial H}{\partial t} - W_f , \tag{6.7}$$

for a homogeneous and isotropic media

$$\frac{\partial^2 H}{\partial x^2} + \frac{\partial^2 H}{\partial y^2} + \frac{\partial^2 H}{\partial z^2} = \frac{S_s}{\lambda_f} \frac{\partial H}{\partial t} - W_f . \tag{6.8}$$

And finally, in the case of a steady-state, when the water inflow equals the outflow, the hydraulic head does not change in time. The groundwater flow equation in such case is

$$\frac{\partial^2 H}{\partial x^2} + \frac{\partial^2 H}{\partial y^2} + \frac{\partial^2 H}{\partial z^2} = 0 . \tag{6.9}$$

The temperature in a media is controlled by the heat transport equation, which is derived from Fourier's law (6.10) and the law of energy conservation (6.11)

$$q_T = -\lambda_T \nabla T \,. \tag{6.10}$$

q_T	heat flux
λ_T	thermal conductivity of a porous medium
∇T	temperature gradient
T	temperature

The law of conservation of energy states that the total amount of energy in an isolated system remains constant over time

$$\nabla q_T = -c^p \rho \frac{\partial T}{\partial t} + W_T \,. \tag{6.11}$$

$c^p \rho$	heat storage of a porous medium
t	time
W_T	heat source term

Heat storage ($c^p \rho$) is calculated as follows

$$c^p \rho = \phi c_f^p \rho_f + (1-\phi) c_s^p \rho_s \,. \tag{6.12}$$

ϕ	porosity
c_f^p	specific heat capacity of fluid
c_s^p	specific heat capacity of rock
ρ_f	fluid density
ρ_s	rock density

And finally, substituting (6.11) into (6.10) results in the transient heat transport equation

$$\nabla(\lambda_T \nabla T) = c^p \rho \frac{\partial T}{\partial t} - W_T \,. \tag{6.13}$$

For the different types of aquifer (homogeneous anisotropic, isotropic), the heat transport equations can be reformulated just as the groundwater flow equations (6.7) and (6.8). Also analogically, in the case of steady-state conditions, the heat transport equation is

$$\frac{\partial^2 T}{\partial x^2} + \frac{\partial^2 T}{\partial y^2} + \frac{\partial^2 T}{\partial z^2} = 0 \,. \tag{6.14}$$

In order to solve the groundwater flow and the heat transport partial differential equations, SHEMAT uses the finite difference (FD) method. Numerical models based on the FD method calculate values at discrete points in space (nodes). SHEMAT uses a block-centered grid, where nodes are located at the centre of the grid cells. Material properties have to be specified at each node and all kinds of flow (fluid, heat, mass) are calculated across the interfaces separating the cells (Clauser, 2003).

For the calculation of a model with a steady-state flow, only the boundary conditions are needed. However, in the case of transient fluid flow, additionally to boundary conditions, also the information concerning the initial conditions is required. In order to provide the initial conditions (the hydraulic head values and temperatures) a steady-state case can be calculated first. In SHEMAT-Suite, boundary conditions required for the solution of the heat transport and groundwater flow equations can be specified in respect to the hydraulic head and temperature for all outer model boundaries.

Implemented in the code are the following boundary types:

Dirichlet hydraulic head / temperature values are known along the boundary

Neumann requires specification of Darcy / heat fluxes along the boundary

The Neumann no-flow boundary conditions belong to the most commonly used boundary conditions in reservoir simulations. Here, the reservoir is described as a closed system, in which fluids and heat can not flow over the boundaries (are hydraulically and thermally closed).

6.2 Hydrothermal Modelling of the KTB Site

The number of boreholes penetrating the crystalline crust into depths above 5000 m is relatively small. For this reason, the 9101 m deep KTB drillhole provides valuable insight into thermal and hydraulic behaviour of the crystalline continental crust.

As mentioned before, the simulation software requires material properties specified at each node of the model. Even though the available seismic data contain a lot of detailed information about geological and tectonic features of the site, the contribution concerning petrophysical parameters of the rock is limited. No exact absolute parameter values could be estimated solely from seismic cross-sections. However, with the help of seismic data analysis, it was possible to define zones of relative values. Identification of the different main parameter units has been described in Chapters 4.1 Division of the Dataset into Main Lithological Units, 4.2 Zone of Erbendorf-Vohenstrauß and 5.4 Fracture Connectivity.

Absolute values to be assigned to the parameter units were collected from a number of published articles (Berckhemer et al., 1997; Jobmann & Clauser, 1994; Kohl & Rybach, 1996; Clauser et al., 1997; Lehman et al., 1998; Flores et al., 2001) and adjusted in cooperation with R. Pechnig (personal communication, 2010). For the Zone of Erbendorf-Vohenstrauß, as the only lithological unit at the KTB site penetrated by the borehole, petrophysical parameters were measured directly. Table 6.1 lists mean values of chosen parameters for the two main rocks components of the ZEV: gneisses and

metabasites. The values were calculated from the high amount of data resulting from measurements on cuttings recovered from the KTB-HB drillhole. Starting values were adjusted during the forward simulation process in order to yield the desired result.

Tab. 6.1: *Arithmetic mean values and standard deviations (±) of gneiss (sum of the contents of biotite gneiss, chlorite gneiss, cataclastic gneiss and muscovite gneiss) and metabasite (sum of the contents of amphibolite, calcsilicate amphibolite, garnet amphibolite and cataclastic amphibolite). Only samples containing more than 90% of gneiss and metabasites are listed. The number of data samples is given in brackets (Emmermann et al., 1995).*

	gneiss	**metabasite**
density g/cm^3	2.737 ± 0.022 (1081)	2.889 ± 0.044 (979)
natural gamma ray activity c/(s kg)	50.87 ± 5.01 (656)	23.32 ± 7.48 (731)
potassium %	2.242 ± 0.246 (464)	0.882 ± 0.423 (596)
uranium ppm	2.786 ± 0.442 (464)	0.975 ± 0.558 (596)
thorium ppm	7.882 ± 0.956 (464)	2.450 ± 1.507 (596)
heat production $\mu W/m^3$	1.493 ± 0.186 (466)	0.531 ± 0.276 (602)
log(susceptibility) 10^{-3} SI	0.412 ± 0.23 (1081)	0.013 ± 0.41 (979)
susceptibility 10^{-3} SI	0.387	1.030
thermal conductivity W/(m K)	3.43 ± 0.23 (211)	2.59 ± 0.21 (198)

Gneisses of the ZEV exhibit a strong foliation and therefore thermal conductivity and permeability could not be assumed to be isotropic. The highest values of these properties can be found in the direction parallel to foliation and lowest in the direction perpendicular to foliation. Because of the computational method of the SHEMAT modelling software, it was necessary to project the direction of foliation and thus also the direction of highest conductivity and permeability values onto the axes of the used grid (Fig. 6.1). However, the favourable orientation of the KTB data block in which the general direction of one of the foliation axes is aligned with the y-axis of the grid, enabled the foliation axes approximation without significant losses in accuracy. For this reason, to depict the value in a particular direction, lower indexes x,y,z have been added to the symbols of the mentioned rock properties (for example k_x, k_y, k_z).

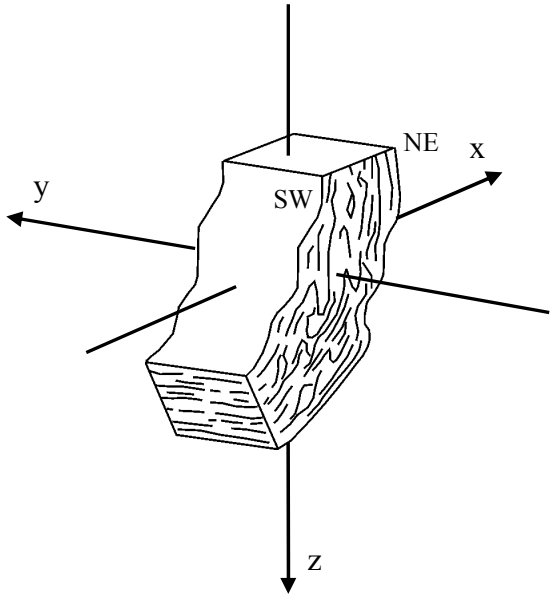

Fig. 6.1: *Schematic sketch of the gneiss foliation with the directions of data cube axes (after Harjes et al., 1997).*

Core samples recovered from the two KTB boreholes composed of gneisses and metabasites show a considerable amount of permeability anisotropy (Fig. 6.2). Permeability parallel to foliation showed to be one magnitude higher (mean value $2.7 \times 10^{-19} m^2$) than permeability perpendicular to foliation (mean value $2 \times 10^{-20} m^2$) (Huenges et al., 1997).

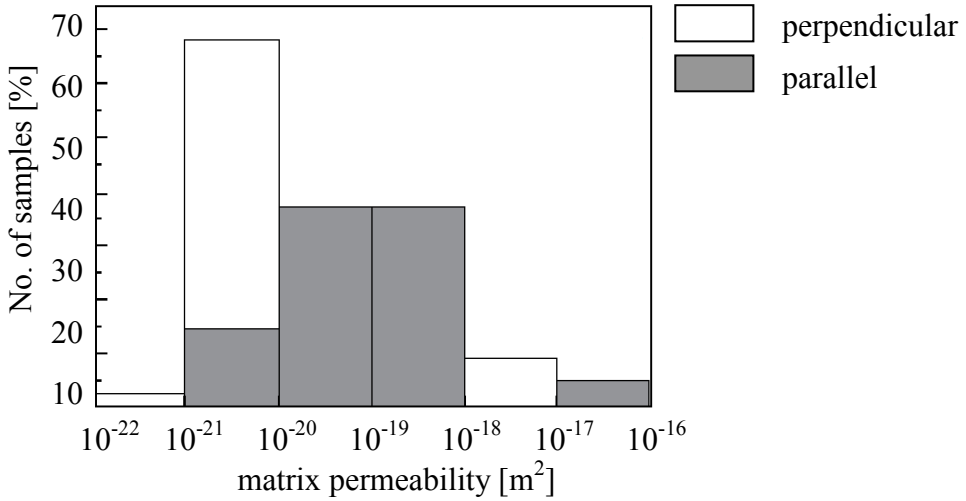

Fig. 6.2: *Permeability values measured on cores from depths up to 4 km of KTB-VB and 7.4 km depth KTB-HB. The measurements were performed perpendicular and parallel to the foliation of the gneissic rock (Huenges et al., 1997).*

6.2.1 Hydrothermal Simulations of the "Regional" Model

As already mentioned, with the aim to provide boundary condition information, the first in the process of heat production simulation is the calculation of thermal and hydraulic conditions of an area larger than the actual area of interest. Chapter 6.2.1 describes simulations of the whole area of the KTB site divided into several steps. Each of the presented models is equidistantly discretised with 300 m gridpoint distance and has a fixed size 17.7 km x 16.8 km x 9.0 km. Concerning the depth in particular, this is a considerably smaller area than the one covered by 3-D reflection seismic measurements. In the case of a survey aimed on geothermal energy production, it showed to be unnecessary to calculate a model incorporating great depths. Also, the computational effort increases considerably with every additional grid cell and therefore, to keep the computation time under a reasonable limit, it is necessary to focus only on the relevant area. Although a model incorporating also deeper sections might bring further information, the cost-benefit ratio in the case of geothermal energy utilization is presently low.

One of the questions which needed to be addressed before starting the simulations is concerning boundary conditions of the model. Taking into account the geological

situation at the KTB area, it can be claimed that no major conductive heterogeneities are present at the lateral boundaries of the model and thus it is possible to apply the no-flow lateral boundary conditions. In order to support and also verify these assumptions, tests of models with different boundary conditions have been carried out. As expected, because of the lack of conductive heterogeneities and additionally the considerable distance between the model boundaries and the evaluated area, no significant effect of boundaries could be observed in the different calculation results. Since a considerable amount of topography (Fig. 2.1) is present at area of interest, the hydraulic head values at the upper model boundary (surface) reflect these conditions (Mottaghy et al., 2011). The mean annual surface temperature 7.5 °C has been assigned to the upper boundary of the model. The factor controlling the bottom boundary is the bottom heat flow. During the modelling process, bottom heat flow has been adjusted so that the temperature at depth 9000 m would match the temperature measured in the KTB-HB at corresponding depth (~261°C (Fig. 2.4)).

Figures presented in this chapter are showing results of steady-state simulations of the site of the Continental Deep Drillhole at different stages. Starting from the simplest possible model, we show the minimum input information required to solve thermal conditions prevailing. The figures show the direction of calculated flow field represented by arrows and the Darcy velocity (specific discharge per unit area) as colour code. Additionally, from the resulting modelled temperature field we extract a temperature profile positioned at the exact location of the KTB-HB in order to compare it with temperatures measured in this borehole. Chosen for this comparison is the temperature log recorded in the KTB-HB in January 1998, since it provides the latest data. To observe temperature behaviour on a bigger scale, the linear temperature increase with depth has been subtracted and only the resulting reduced temperatures (T_{red}) are plotted:

$$T_{red} = T - \left(T_{surface} + \frac{\Delta T}{\Delta z} z \right). \tag{6.15}$$

Here $T_{surface}$ represents the surface temperature which is of the value 7.5 °C. The mean vertical thermal gradient $\frac{\Delta T}{\Delta z}$ is 0.028 K/m.

The thermal gradient 0.0275 K/m has been derived by Clauser et al. (1997) from bottom hole temperature measurements and temperature extrapolations based on temperature logs recorded during drilling pauses. This value has been adopted by a number of authors dealing with the topic of temperature measurements at the KTB site. Nevertheless, the undisturbed temperature gradient deviates from this value slightly. As suggested already by Rybach (1992) who corrected the temperature data using a palaeogeothermal correction and later by Wilhelm (2000), the undisturbed temperature gradient is 0.028 K/m.

6.2.1.1 Homogeneous Model

The 3-D hydrothermal simulations of the KTB area started with the simplest possible model, consisting of only one entirely homogeneous unit with the parameter values listed in Table 6.2.

Tab. 6.2: *Parameter values used during hydrothermal simulations of a homogeneous model.*

unit	th. conductivity [$Wm^{-1}K^{-1}$]	heat production [μWm^{-3}]	porosity [%]	permeability [m^2]
crystalline	3.0	1.2	0.8	1.0^{-19}

The crystalline unit shall represent a general crystalline rock of average petrophysical properties. To achieve the desired temperature 261°C at depth 9000 m, bottom heat flow density 63.55 mWm^{-2} was required. Due to the lack of any heterogeneity, the calculated flow field plotted for a SW-NE cross-section (Fig. 6.3) shows a completely homogeneous behaviour. It is necessary to mention that the low permeability values reflect in the calculated Darcy velocities, which are very low. The values of about 1^{-18} m/s are about 3^{-8} mm in a year. Shape of the reduced temperature curve illustrates that a completely homogeneous model is clearly not suitable to explain the thermal field of the area.

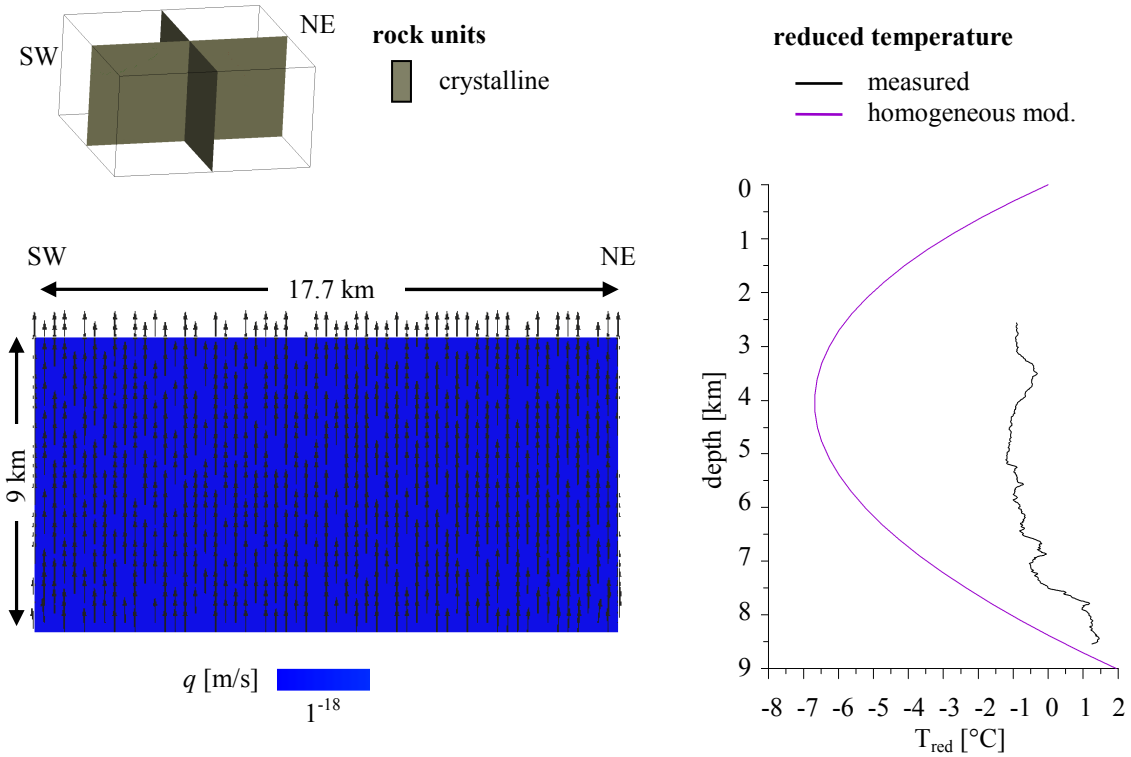

Fig. 6.3: *Calculated flow field of a model consisting of a completely homogeneous unit (left) and the comparison of reduced temperatures of the modelled and logged temperature (right). Reduced temperatures were calculated using the formula (6.15).*

6.2.1.2 Homogeneous Model with Topography

Figure 6.4 shows again the simulation of a homogeneous model (parameter values listed in Table 6.1), now with the consideration of the local topography (Fig. 2.1). Since the altitude difference between the highest and the lowest point at the KTB site reaches up to 300 m, the effect of topography onto the hydraulic head and consequently also on the flow field, should not be neglected. Jobmann & Clauser (1994), who performed 2-D calculations along a profile crossing the KTB site also emphasised the importance of topography driven hydraulic impact onto the temperature field.

Figure 6.4 shows that Darcy velocities increased by several orders of magnitude due to the change of hydraulic head. We can state that the effect caused by topography is strongest within the upper 1000 m. The flow pattern is following the path from areas of higher altitude (head), located in the SW of the site, towards the lower areas in the NE. Considering its rather significant influence, the topography effect has been taken into account in all of the following models.

Due to the lack of any local thermal inhomogeneity, the reduced temperature curve is of the same shape as in the case of the simple homogenous model. Also, the bottom heat flow density value did not change.

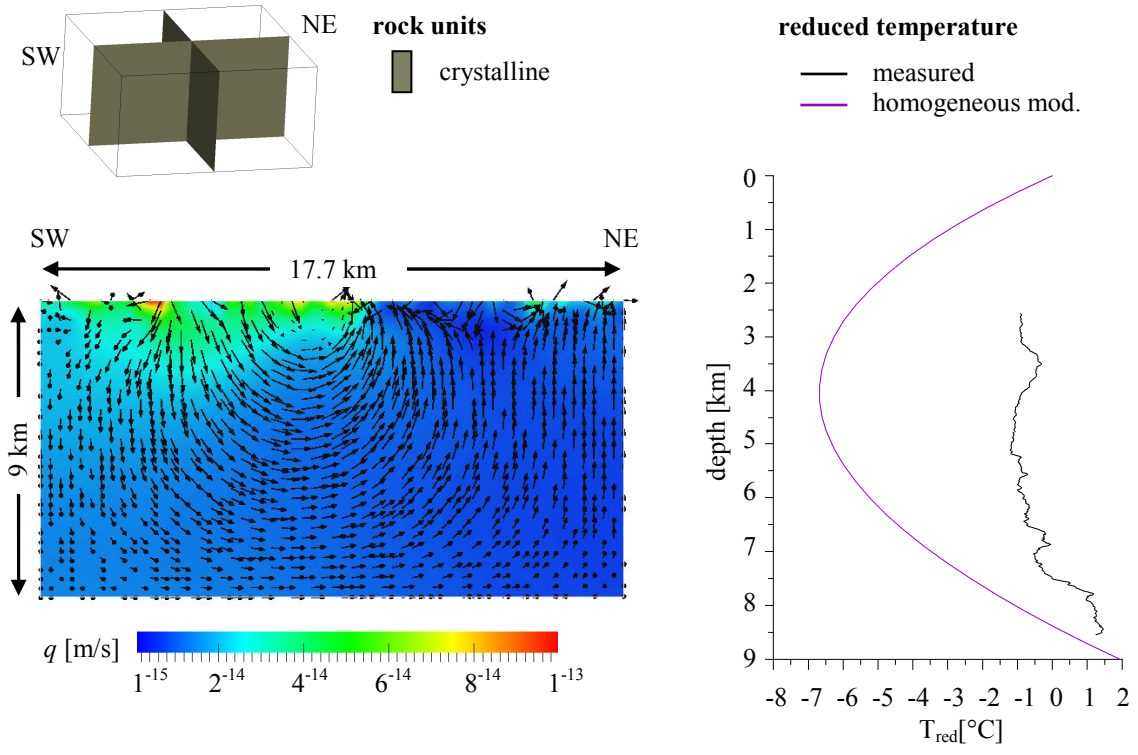

Fig. 6.4: *Calculated flow field of a model consisting of a completely homogeneous unit with the consideration of topography (left) and the comparison of reduced temperatures of the modelled and logged temperature (right).*

6.2.1.3 Model Incorporating the Granitic Unit

To understand the effects of each lithological unit separately, models consisting of only the crystalline unit and each of the main units (sediments and granites) have been calculated and are presented in the following chapters. Aim of the modelling process is to show the thermal effect of each of the rock units. Parameter values of the "background" crystalline unit do not change. Furthermore, permeability and porosity values are still being kept constant and relatively low in the whole model.

The granitic unit, consisting to the majority of the Falkenberg granite is located in the north-eastern part of the KTB site and reaches up to 7000 m depth. While granites show high values of heat production, which is up to 90% caused by the presence of U and Th, their thermal conductivity is relatively low. As already mentioned, absolute values of petrophysical properties used during the hydrothermal simulations were taken from the literature and are listed in the Table 6.3.

Tab. 6.3: *Parameter values used during simulations of a simple model consisting of two units: the granites and the crystalline unit. Porosities and permeabilities are being kept constant within the whole model.*

unit	th. conductivity [$Wm^{-1}K^{-1}$]	heat production [μWm^{-3}]	porosity [%]	permeability [m^2]
crystalline	3.0	1.2	0.8	1.0^{-19}
granites	2.8	6.3	0.8	1.0^{-19}

The thermal effect of the granitic unit presented in Figure 6.5 brings more complexity into the previously homogeneous flow field. Darcy velocities are now slightly higher in the NE section of the model, at the location of the granitic unit. Reduced temperature curves calculated during the previous steps are kept in the graph to allow a visual comparison with the other models. Temperature field of the area increased notably and reduced temperatures show already a slightly better correlation (max. 4°C mismatch) with the measured temperature curve. Still, it is obvious that the effect of the granitic unit alone is not sufficient to describe the thermal field of the KTB site correctly. Bottom heat flow density changed to the value 61.90 mWm^{-2}.

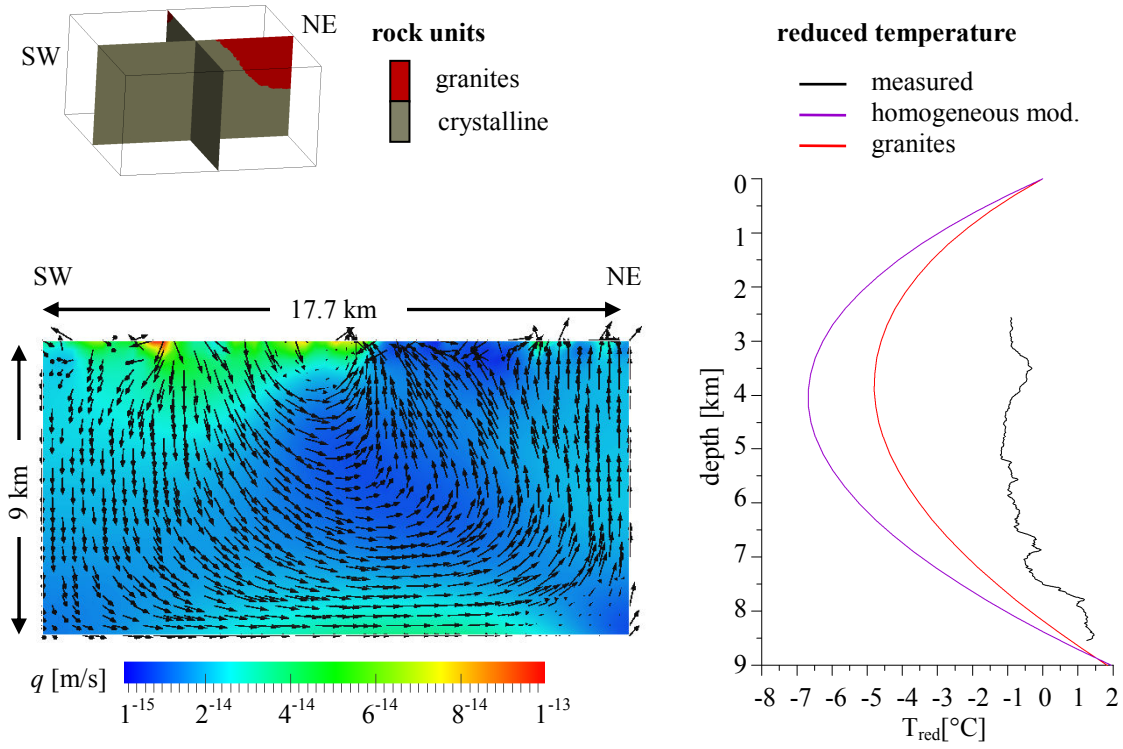

Fig. 6.5: *Calculated flow field of a model consisting of two rock units: the granites and the crystalline unit (left) and the comparison of reduced temperatures of the modelled and logged temperature (right).*

6.2.1.4 Model Incorporating the Sedimentary Unit

The second main lithological unit located at the KTB area are the foreland sediments in the south-west. Sedimentary layers here are up to 3000 m thick and consist of horizons of Permo-Mesozoic age. According to literature, which describes properties of sediments in the Oberpfalz, the heat production, as well as thermal conductivity of this lithological unit is low (Tab. 6.4). Even though porosity and permeability values of sedimentary layers are naturally higher than of crystalline rocks, at this stage of modelling we still assume homogeneously low porosities and permeabilities for the whole model.

Tab. 6.4: *Parameter values used during simulations of a simple model consisting of only two units: sediments and the crystalline background. Porosities and permeabilities are being kept constant within the whole model.*

unit	th. conductivity [$Wm^{-1}K^{-1}$]	heat production [μWm^{-3}]	porosity [%]	permeability [m^2]
crystalline	3.0	1.2	0.8	1.0^{-19}
sediments	2.0	0.7	0.8	1.0^{-19}

The presence of sediments increased Darcy velocities in the SW part of the model (Fig. 6.6) and changed the flow direction. Although volume of the sedimentary unit is smaller and heat generation considerably lower compared to the granites, the final effect on the temperature field is larger (max. 3°C mismatch). This fact can be explained by the interaction of several factors, from which the main influence may have the position of the sedimentary unit within the flow field activated by the hydraulic head and thermal rock properties. Bottom heat flow density required to reach the necessary temperatures was 61.6 mWm^{-2}.

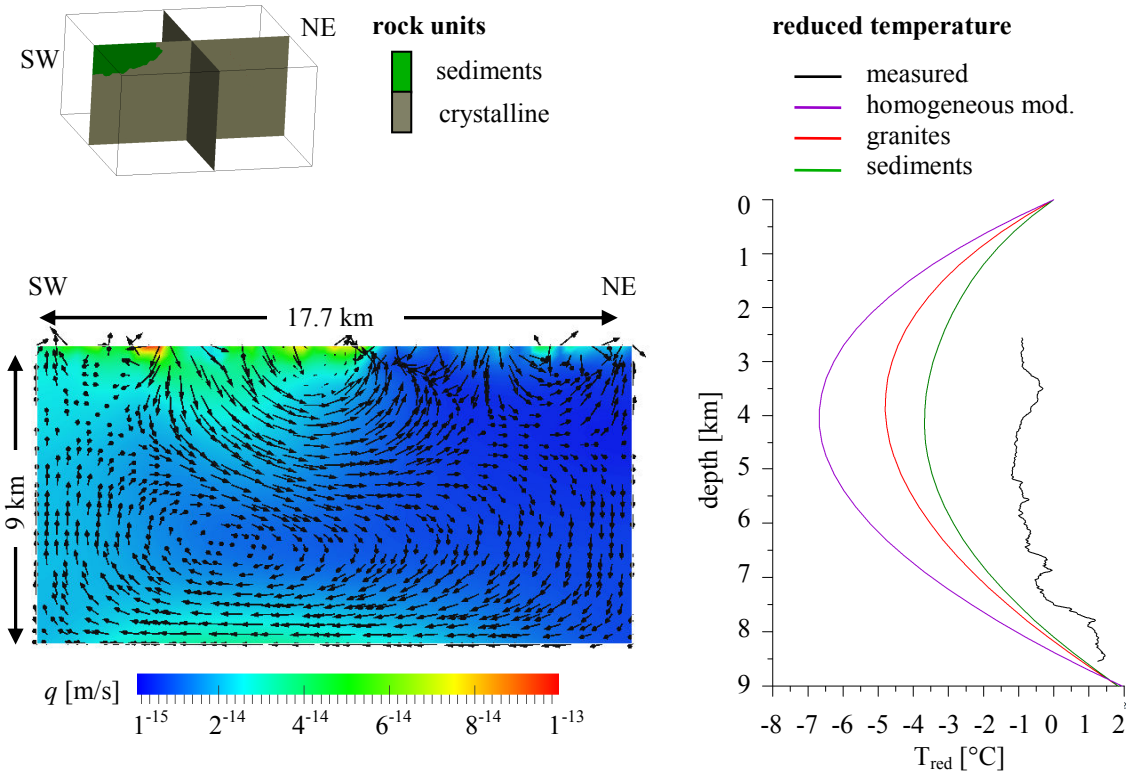

***Fig. 6.6**: Calculated flow field of a model consisting of two rock units: sediments and the crystalline background unit (left) and the comparison of reduced temperatures of the modelled and logged temperature (right).*

6.2.1.5 Model Incorporating the Granitic & Sedimentary Unit

In the next model effects of the two previously presented main lithological units are considered simultaneously and their combined effect on the thermal field is calculated. The presence of sedimentary and granitic unit at the KTB site is known and can not be questioned. Also their general shape and extent can be identified with the help seismic data and a priori information as described in the Chapter 4. These units can be considered as constants in the structural model of the KTB site.

Values of thermal conductivity and heat production for sediments and granites were taken from literature, consulted with R. Pechnig during personal communication in 2010 and adjusted during the modelling process (Tab. 6.5).

Tab. 6.5: *Parameter values used during simulations of a model consisting of three units: granites, sediments and the crystalline "background". Porosities and permeabilities are kept homogeneous in the whole volume.*

unit	th. conductivity [$Wm^{-1}K^{-1}$]	heat production [μWm^{-3}]	porosity [%]	permeability [m^2]
crystalline	3.0	1.2	0.8	1.0^{-19}
granites	2.8	6.3	0.8	1.0^{-19}
sediments	2.0	0.7	0.8	1.0^{-19}

The flow field presented in Figure 6.7 combines flow patterns of the separate sedimentary and granitic models. Due to the still low homogenous porosities and low permeabilities, Darcy velocities do not reach significant magnitudes. The modelled reduced temperature curve is already very close to the curve of measured reduced temperatures (max. 1.5°C mismatch), nevertheless the correlation is still not completely satisfactory. Bottom heat flow density of this model reached the value 59.70 mWm^{-2}.

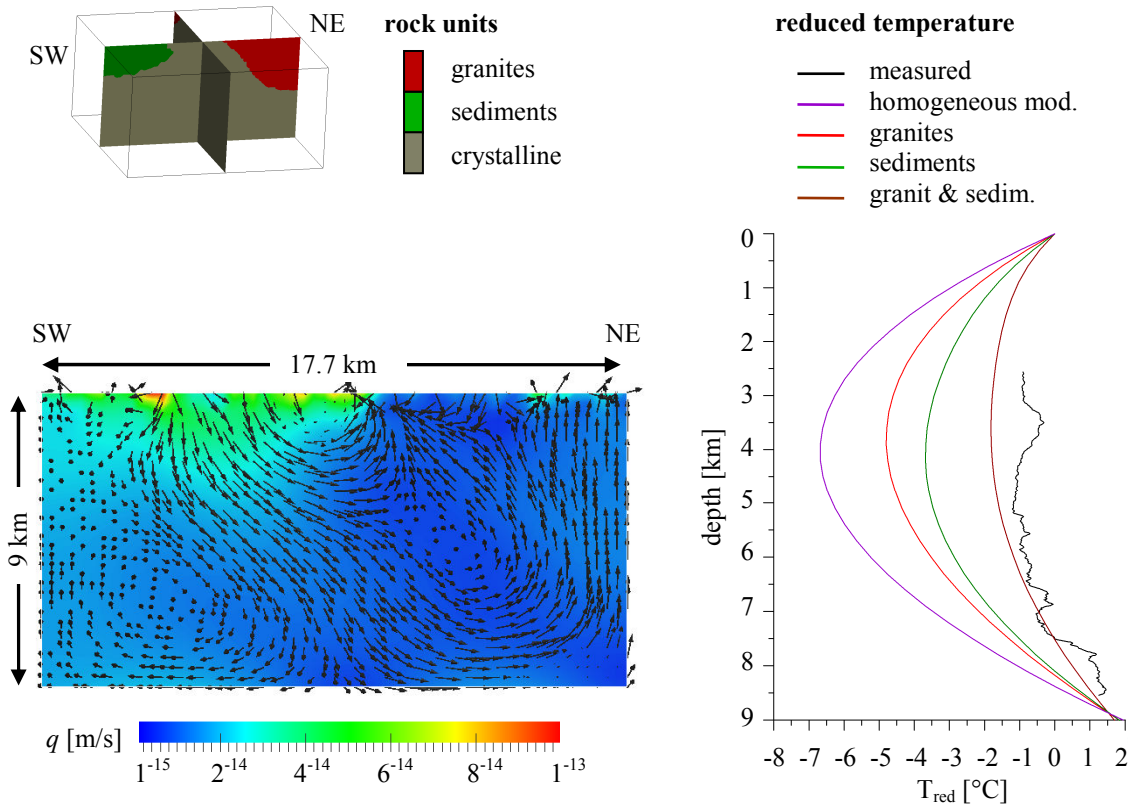

Fig. 6.7: *Calculated flow field of a model consisting of the three main rock units of the KTB site (left) and the comparison of reduced temperatures of the modelled and logged temperature (right).*

On the basis of reduced temperature curves we can say that especially the upper section of the calculated temperature field is showing lower temperature values than those which were measured in the field. This discrepancy can be solved by adding realistic porosity values to the sedimentary unit. During the simulations, porosity of 7% assumed for the whole sedimentary unit, provided best results (Tab. 6.6). Because of the higher porosities, bottom heat flow density had to be increased to the value 63.00 mW/m^2 in order to reach the temperature 261°C at 9000 m depth.

Tab. 6.6: *Parameter values used during simulations of a model consisting of three units: granites, sediments and the crystalline. Porosities of the sedimentary unit are adjusted to reflect a realistic value, while permeability values are still homogeneous in the whole volume.*

unit	th. conductivity [$Wm^{-1}K^{-1}$]	heat production [μWm^{-3}]	porosity [%]	permeability [m^2]
crystalline	3.0	1.2	0.8	1.0^{-19}
granites	2.8	6.3	0.8	1.0^{-19}
sediments	2.0	0.7	7	1.0^{-19}

The fact that the flow field (Fig 6.8) did not change compared to the model with the two main lithological units, but homogenous porosities, is due to the low permeabilities which are still same in the whole model.

If we observe the modelled and the measured reduced temperature (less than 1°C mismatch), we can state that at this point of the modelling process, the temperature field of the KTB site can be considered as solved. The general shape of measured temperature curve can be reproduced by taking into consideration the two major lithologic units: sediments and granites (Fig. 6.8). Of course the coarse grid, the relatively large units and the fact that the temperature profile is located within the still homogenous crystalline unit results in a reduced temperature curve, which is smooth and does not reflect any local structures. Nevertheless, simulation results lie in the interval of temperature measurement precision and thus can be considered as satisfactory.

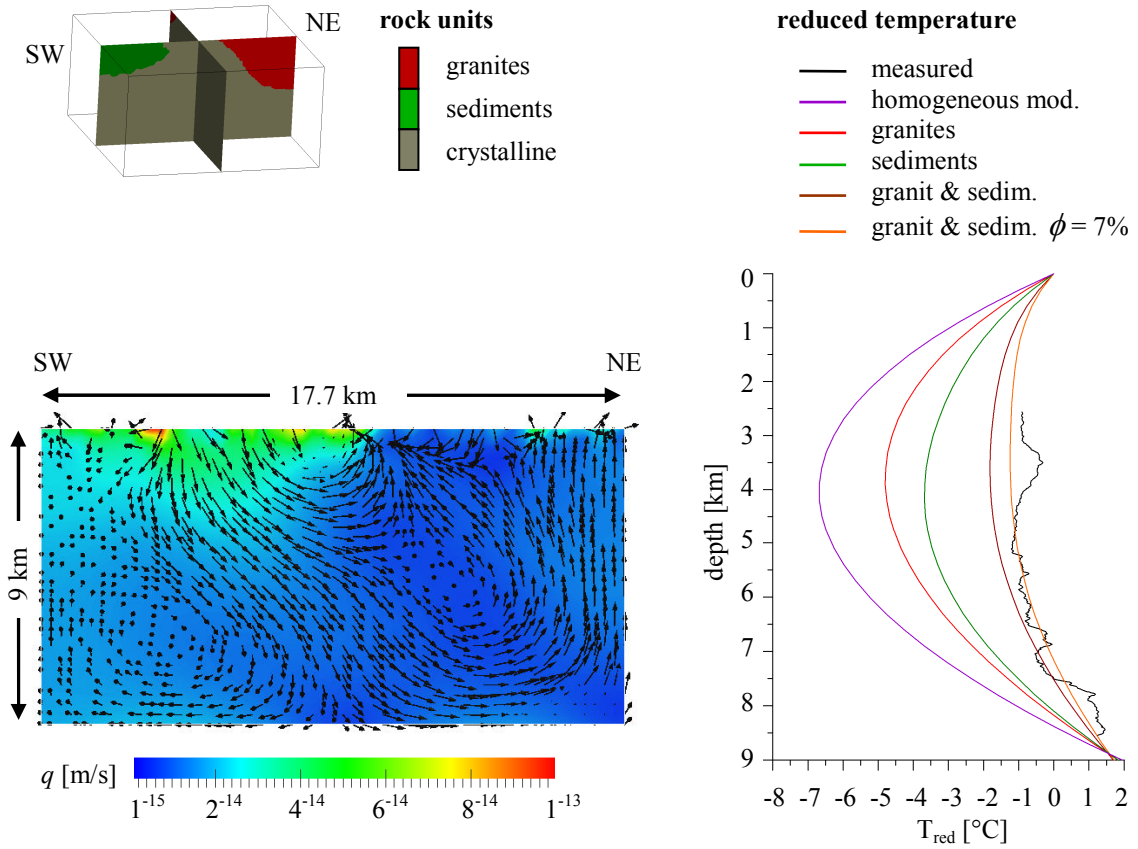

Fig. 6.8: *Calculated flow field of a model consisting of three main rock units of the KTB site: granites, sediments and the crystalline background unit (left) and the comparison of reduced temperatures of the modelled and logged temperature (right). Porosity of the sedimentary unit is 7 %.*

6.2.1.6 Model Incorporating All Lithological Units at the KTB site

Although hydrothermal simulations of the KTB site can be declared as completed, seismic data provided further information which can be included into the simulations. These additional data might improve modelling results.

With the help of synthetic seismograms based on the Monte Carlo method (Chapter 4.2), it was possible to identify zones with rather metabasic and rather gneissic rocks within the large Zone of Erbendorf-Vohenstrauß. Incorporation of this information into the structural model of the site enabled to assign a more detailed structure to the up to now homogenous crystalline background unit. During this modelling step, permeabilities and porosities are still constant in the whole data cube; the only exception is the sedimentary unit, where it proved to be important to assign a realistic porosity value.

The Zone of Erbendorf-Vohenstraß was the only lithological unit penetrated by the KTB boreholes. Thanks to the many tests and measurements performed on the recovered samples, we have accurate data concerning the properties of the ZEV rocks. As listed in Table 6.7, we consider also the anisotropic behaviour of gneisses. The strong foliation of gneisses has a large effect on the thermal conductivity and it can not be considered as isotropic. As mentioned in Chapter 6.2, we distinguish between the vertical (λ_{Tz}) and two horizontal (λ_{Tx} , λ_{Ty}) thermal conductivity values.

Tab. 6.7: *Petrophysical parameters used during hydrothermal simulations of a model consisting of all main lithological units which were identified on the basis of seismic data. The model includes also a more detailed definition of the rock units within the ZEV. In the case of gneisses, their anisotropic character is taken into account as well and we distinguish between thermal conductivities in x, y and z direction.*

unit	th. conductivity [$Wm^{-1}K^{-1}$]			heat production [μWm^{-3}]	porosity [%]	permeability [m^2]
granites	2.8			6.3	0.8	1.0^{-19}
sediments	2.0			0.7	7	1.0^{-19}
	λ_{Tx}	λ_{Ty}	λ_{Tz}			
gneiss steep	3.0	3.6	3.4	1.5	0.8	1.0^{-19}
gneiss intermediate	3.2	3.6	3.2	1.5	0.8	1.0^{-19}
gneiss near-horizontal	3.6	3.6	3.0	1.5	0.8	1.0^{-19}
gneiss & metabasite	3.2			1.2	0.8	1.0^{-19}
metabasite	2.5			0.8	0.8	1.0^{-19}

The calculated fluid flow does not differ noticeably from the one of the previous model, because of the homogeneous permeability and porosity values. On the other hand, differentiating the Zone of Erbendorf-Vohenstrauß into individual rock components had a considerable impact on the thermal field of the site. As seen in Figure 6.9, the curve of calculated reduced temperatures displays the local inhomogeneity represented by the gneissic and metabasic layers. The shape of the curve will be discussed in more detail in the following section. Bottom heat flow density of the value 62.3 mWm^{-2} has been used.

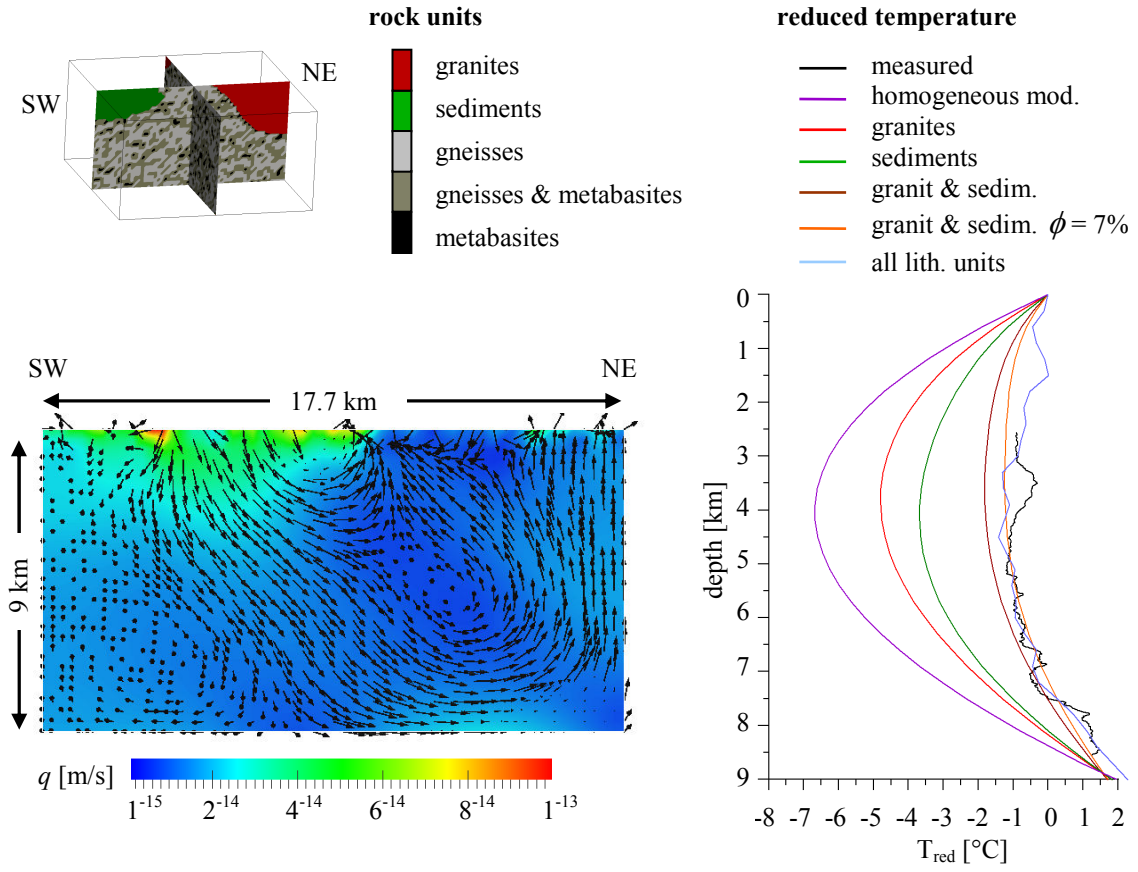

Fig. 6.9: *Calculated flow field of a model consisting of all main rock units identified at the KTB site, including a closely defined Zone of Erbendorf-Vohenstrauß (left) and the comparison of reduced temperatures of the model and the logged temperatures (right). Porosity of the sedimentary unit is 7 %.*

6.2.1.7 Model Incorporating All Lithological Units at the KTB Site with Inhomogeneous Porosity & Permeability

The last model, which is considered as the final model, incorporates all of the information acquired from the 3-D reflection seismic dataset. Input, which has not yet been incorporated in the previous models concerns the permeabilities. Up to now, the large-scale fault zone, as well as the middle-scale fractures, did not play any role in the modelling process. We now introduce to the model results of fracture connectivity calculations (Chapter 5) as new units of increased permeability and porosity values.

As described previously, matrix permeability of crystalline rock is too low to contribute in a noteworthy amount to fluid flow. Therefore, it is represented by a unit of very low permeability, in the final model marked with the number 4 (Tab. 6.8). Units 1 to 3 incorporate media fractured and faulted to a different level. Unit 1 stands for the large-scale fault zones, the downward continuations of the Franconian Lineament.

Permeability of this unit has been estimated to be the highest. Middle-scale fractures and zones affected to a high level by percolation are included in the unit 2. Unit 3 is also affected by percolation, but to a lower level.

Absolute values of thermal conductivities and heat production rates are same as in the previous model, values for the different permeability units have been proposed by R.Pechnig (personal communication).

***Tab. 6.8**: Final petrophysical parameters used during hydrothermal simulations of the regional model (0 m – 9000 m).*

unit	th. conductivity [$Wm^{-1}K^{-1}$]			heat production [μWm^{-3}]	porosity [%]	permeability [m^2]
granites	2.8			6.3		
sediments	2.0			0.7	7	
	λ_{Tx}	λ_{Ty}	λ_{Tz}			
gneiss steep	3.0	3.6	3.4	1.5		
gneiss intermediate	3.2	3.6	3.2	1.5		
gneiss near-horizontal	3.6	3.6	3.0	1.5		
gneiss & metabasite	3.2			1.2		
metabasite	2.5			0.8		
unit 1					1	10^{-16}
unit 2					0.8	10^{-17}
unit 3					0.7	10^{-18}
unit 4					0.7	10^{-19}

Modelling showed that porosities have to be kept low in all units except in sediments in order to achieve a good fit of temperatures. The now higher permeability values of the fracture network bring changes to the flow field behaviour (Fig. 6.10). Highest flow velocities can be found in the structures defined by highest permeabilities which also communicate hydraulically with the neighbouring structures. Still, the highest value of Darcy velocity is reaching only 10^{-12} m/s. This slow flow is also the explanation for no noticeable change in the temperature field. Reduced temperature curve does not differ from the one calculated in the previous model. Bottom heat flow density which was necessary for the correct temperatures is 60.20 mWm^{-2}.

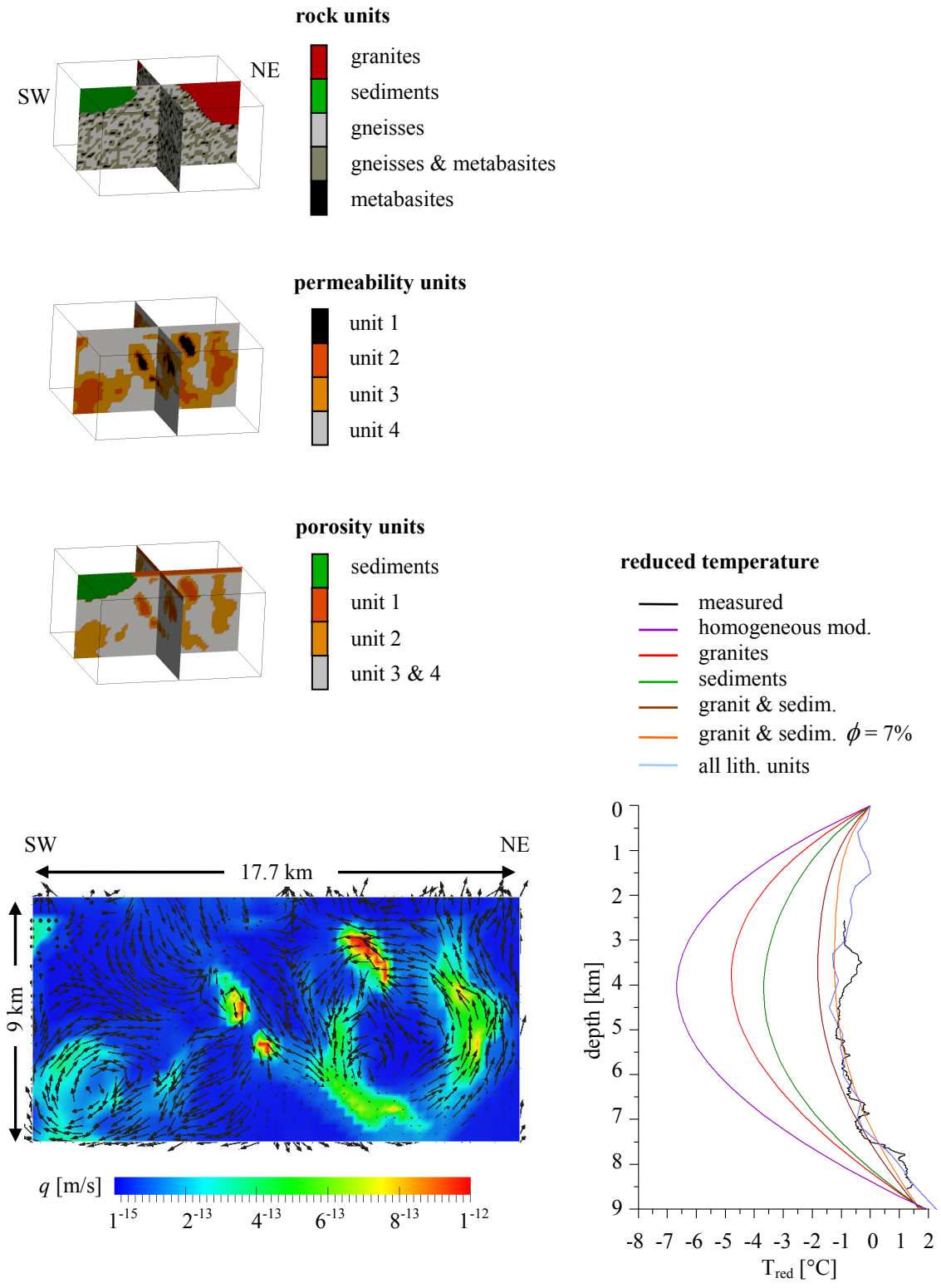

Fig. 6.10: *Calculated flow field of the final model consisting of all rock units identified at the KTB site including inhomogeneous porosities and permeabilities (left). Comparison of all reduced temperature curves calculated so far and the logged temperature (right).*

6.2.2 Hydrothermal Simulations of the Near-surface Section

The specific characteristics of KTB site's near-surface zone require additional attention. To evaluate the thermal field in the upper 0 – 4000 meters, we analyse the temperature log recorded in the pilot hole in February 1996. Temperature data from KTB-VB were used also for simulation verifications since they are more complete and more reliable than the temperatures coming from the KTB-HB (Kohl & Rybach, 1996).

As has been pointed out by Rybach (1992), the temperature profile shows a striking non-linearity (Fig. 6.11 left) caused by a near-surface low heat-flow zone. This zone has been discussed and studied by a number of authors (Rybach, 1992; Jobmann & Clauser, 1994; Wilhelm, 2000 etc.). From the possible reasons to which belongs the constant heat flow and with depth increasing thermal conductivities; constant thermal conductivities but a depth-dependent heat flow caused by fluid movement; or the presence of heat sinks, only palaeoclimatic effects can explain such non-linear behaviour (Rybach, 1992). Therefore, we add the palaeoclimatic effect determined by Burkhardt et al. (1989) to the temperature data measured in the pilot hole in February 1996 to receive a linear temperature–depth profile (Fig. 6.11).

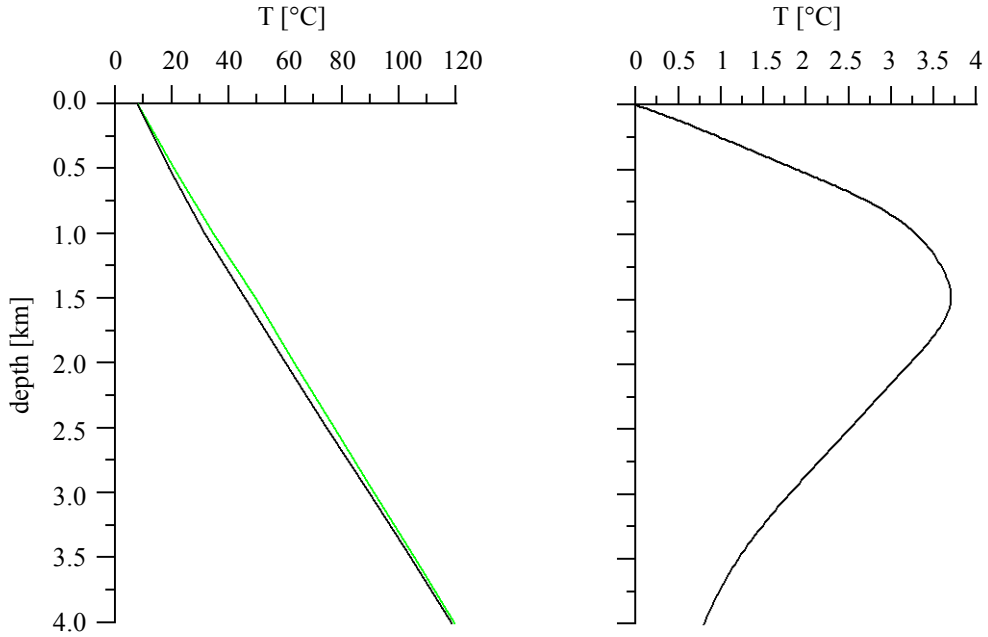

Fig. 6.11: *Left: temperature profile measured in KTB-VB uncorrected (black line) and corrected (green line) with the palaeoclimatic effect. Right: the subsurface palaeoclimatic effect calculated for the KTB site (Burkhardt et al., 1989) (after Rybach, 1992).*

In order to perform coupled hydro-thermal simulations of the upper section of the KTB site, we set up a separate structural model of a smaller vertical extent (4 km). Horizontal dimensions (17.7 km x 16.8 km), gridpoint distance (300 m) and the boundary conditions are same as in the previous "regional" model. We assume no-flow lateral and base boundary conditions. The upper boundary condition is fixed with the temperature 7.5°C and the hydraulic head is defined by the local topography. The correct hydraulic head is important, because the possibility that topography effects act as possible driving forces for advective transport is high especially in the uppermost 2000 m. Lithologically, the model consists of the same units as the previously shown model. We differentiate between sediments, granites and the ZEV units consisting of metabasites and the anisotropic gneisses. Absolute values used in the simulations are listed in Table 6.8.

At the position of the KTB pilot hole, we extract the modelled temperature-depth profile and with subtracting the linear trend, we calculate the reduced temperature. Firstly, we compare the simulated reduced temperature profile to the measured uncorrected temperature log. As seen in Figure 6.12, the misfit between the two curves is relatively high in the whole depth of the simulated area, reaching up to 4°C. It was not possible to reduce this temperature difference with any adjustments of petrophysical properties. On the other hand, correlation between the modelled and the measured temperature corrected for palaeoclimatic effects is highly satisfactory. Results of simulations confirm thus the statement about palaeoclimatic affected low heat-flow zone in the upper part of the KTB site.

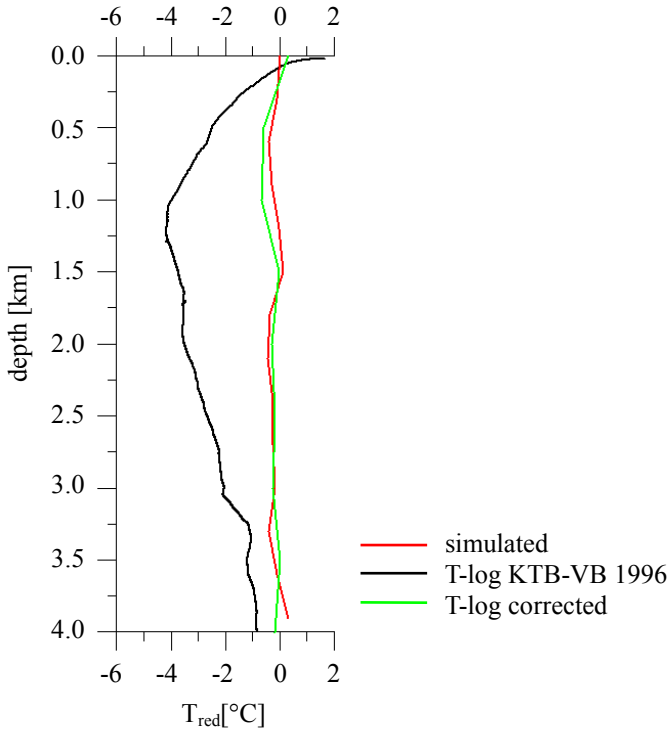

Fig. 6.12: *Simulation results of the near-surface model. We compare the modelled reduced temperature curve to the measured uncorrected reduced temperature and also to the temperature corrected with the palaeoclimatic effect. Reduced temperatures were calculated using the formula (6.15).The temperature log was recorded in the KTB-VB in February 1996.*

6.3 Summary

Boundary conditions for a detailed model of heat production are provided by solving the thermal and hydraulic conditions of a wider surrounding area. We searched for steady-state solutions of an equidistantly discretised model with no-flow lateral boundary conditions, a fixed surface temperature and an adjustable bottom heat flow density. The hydraulic boundary conditions of the upper boundary are given by the hydraulic head characterised by the local topography.

In several steps, we computed the thermal effect of the main KTB lithological units separately and in combination and compared the resulting reduced temperature profiles with values measured in the KTB-HB borehole. A satisfying match has been achieved already in a relatively early stage of the modelling process, with a model incorporating the granitic outcrops and the foreland sediments embedded in a general crystalline unit. While permeability values were kept low and homogeneous in the whole model, porosity values of the sedimentary unit had to be realistically high. More detailed definition of the Zone of Erbendorf-Vohenstrauß results in reduced temperature curves reflecting also the local inhomogeneity.

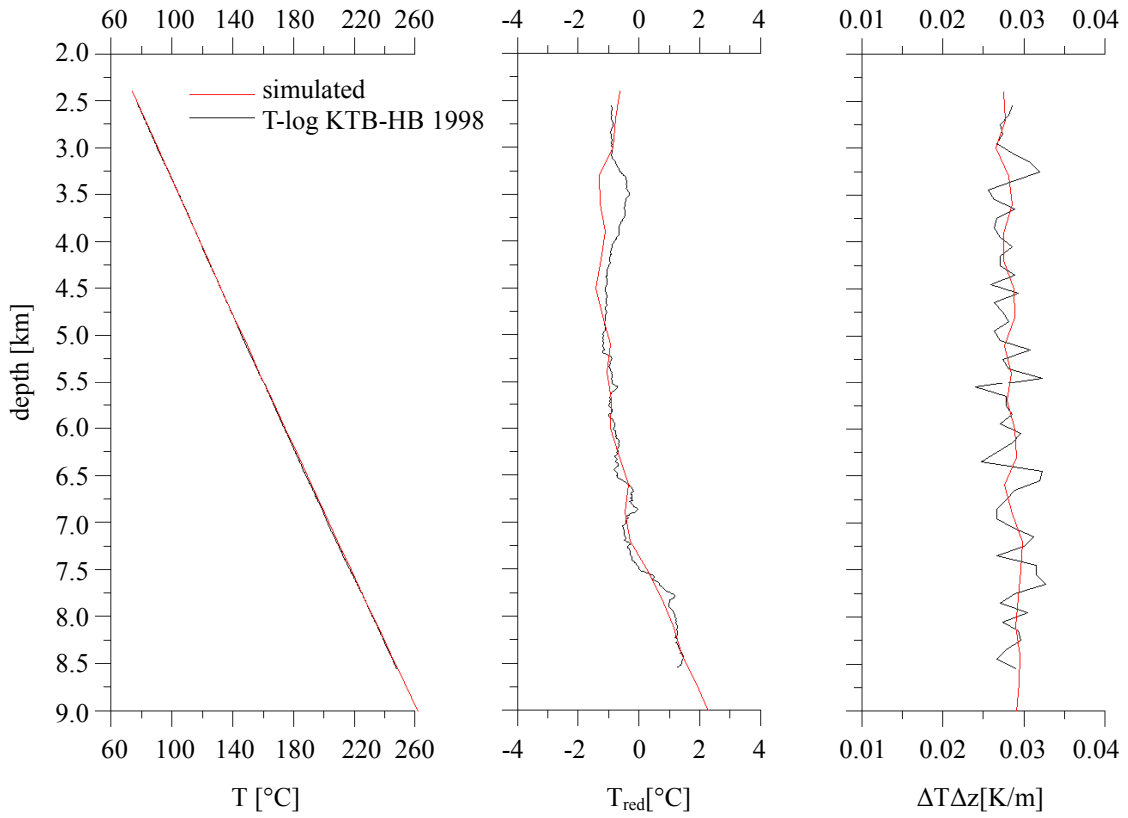

Fig. 6.13: *Comparison of the modelled and measured curves of temperature (T), reduced temperature (T_{red}) and vertical thermal gradient ($\Delta T/\Delta z$) in the case of the "regional" model up to the depth 9000 m. The temperature log was recorded in the KTB-HB in January 1998. Reduced temperatures were calculated using the formula (6.15).*

Figure 6.13 shows a comparison of measured and simulated temperature data in the case of the regional model. As it can be seen, a close fit has been achieved in the whole depth, except for the interval from 3000 m to 4000 m. The mismatch of measured and calculated temperatures is here slightly higher, reaching up to 1.2°C. Examination of the mentioned section in the lithological and tectonic interpretation of borehole data and the corresponding seismic cross-sections leads to the conclusion that the observed mismatch is caused by the presence of a fault. According to data collected in the KTB-HB, the borehole penetrated the fault zone Waldeck-Klobenreuth (in the seismic data named SE2) in the referred depth interval (Fig. 3.2). Seismic cross-sections show a highly disturbed zone as well, but here the presence of a fault is not as clear as it is in the case of the SE1 fault (Fig 6.14). Complexity of this depth interval clearly decreases the interpretation quality and leads also to lower accuracy concerning the generation of synthetic models and thus the identification of gneisses and metabasites.

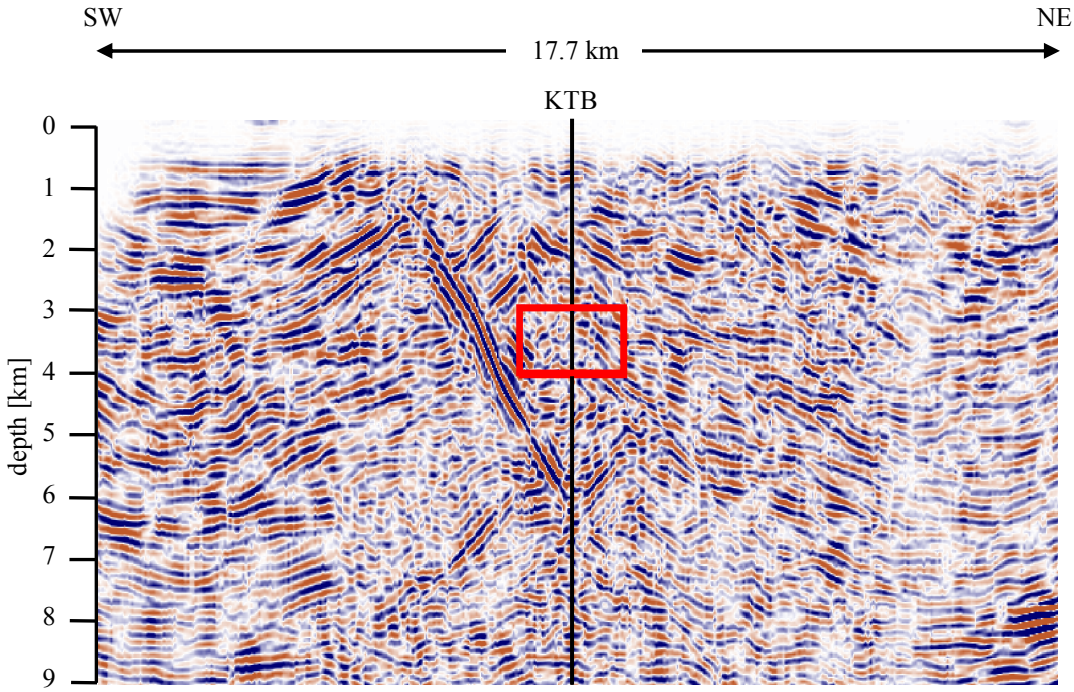

Fig. 6.14: *Seismic cross-section displaying area of hydrothermal simulations with the red rectangle marking the depth section of low fit between the measured and the calculated temperatures. This discrepancy seems to be caused by the presence of the SE2 fault.*

To reproduce the thermal field of the site correctly, it was necessary to keep the porosity values very low. During the process of modelling, it became clear that the thermal field of the area can be explained by a relatively simple conductive model. Low permeabilities and porosities cause low Darcy velocities with the highest values reaching only 10^{-12} m/s. One of the findings of the modelling process is that permeabilities prevailing in this particular crystalline environment are of values too low

to generate a hydraulic flow which would affect the thermal field notably. The only exception might be the SE2 fault, which seems to have an effect on the thermal field. These conclusions agree for example with the results of Clauser et al. (1997), who said that conduction is the dominating heat transport mechanism in the KTB region. In other words, the main effect on the thermal conditions at the site comes from the composition of the rock units and their thermal properties. Lithological units of the highest volume, namely sediments and granites have the highest effect on the temperature curve, while the Zone of Erbendorf-Vohenstrauß can be considered as one large unit. More detailed curve behaviour is reflecting the composition of the ZEV unit, the structure of alternating metabasites and gneisses. This means that in order to receive the closest possible fit, it is crucial to identify the extent of these units correctly and assign them correct petrophysical values. The final modelling results are presented in Figure 6.15.

Even though the presented model is of a coarse grid (300 m), it proved to be sufficient to incorporate the most important structures in a satisfactory way. A finer grid might offer more structural detail, but the related high computation time would not increase modelling efficiency.

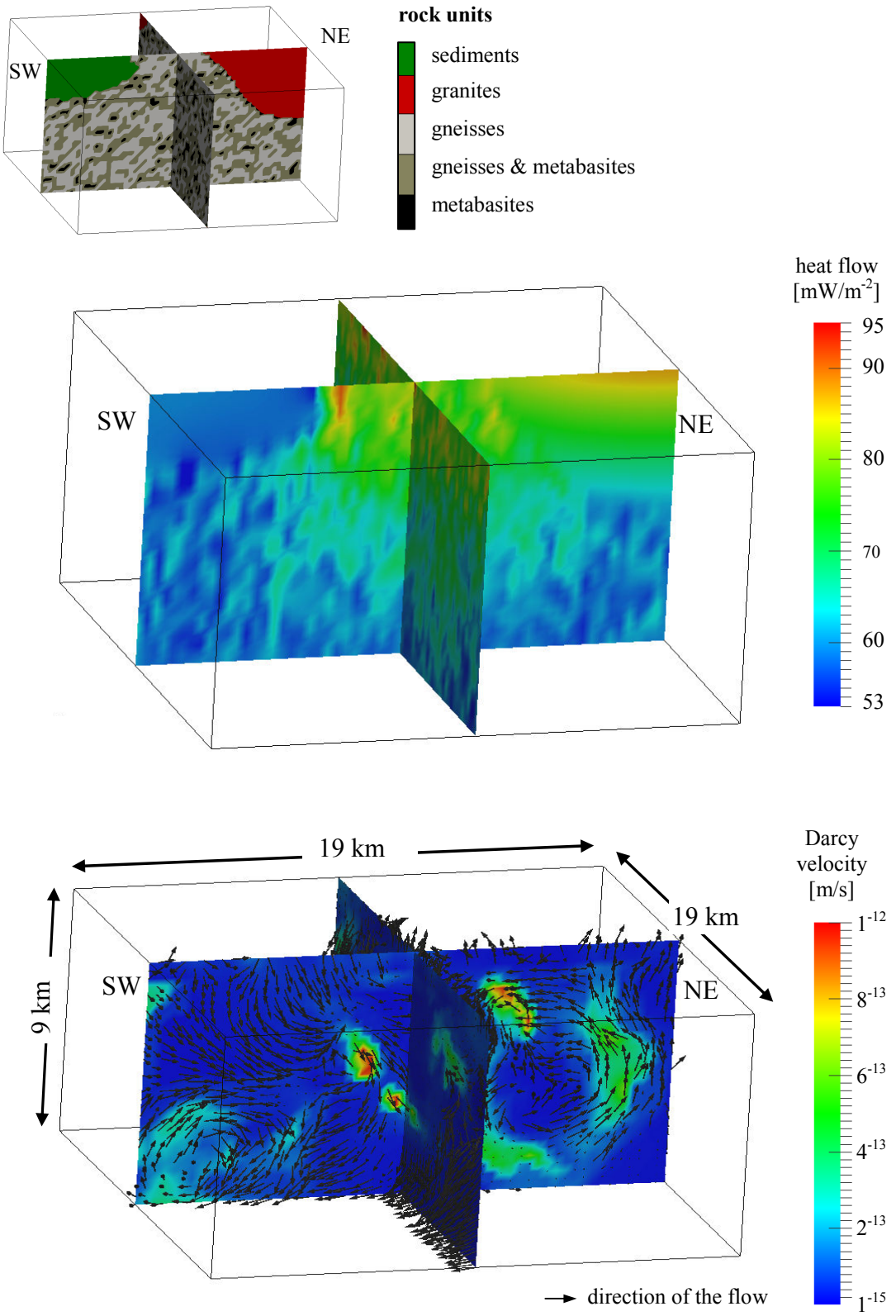

Fig. 6.15: *Heat flow density and the hydraulic flow field calculated for the "regional" model of the KTB site. This model incorporates all main lithological units and inhomogeneous permeability values.*

The upper 4000 meters of the KTB site are being treated slightly differently than the deeper sections. Temperature field here shows a rather peculiar feature, a non-linear behaviour caused by palaeoclimatic effects. The attempt to simulate corresponding conditions did not lead to satisfactory results. In order to receive a linear temperature-depth profile, we apply a correction for the palaeoclimatic effect to the measured temperature data. These data show a very good correlation with the modelled temperatures, which proves that the near-surface zone at the site is in fact affected to a considerable level by palaeoclimatic effects.

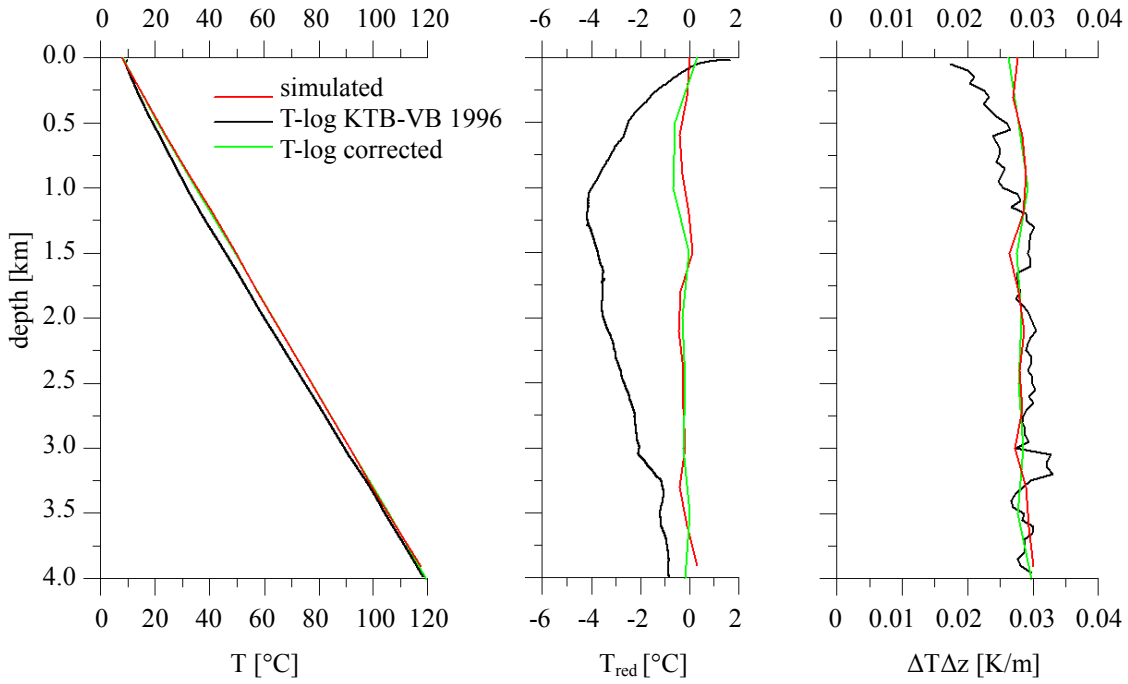

Fig. 6.16: *Comparison of the modelled and measured curves of temperature (T), reduced temperature (T_{red}) and vertical thermal gradient ($\Delta T/\Delta z$) in the case of the model of the upper 4000 m. The temperature log was recorded in the KTB-VB in February 1996. Reduced temperatures were calculated using the formula (6.15).*

6.4 Simulating a Geothermal Production Site

Understanding the hydrothermal conditions at the KTB site is only the first step towards answering the question of possible utilisation of the heat stored in the crystalline rock. Model of a smaller and more detailed two-well (doublet) system simulating heat extraction can help to assess the quality of the geothermal reservoir. The basic principle of a doublet system is simple. It incorporates two boreholes: the injection well, through which cool water is being pumped downwards into the geothermal system and the production well, which is extracting the water heated up in the underground. Depending on the amount of heat, the produced energy can be used for different purposes. At the KTB site, temperatures above 150°C have been measured in the deeper sections. These kinds of temperatures are the prerequisite for geothermal electricity production (Fig. 1.1).

Previous large-scale models show that permeability and porosity of the crystalline rock at the KTB site is low, resulting in very low Darcy flux. For the fluid to reach flow rates required for the functioning of a doublet system, permeability of rock needs to be enhanced. This can be achieved with hydrothermal fracturing. During this process, fluid which is injected under high pressure causes existing fractures to open or if not existent, creates new ones and thus increases the natural permeability. Rocks with interconnected fractures or pore spaces are more likely to result in a connected circulation system. Fluids then travel rather through the open fractures than through the rock matrix. This concept can be referred to as “hot dry rock” or “enhanced geothermal system” (Ngô et al., 2006).

Transmissivity is not the only important prerequisite for a functioning doublet geothermal installation. Since in a geothermal reservoir 95% of thermal energy is stored in the rocks (Ngô et al., 2006), heat transfer is happening between the circulating fluid and the underground rock. Consequently, injected cool fluid needs to travel through the rock for an amount of time necessary for sufficient heat exchange.

Taking into account the before-mentioned requirements, a smaller, more detailed model of the following characteristics has been selected out of the large data cube (Fig. 6.17). In order to make use of the favourable tectonic conditions of the KTB site, namely the large-scale fault system, both, injection and production boreholes have been located within the Zone of Erbendorf-Vohenstrauß, directly into the zone affected by the fault (Fig. 6.18). After hydraulic fracturing we can expect enhanced natural permeability of the fracture network to be of the order 10^{-13} m^2 to 10^{-15} m^2, which will ensure the necessary fluid flow. Model dimensions x = 3500 m, y = 3000 m, z = 3950 m, have been chosen so that they would cover the area affected by hydraulic fracturing. The model is discretised on an equidistant grid of the size 50 m x 50 m x 50 m. This corresponds to the resolution of the 3-D reflection seismic dataset. The modelled area is situated in depths from 3000 m to 6950 m, which will ensure production temperatures above 150°C.

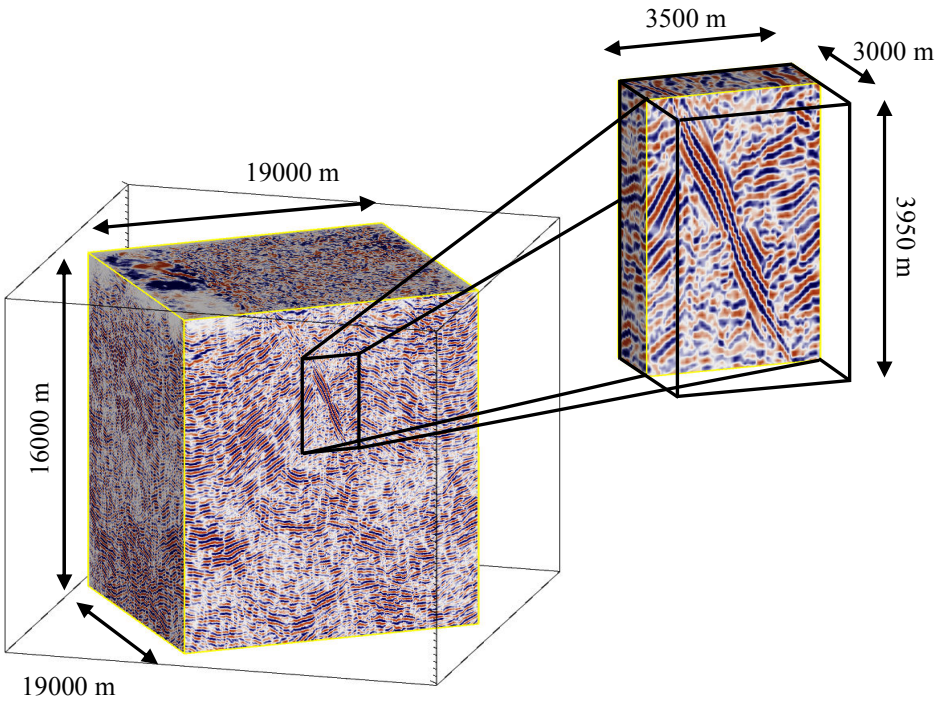

Fig. 6.17: *Location of the detailed model within the KTB data cube. Simulations of a doublet system were performed within this volume.*

Water injected into the injection well at 4700 m depth travels downwards to the production well, where it is pumped to the surface from 5700 m depth (Tab. 6.9). Vertical distance 1000 m and horizontal distance 750 m between the two boreholes should be sufficient to avoid the effect of early thermal breakthrough. Trajectory which the circulating water is going to follow should also provide sufficient time for the necessary heat exchange.

The heat production rate needs to be chosen carefully. Even though at human time scales geothermal energy can be classified as a renewable energy, excessive production can cause early depletion of the geothermal reservoir and a consequent termination of energy production. For this reason it is important to consider circulation rates which would ensure the longevity of a reservoir.

During the heat extraction simulations, we consider a production rate, which is equal to the injection rate (26 L/s). The condition of a constant circulation rate is implemented as boundary condition. The temperature of injected water is 80°C and is kept constant during the whole production time (Vogt et al., 2011). These represent typical values used in thermal energy production systems located in crystalline environments.

Table 6.9: *Position of the injection and production wells in the local coordinate system (see also Fig 6.18). Value of the circulation rate is being kept constant during the whole production time. Simulations provide an overview of the produced heat, if the temperature of injected water is 80°C.*

well	x [m]	y [m]	depth [m]	circulation rate [L/s]	water temperature [°C]
injection	1500	1500	4700	26	80
production	2250	1500	5700	26	calculated

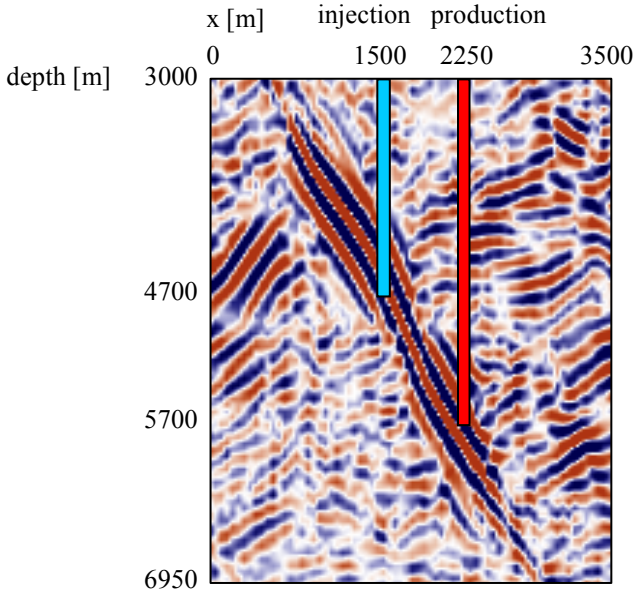

Fig. 6.18: *Location of the injection and production wells within the detailed model.*

For the calculations of the transient flow in a doublet system, definition of boundary conditions only is insufficient. The simulation software requires also initial values of the hydraulic head and the temperature at every gridpoint of the model. To obtain these values we first calculate a steady-state model of the small area with boundary conditions taken from the simulation results of the previously calculated large-scale model. The following Dirichlet thermal boundary conditions were applied: T_{top} = 94.82 °C, T_{base} = 202.0 °C. Lateral boundary conditions are set to no-flow thermally as well as hydraulically.

Steady-state calculations of the small model yield the initial values for simulations of a transient flow. No-flow hydraulic boundary conditions proved to be the most stable choice and agree also with the idea of a hydraulically fractured area. This area has limited dimensions (we assume them to be maximally the dimensions of the small model) and due to the low matrix permeabilities past the borders of this area, fluid flow here is not expected.

For the given site location and position of injection and production boreholes, we perform heat production simulations for the operation time of 80 years. While the resulting temperature–time profiles are self-explanatory, meaning of the other simulation product, the grid-cell pressure (p_b) needs some clarification. Pressure is one of the important factors affecting production efficiency. Insufficient pressure in the well would mean a termination of production, or the necessity to increase the amount of injected fluid. For this reason, throughout the whole simulations, simultaneous observation of temperature and well pressures (p_w) is necessary.

Clearly, dimensions of a grid-cell (50 m) with which the model is discretised are much larger than the well radius (usually 8 cm). In order to receive the value of pressure inside the well, the calculated grid-cell pressure needs to be corrected. To do this, we use the Peaceman (1983) approach

$$p_w = p_b - \frac{q_w \eta}{2\pi k \Delta z} \log\left(\frac{r_c}{r_w}\right). \tag{6.16}$$

Here

q_w	is the circulation rate
η	fluid dynamic viscosity
k	permeability
Δz	cell size in z-direction
r_w	radius of the well
r_c	radius of the cell defined for cube cells by their horizontal dimensions is

$$r_c = 0.14\sqrt{\Delta x \Delta y}\,. \tag{6.17}$$

The smaller dimensions of the doublet model allow to include more detailed structural information. We now consider also the matrix permeability anisotropy, as it was measured in the laboratory under simulated in situ conditions. Core samples recovered from the two KTB boreholes composed of gneisses and metabasites show a considerable amount of permeability anisotropy (Fig. 6.2). Permeability parallel to foliation showed to be one magnitude higher (mean value $2.7\text{x}10^{-19}$ m^2) than permeability perpendicular to foliation (mean value $2\text{x}10^{-20}$ m^2) (Huenges et al., 1997). No obvious depth dependence could be observed in the available data. These values describe the matrix permeability before hydraulic fracturing. According to results of fracture density calculations, the doublet installation is situated in a zone of increased crack occurrence. This means that after permeability stimulation, also values of matrix permeability will be slightly increased. During the simulation process we assume the lowest matrix permeability value to be 10^{-18} m^2.

Permeability of the system is the main parameter governing the whole simulation process. There are three main structures which define the model's permeability: rock matrix, the SE fault and the small-scale fractures. Rock matrix, as well as the zone of

the SE fault lithologically consists of the same rocks (gneisses and metabasites), therefore anisotropy is assumed for both. In the case of small-scale fractures due to the prevailing linear character, a preferred flow direction is given.

Since we are not able to predict the exact absolute permeability values of the system after hydraulic fracturing, we test different scenarios presented in the following five chapters. While existence of the large-scale SE faults is a fact, the small-scale fractures need to be treated with some caution. Although the results of several verification methods spoke for the plausibility of the fractures, their properties can be guessed only.

Thermal properties of the rocks are same as in the large-scale model and are listed in Table 6.8.

6.4.1 Doublet Model 1

Same as in the previously shown regional model, we start the simulations of heat extraction with a very simple model. The model presented in the Figure 6.20 is homogeneous in the sense of hydraulic rock properties. This model shall represent the unfractured crystalline rock. The existence of the large-scale fault zone is not being considered as well. Permeability (k_z) of the rock is 10^{-18} m^2 (Tab. 6.10) and as mentioned, it is homogenous and isotropic in the whole volume of the model.

Table 6.10: *Permeability values of the main structural features in the first model of a doublet system. The large-scale fault and small-scale fractures are not yet being taken into account.*

doublet model 1	*kx* [m^2]	*ky* [m^2]	*kz* [m^2]
matrix	10^{-18}	10^{-18}	10^{-18}

A two-well system simulation in such an environment yields the following results (Fig. 6.19 & Fig. 6.20). The constant circulation rate of 26 L/s between the injection and the production borehole yields unrealistic pressures caused by the impermeable crystalline rock. Absolute values of borehole pressures in Figure 6.19 do not have a deeper meaning since they are the result of conditions unsuitable for the functioning of a doublet system. Since there is no path leading towards the production well, water constantly injected into the system accumulates at the location of the injection well and causes the increase of injection well pressure. The maximal value allowed by the simulation software is reached practically immediately. On the other hand, the condition of constant 26 L/s water production yields very low pressures at the production well.

The temperature field behaves similarly. While temperatures in the surroundings of the injection well are increasing due to the constantly accumulating warm water, the heat at the production well is depleted completely within the simulated 80 years (Fig. 6.19).

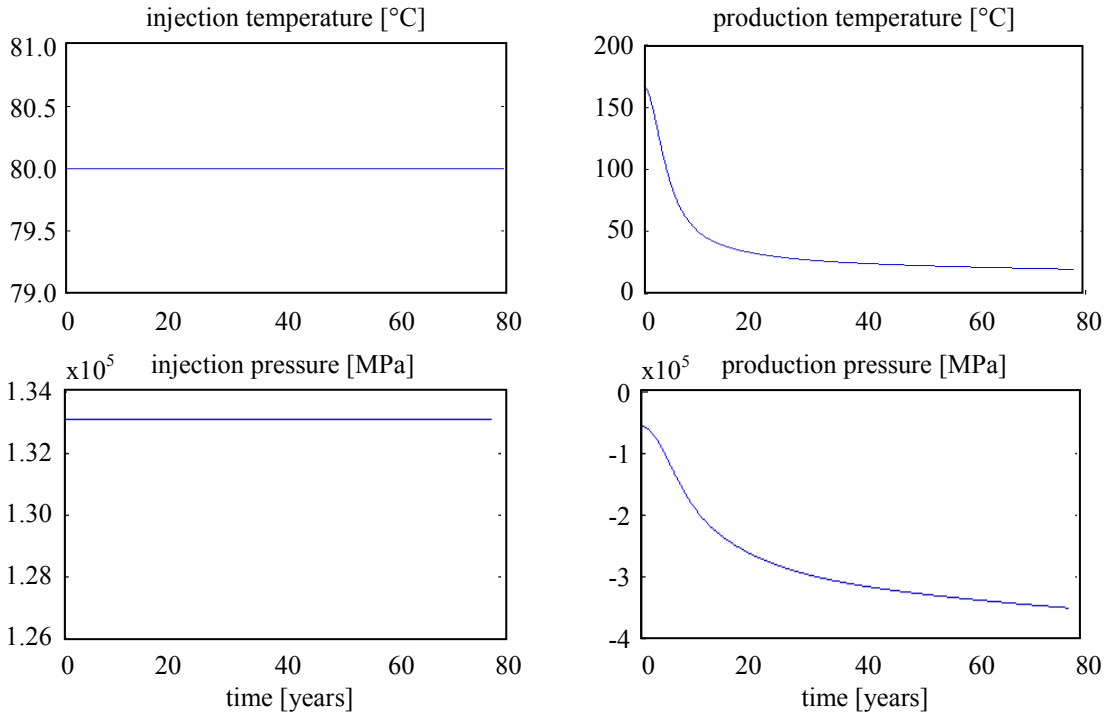

Fig. 6.19: *Modelled temperature-time and pressure-time profiles of injection and production wells for operation time 80 years and circulation rate 26 L/s. The corresponding hydraulic properties of the rock are listed in Table 6.10.*

Figure 6.20 shows the thermal field and the fluid flow at different stages of the simulations plotted on a vertical cross-section. Along with the temperatures (T), also reduced temperatures (T_{red}) are shown. After the subtraction of the linear increase of temperatures with increasing depth, the reduced temperatures calculated with the formula (6.15) show the smaller variations of the temperature field.

While viewing the fluid flow, it is necessary to remember that Darcy velocities (q) of the value 10^{-16} m/s (dark blue colour) are extremely low. One can almost say that areas which exhibit these Darcy velocities do not contribute to the fluid flow at all.

The location of the injection and production well is not specifically marked in the cross-sections. This was not necessary, since position of the injection and production points can be understood easily when observing the changes of temperatures and Darcy velocities. Additionally, an overview of the well's positions at the same cross-section is given in Figure 6.18.

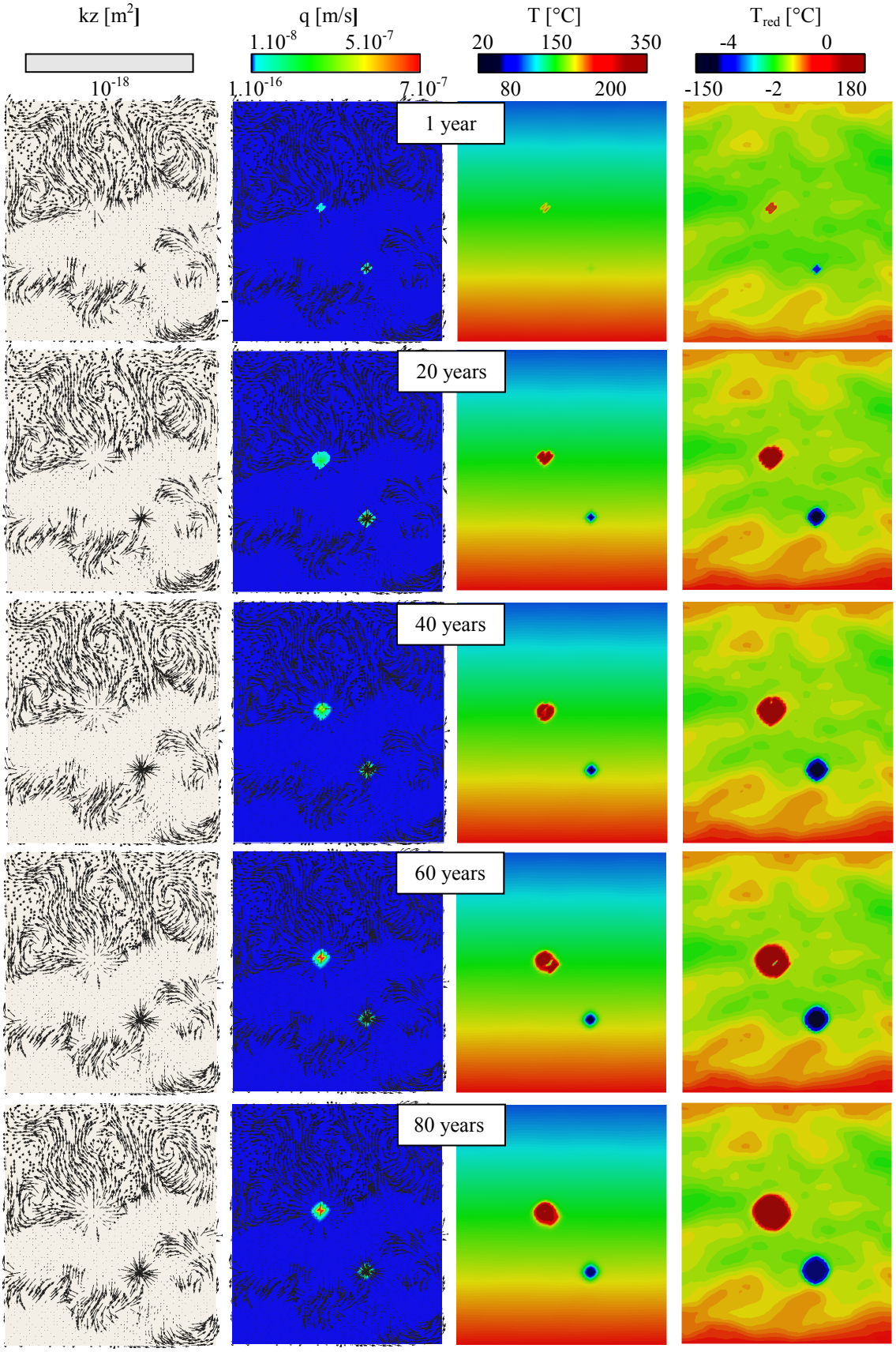

Fig. 6.20: *A cross-section through the heat extraction model 1. Shown is the effect of a doublet production system on chosen parameters in time.*

6.4.2 Doublet Model 2

With the aim to understand the hydraulic effect of the small-scale fractures, four different models are being tested. In the first simulated scenario, the presence of small-scale fractures is neglected and the effect of only the large-scale fault surrounded by a low permeability matrix is calculated (Tab. 6.11).

Table 6.11: *Permeability values of the main structural features in the second model of a doublet system. Small-scale fractures are not being taken into account.*

doublet model 2	*kx* [m^2]	*ky* [m^2]	*kz* [m^2]
SE fault	10^{-14}	10^{-13}	10^{-14}
matrix	10^{-18}	10^{-17}	10^{-18}

Simulation of 80 years of heat production in this kind of environment with a constant circulation rate (26 L/s) and constant temperature of injected water (80°C) yields temperate and pressure variations plotted in the Figure 6.21. Processes taking place in the model during the heat production are shown also in the Figure 6.22. Flow direction, Darcy velocity, reduced temperatures and the actual temperatures are plotted for chosen time intervals. As the Darcy velocities are showing, the overall fluid flow is happening inside the large-scale fault in the direction from the injection well towards the production well.

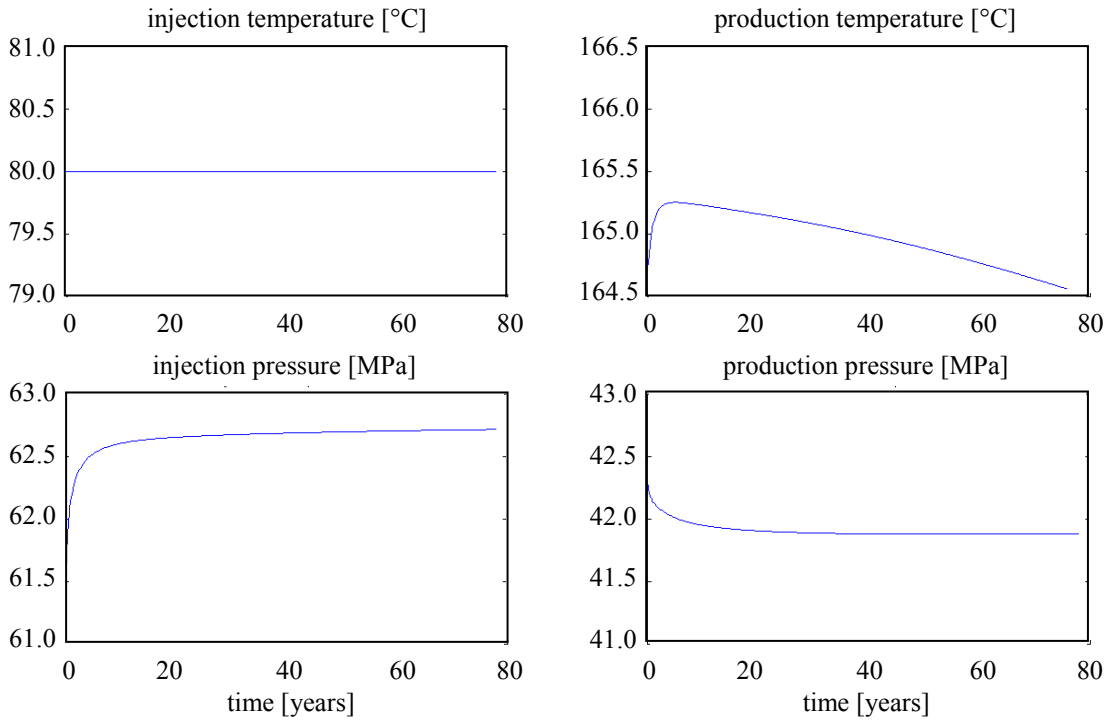

Fig. 6.21: *Modelled temperature-time and pressure-time profiles of injection and production boreholes for operation time 80 years. The corresponding model properties are listed in Table 6.10.*

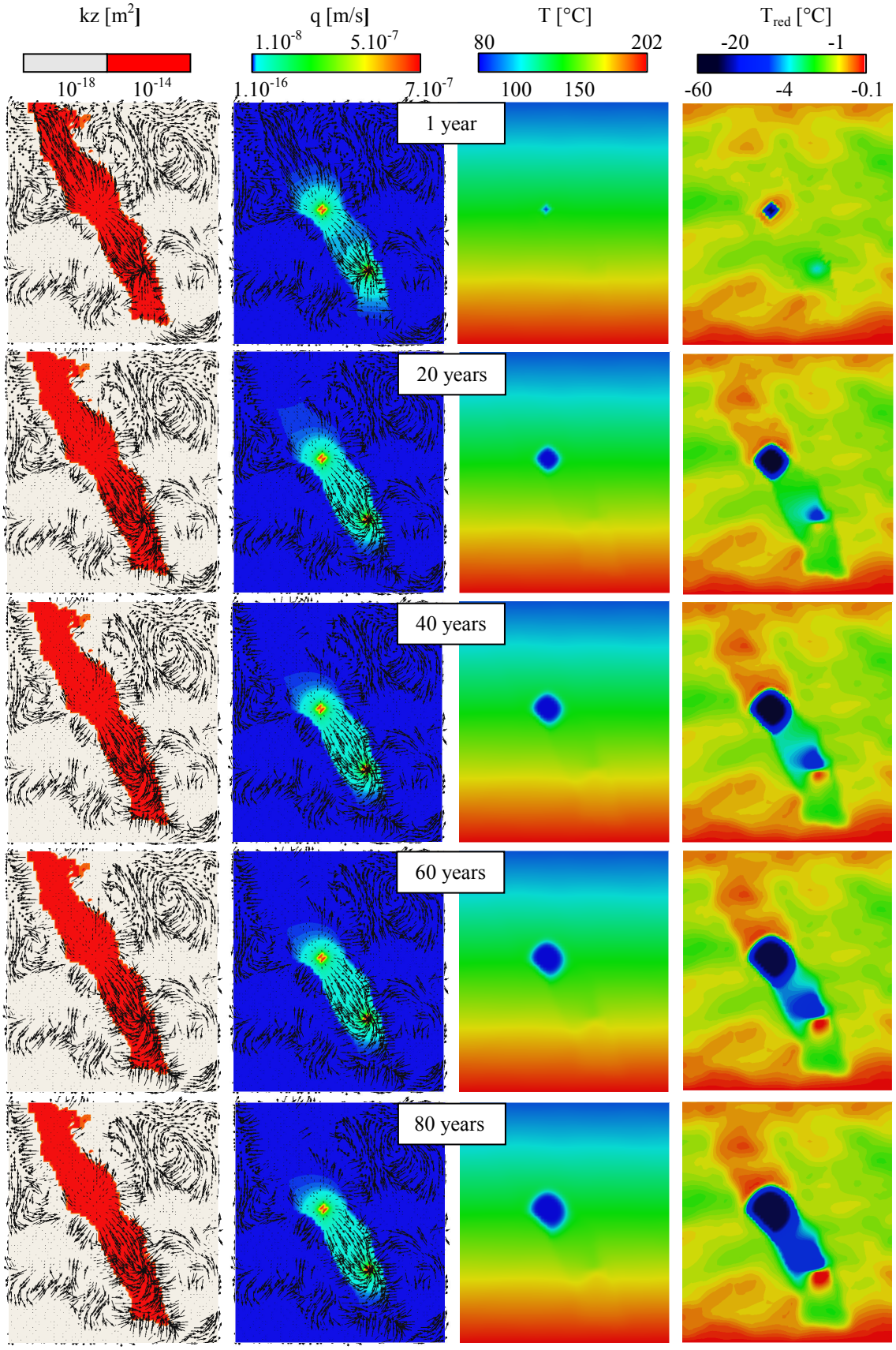

***Fig. 6.22**: A cross-section through the heat extraction model 2. Shown is the effect of a doublet production system on chosen parameters in time.*

6.4.3 Doublet Model 3

As the third scenario, we consider small-scale fractures as existent and their permeability values higher than of the matrix rock, but lower than the permeability of the large-scale fault zone (Tab. 6.12). While anisotropy is assumed for the SE fault and the matrix, permeability of small-scale fractures is assumed to be isotropic, or rather dominated by the linear character of the particular fracture.

Table 6.12: *Permeability values of the main structural features in the third doublet system model.*

doublet model 3	*kx* [m^2]	*ky* [m^2]	*kz* [m^2]
SE fault	10^{-14}	10^{-13}	10^{-14}
small-scale fractures	10^{-15}	10^{-15}	10^{-15}
matrix	10^{-18}	10^{-17}	10^{-18}

The resulting temperature and pressure variation at the location of the injection and production boreholes is presented in the Figure 6.23. Figure 6.24 shows the changes of thermal and hydraulic flow on a single cross-section. Even though the small-scale fractures are now part of the model, most of the flow is still concentrated into the large-scale fault zone.

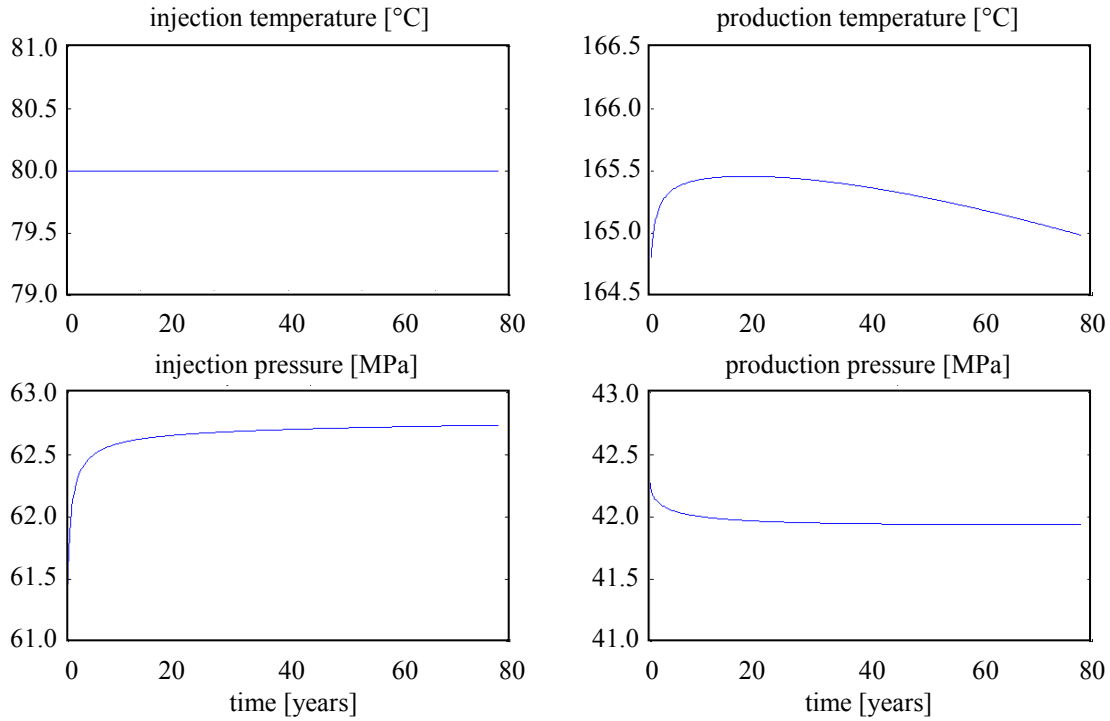

Fig. 6.23: *Modelled temperature-time and pressure-time profiles of injection and production boreholes for operation time 80 years. The corresponding model properties are listed in Table 6.12.*

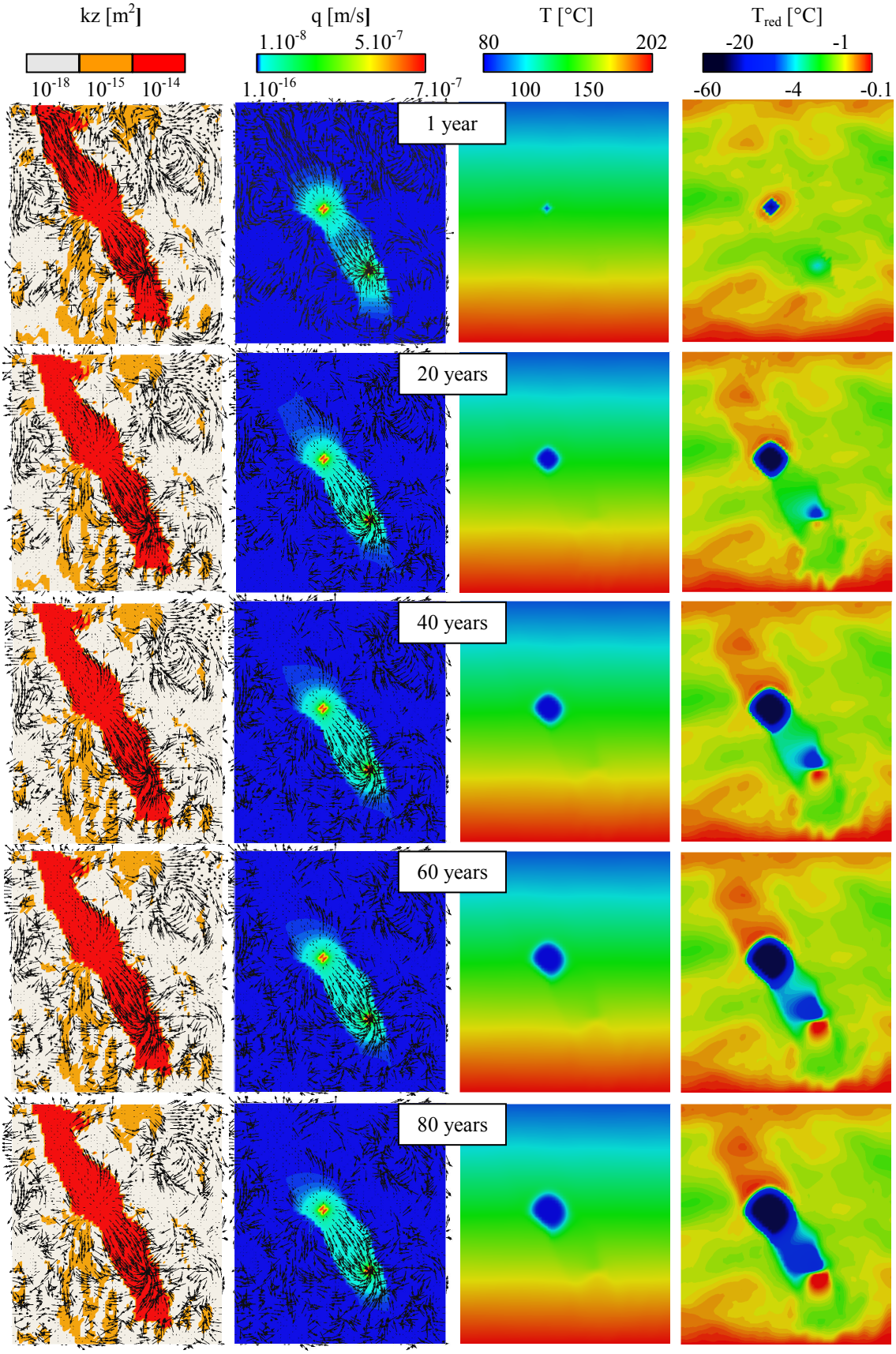

***Fig. 6.24**: A cross-section through the heat extraction model 3. Shown is the effect of a doublet production system on chosen parameters in time.*

6.4.4 Doublet Model 4

The case when small-scale fractures are of similar permeability as the large-scale fault is considered in the fourth model. Same as in the previous case, fractures did not receive any anisotropy (Tab. 6.13) since they clearly are of different nature than the matrix and the large-scale fault.

Table 6.13: *Permeability values of the main structural features in the fourth model of a two-well installation.*

doublet model 4	*kx* [m^2]	*ky* [m^2]	*kz* [m^2]
SE fault	10^{-14}	10^{-13}	10^{-14}
small-scale fractures	10^{-14}	10^{-14}	10^{-14}
matrix	10^{-18}	10^{-17}	10^{-18}

The resulting temperate and pressure variation recorded at the position of the injection and the production well is plotted in Figure 6.25. Changes of fluid and heat flow during the production time can be observed closely in Figure 6.26. The small-scale fractures have already a notable effect on the production and serve as paths of fluid flow. There is an indication of the origin of a convection cell in the lower section of the model. Fluids passing through the deep, hot rock collect a considerable amount of heat.

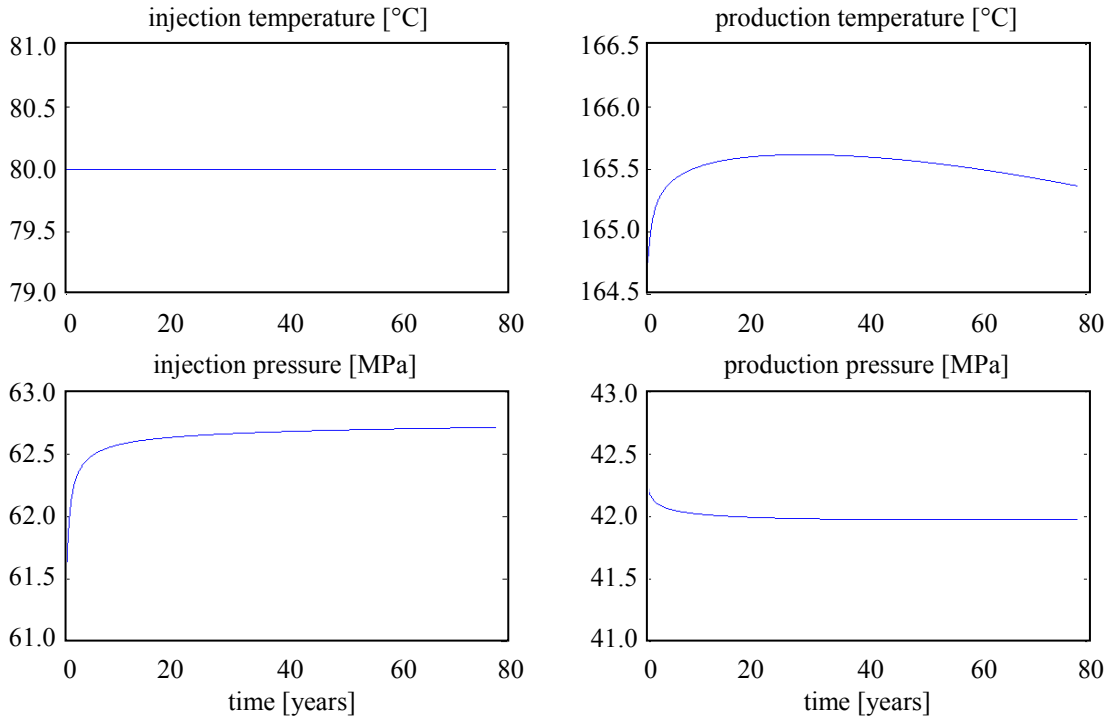

Fig. 6.25: *Modelled temperature-time and pressure-time profiles of injection and production boreholes for 80 years operation time. The corresponding model properties are listed in Table 6.13.*

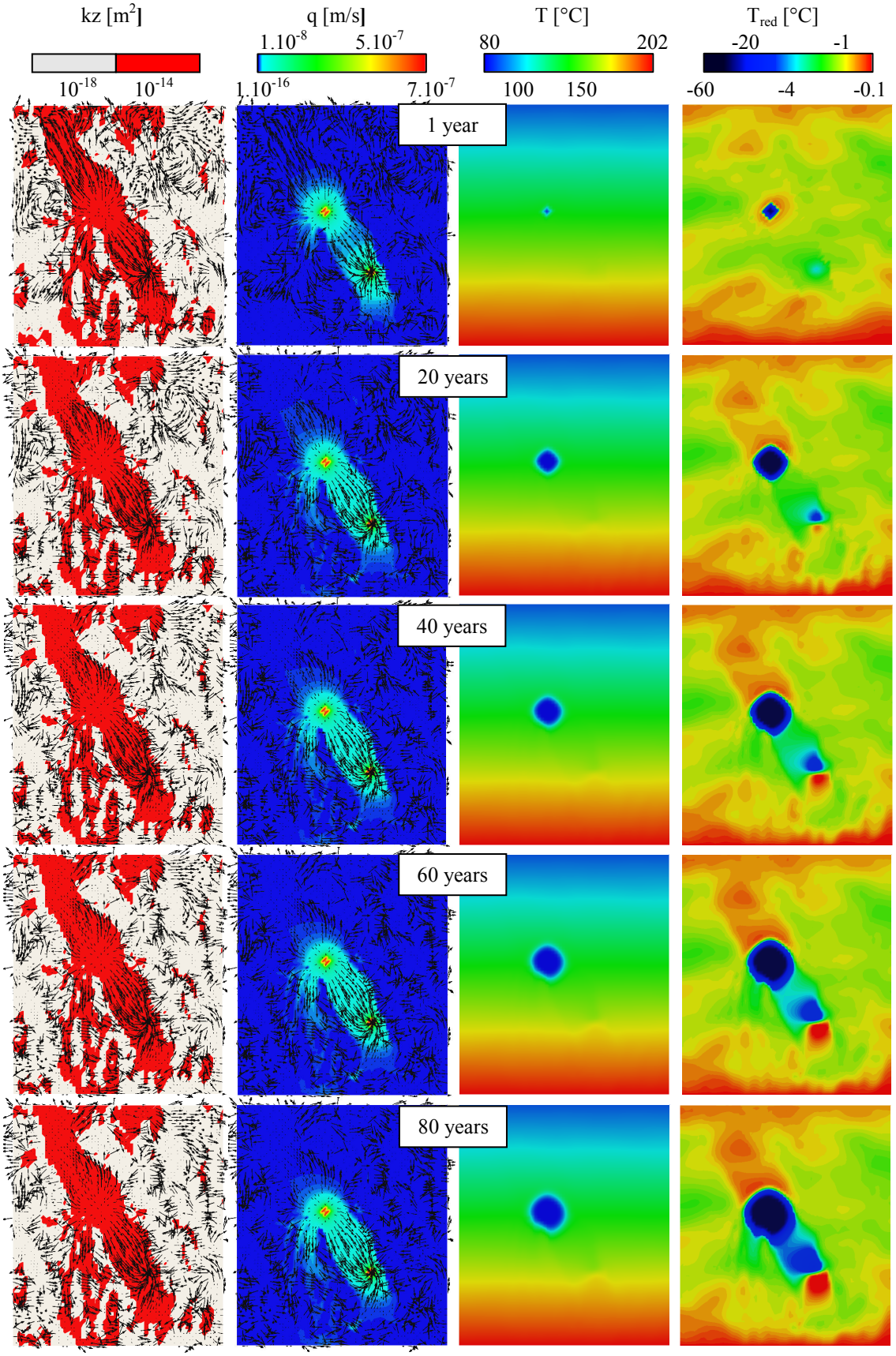

***Fig. 6.26**: A cross-section through the heat extraction model 4. Shown is the effect of a doublet production system on chosen parameters in time.*

6.4.5 Doublet Model 5

As the last scenario, small-scale fractures are assumed to be of permeabilities higher than the SE fault (Tab. 6.14). Water injected into the large-scale fault will therefore percolate preferably into the small-scale fractures. Due to the nature of the fractures and if we consider hydraulic fracturing applied within the large-scale fault zone, this case is less realistic. Nevertheless, for the sake of the completeness of the calculations, it has been considered as well.

Table 6.14: *Permeability values of the main structural features in the fifth model of a doublet system.*

doublet model 5	*kx* [m^2]	*ky* [m^2]	*kz* [m^2]
SE fault	10^{-14}	10^{-13}	10^{-14}
small-scale fractures	10^{-13}	10^{-13}	10^{-13}
matrix	10^{-18}	10^{-17}	10^{-18}

Temperate and pressure variations calculated for the injection and production boreholes are presented in Figure 6.27. While the pressure values do not differ notably from the previous results and are realistic, the development of produced temperatures as it was calculated is in reality not be possible. Figure 6.28 gives an explanation to why the simulation yielded these results. Shown is the change of fluid and heat flow with time plotted onto a cross-section. Since the small-scale fractures now have the highest permeability values, with time fluids are gradually redirected from the direct path between the injection and the production borehole into the paths provided by the fractures. A convection cell seems to originate in the system, leading the circulating fluid into the deeper sections of the model towards its borders.

Border conditions in this model are, same as in the previous models, set to no-flow. However, small-scale fractures which now represent the major hydraulically conductive structures are located also directly at the borders of the model. Ideally, the distance of the area of interest from the model borders should be large enough not to be affected by the border conditions (Flores et al., 2001). This is not fulfilled in the scenario presented by the doublet model 5. Unfortunately, opening borders for hydraulic flow did not result in an improvement of the simulation results either. This fact points out the complexity of hydrothermal processes taking place in an environment containing a number of fractures.

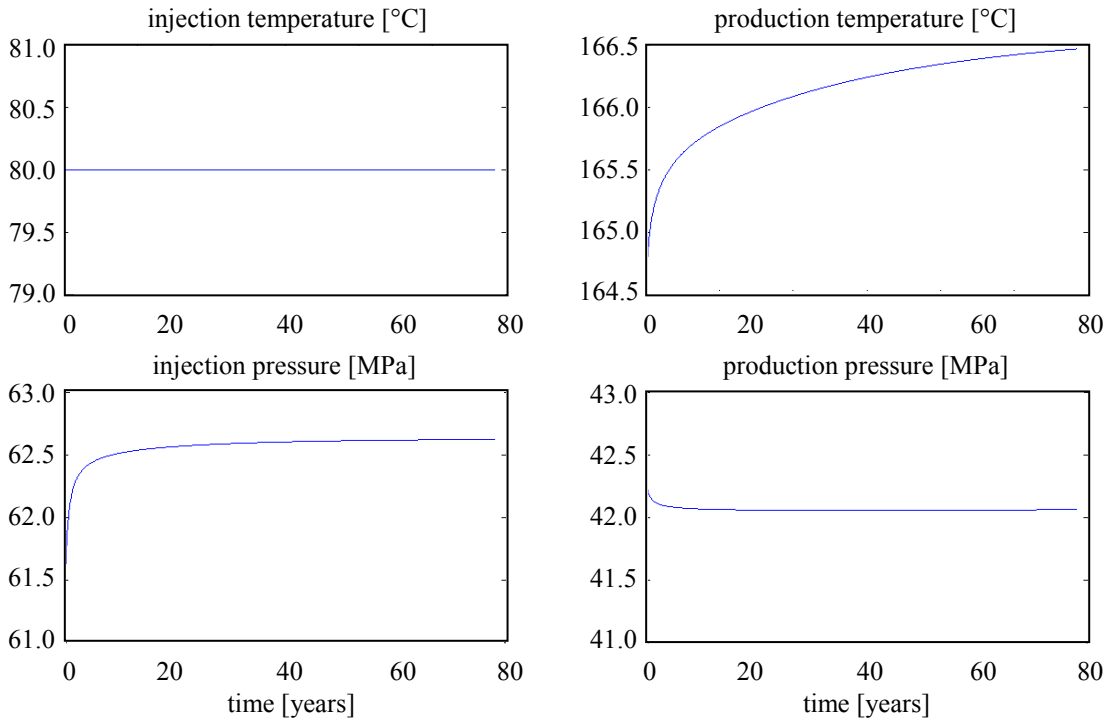

Fig. 6.27: *Modelled temperature-time and pressure-time profiles of injection and production boreholes for operation time 80 years. The corresponding model properties are listed in Table 6.14.*

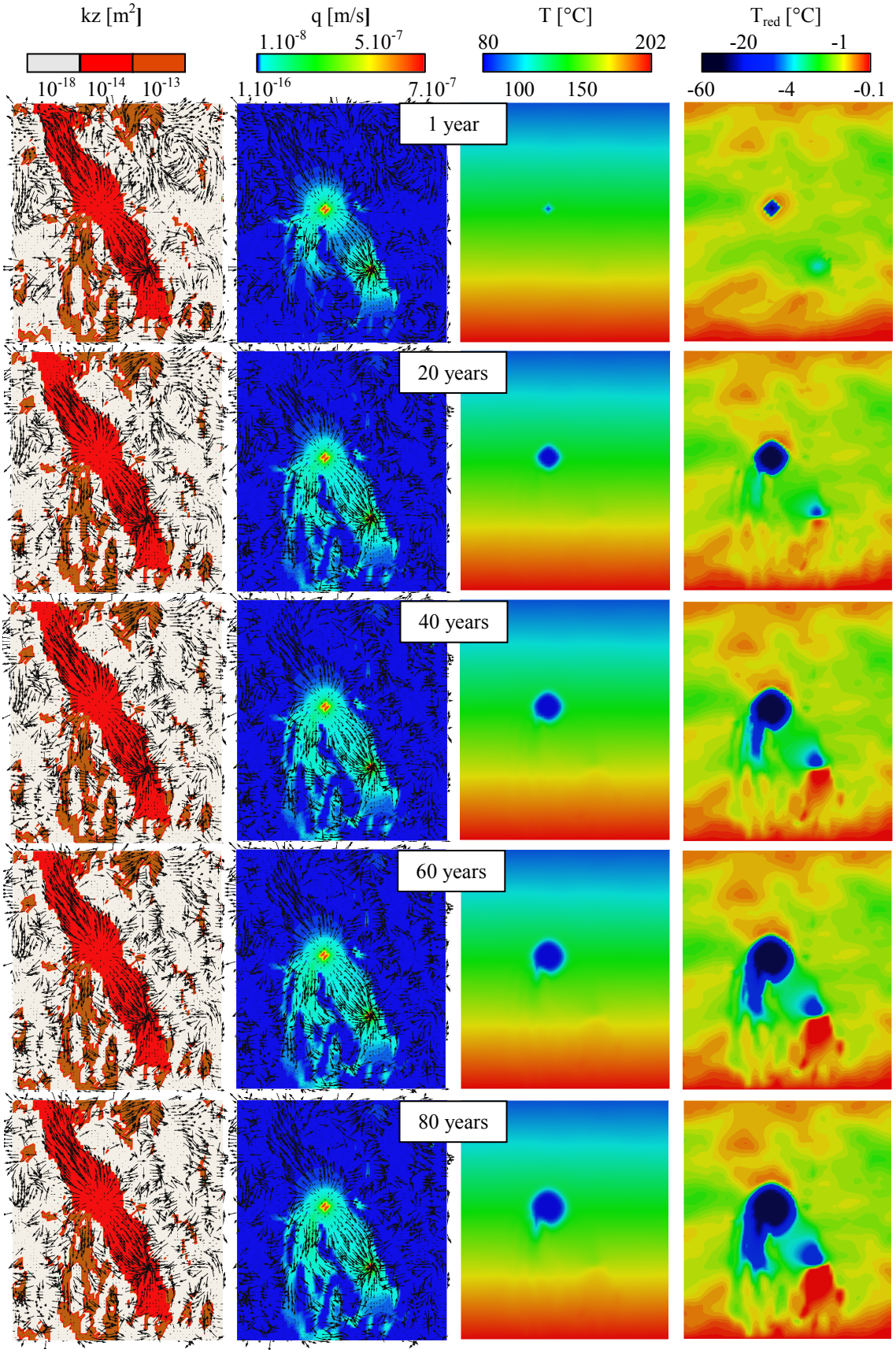

Fig. 6.28: *A cross-section through the heat extraction model 5. Shown is the effect of a doublet production system on chosen parameters in time.*

6.5 Summary

Simulations of the thermal and hydraulic field of the KTB site in a large-scale (regional) model yielded information necessary for the construction of a smaller, more detailed model of the actual heat production. Due to low permeabilities of the crystalline matrix rock, additional permeability stimulation with hydraulic fracturing is required. During this procedure water injected under high pressure causes pressure build up, which acts on fractures and reopens them and creates thus pathways for fluid circulation. Te fact that absolute permeability values of such an enhanced system are difficult to predict led to the consideration and modelling of several different scenarios.

Location of the doublet installation has been chosen so that the large-scale fault SE1, which is expected to be the structure of highest hydraulic conductivity, would stand in the centre. Apart from the SE1 fault, the model incorporates middle-scale fractures and the matrix rock consisting of alternating gneisses and metabasites of the Zone of Erbendorf-Vohenstrauß. These three structures control the permeability composition of the model. From the numerous different cases of permeability ratios which have been considered and simulated, we present the main five. While, thanks to laboratory data permeability of the matrix and the SE1 fault can be estimated, different absolute permeability values assigned to middle-scale fractures are being tested.

Both, injection and production boreholes of the doublet system are placed directly into the large-scale fault, where rather increased permeabilities are expected. Water of the constant temperature 80°C is being injected into the system and travels downwards to the production well, from which it is pumped to the surface. The rate of circulating water is kept constant at 26 L/s, while pressure and temperature change with time are being observed.

The first model represents a simple homogenous crystalline matrix of low permeability in which the presence of faults or fractures is not being considered. For each of the models, temperature-time and well-pressure-time graphs are presented as well as cross-sections through the model. Plotted are the Darcy velocities, temperatures and reduced temperatures of the models after 1, 20, 40, 60 and 80 years of production.

The following two scenarios, in which permeability of the middle-scale fractures is considered to be lower than of the large-scale fault, are most realistic and give also the best simulation results. Within the operation time of 80 years with the circulation rate 26 L/s, temperature of the geothermal reservoir dropped by maximally 1°C. Pressure at the producer well is about 20 MPa lower than at the injector and stays almost constant during the production time.

Models 4 and 5, in which the fracture permeability is reaching high values, bring difficulties into the calculations of fluid flow. Especially for the last scenario, in which the fractures are of highest permeabilities, the calculated results can not be considered as true. With time constantly increasing produced temperature is not realistic, but is the result of boundary effects. While it is clear that in the case of highly permeable fractures located also at the boundaries of the model no-flow boundary conditions do not apply, opening boundaries hydraulically also did not improve the simulation results. This fact is a common problem in hydrothermal modelling and is caused by the extreme complexity of the processes taking place in a model containing a large number of fractures. Presently, the used simulation software is not able to calculate these kinds of

models.

However, probably the most realistic case is represented by the model number 3 (Chapter 6.4.3), in which permeability of middle-scale fractures is lower than the permeability of the SE1 fault, but higher than of the matrix. Temperature-time and well-pressure-time variations for the doublet model 3 are presented in the Figure 6.29 one more time. After 80 years of production, the temperature in the production well dropped by only 1 °C. Flow field calculated for this model shows that the main path followed by water particles is between the injection and production well inside of the SE1 fault. Hydraulic flow occurs also within the other structures of the model, but with a velocity too low to affect production temperatures and the pressure (Fig. 6.30). The reduced temperatures plotted in Figure 6.30 were calculated using the formula (6.15) and show the area most affected by the doublet installation.

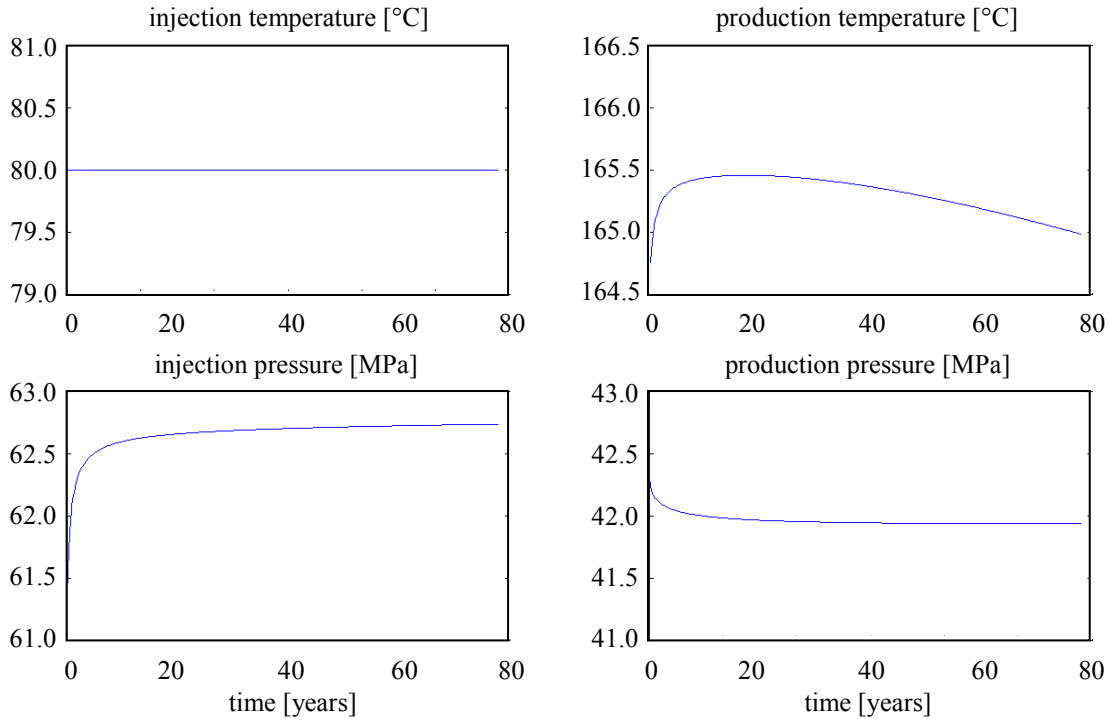

Fig. 6.29: *Modelled temperature-time and pressure-time profiles of the injection and production well in the case of the doublet model 3 (Chapter 6.4.3). 80 years of heat production with the constant circulation rate 26 L/s were simulated.*

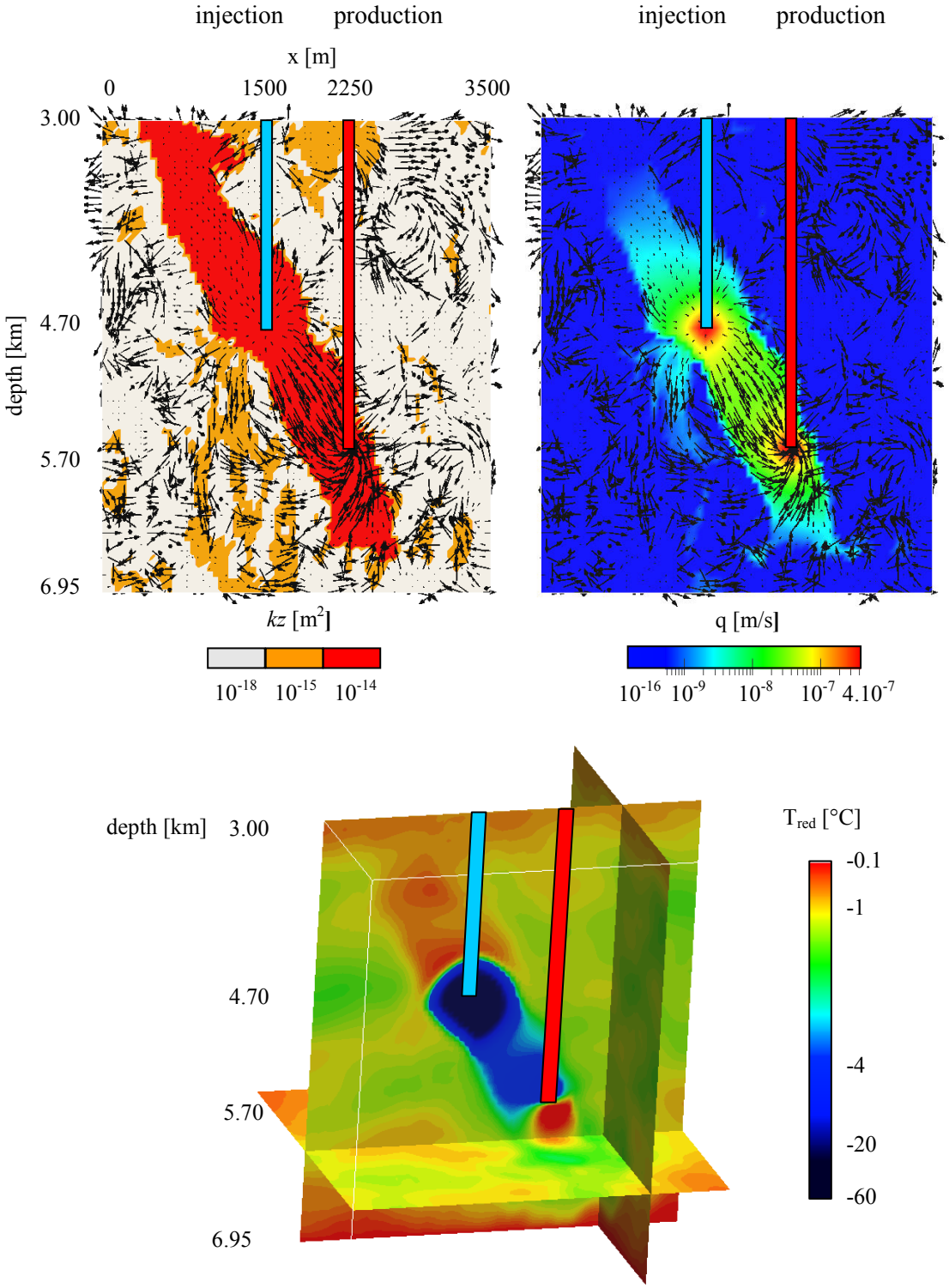

Fig. 6.30: *Vertical cross-section through the third model of a doublet installation, in which middle-scale fractures are of lower permeability than the SE1 fault. Upper left: colour code represents the permeability; arrows show the direction of hydraulic flow. Upper right: colour code represents the Darcy velocity; arrows show the direction of hydraulic flow. Lower figure shows the calculated temperature field in the form of reduced temperatures in 3-D.*

Chapter 7

Conclusions & Discussion

Short paragraphs summing up the acquired information can be found at the end of every chapter. The following shall offer a general summary of the whole work and point out the connections between the separate steps one more time.

A wide amount of information concerning the Continental Deep Drillhole (KTB) site has been processed and evaluated with the aim to assess its suitability for geothermal exploitation. The mentioned site has been chosen representative for geothermal reservoirs located in crystalline environments mainly because of the large amount of freely accessible high quality data, high temperature values measured and the favourable tectonic features. The work concept set up during the evaluation of KTB data can be followed also during geohydrothermal assessments of similar crystalline sites.

The main sources of information processed and analysed within the scope of this work were the three-dimensional reflection seismic data recorded during the ISO89 campaign together with downhole measurement from the superdeep KTB borehole.

Lithological interpretation of seismic cross-sections regularised with a priori data (geological map, geological cross-section through the KTB site, etc.) led to the classification of the whole area into six main lithological units. Since the section relevant for geothermal exploitation is located in the centre of the survey area, within the Zone of Erbendorf-Vohenstrauß (ZEV), this lithological unit has been treated in much more detail. Identification of the remaining units on a coarse scale proved to be sufficient.

The KTB borehole located directly within the ZEV provides continuous records of the penetrated section up to depths of about 9000 m. Analyses of log data showed that the main rock components of this crystalline unit are gneisses and metabasites. The fact that thermal properties of these two rock units differ considerably had to be taken into account during the coupled hydrothermal simulations. Therefore, in order to identify the complex lithological structure of the ZEV, computations of synthetic seismograms have been performed. A “bank” of 20 000 lithological models of alternating gneisses and metabasites created with the Monte Carlo method has been used for the calculation of synthetic traces. Those traces correlating best with the real seismic traces were selected for the construction of a 3-D synthetic data cube. The corresponding parenting lithological models then represent local gneiss-metabasit ratios and can be put into connection with the thermal rock properties.

Geothermal relevance of a reservoir is conditioned not only by favourable thermal properties of the rocks, but also by hydraulic characteristics of the environment. The crystalline matrix of the KTB site is defined by low permeability values which result in very low fluid flow. On the other hand, the high amount of cracks often found in the crystalline rock can affect the flow field in a positive way. Knowledge concerning the fracture network of a site is therefore vital for successful geohydrothermal simulations.

The main tectonic feature of the KTB site is the Franconian Lineament, a deep reaching, steep bundle of faults intersecting the survey area in the NW-SE direction. In the interpreted seismic data, this large-scale fault system can be identified by its characteristic angle of inclination. Dip calculations and *k-k* analyses were therefore very successful in the identification process of the fault's extent and position.

The attempt to explain shifts of horizons visible in the seismic data led to the conclusion that these structures might represent a middle-scale fracture network in the crystalline rock. Characterised by amplitudes close to zero, the structures could be identified and extracted from the dataset with the help of log-Gabor filtering and additional image processing. Plausibility of the detected fractures has been verified in various ways, including visual analysis, fractal dimension analysis and the comparison to former results based on induced microseismicity.

In order to function as paths for fluid flow, fractures have to be of higher permeability than the surrounding rock. Seismic data do not distinguish between healed and hydraulically open fractures, but they can provide information concerning the spatial orientation of each fracture. Relating this information to the present-day stress field enabled the selection of only fractures critically stressed and thus most probably permeable.

The mere existence of a fracture, even it is hydraulically open does not suffice to enable fluid circulation. Only fractures connected into paths can contribute to the flow field. Fracture density can be related to fracture connectivity, in other words, with higher fracture density also the probability of a continuous path is increasing. Fracture connectivity calculations based on the percolation theory lead to the designation of zones of different levels of fracture permeability. While the network including fractures of all orientations seems to be highly interconnected, consideration of only the critically stressed fractures yields permeable zones of minimal extent.

The above mentioned finding is supported by the results of coupled hydrothermal simulations. A three-dimensional model of the whole area discretised on an equidistant broad (300 m) network of gridpoints has been used for calculations of the site's thermal and hydraulic conditions. While seismic cross-sections carry the information concerning the different zones of relative values of petrophysical characteristics (thermal conductivity, heat production, permeability, porosity), literature sources and log data had to be consulted in order to acquire the absolute values.

The simulation process begun with a model of the simplest characteristics and throughout the modelling lithological complexity has been stepwise increased in order to show the least amount of information necessary for solving of the temperature field. At the coordinates of the KTB borehole, a temperature-depth profile is being extracted and compared with the latest temperature log recorded in the KTB-HB borehole. Simulations show that the temperature field is reproduced correctly already at a relatively early stage of the modelling, at the consideration of the three following main lithological units: foreland sediments, granitic outcrops and the large homogeneous Zone of Erbendorf-Vohenstrauß. Except for the sedimentary unit, porosity as well as permeability of the model has to be low to yield correct temperatures, which results in Darcy velocities of maximally 10^{-12} m/s. Flow field of such low velocity implies that heat exchange at the KTB site is dominated by convection.

Heat production calculations are performed on a smaller and more detailed subsection of the dataset. Simulations of the large-scale model provided not only boundary conditions for the doublet systems, they also suggest that additional enhancement of the site's permeability is necessary. Therefore, permeability values used during the simulations of a two-well geothermal installation are those assumed for a system after hydraulic fracturing.

Since the SE1 fault zone represents the tectonic feature best suitable for fluid conduction, both injection and production borehole were placed directly within. The fluid injected into the system is circulating in the depth interval of about 4000 m to 6000 m. Simulations covering five different possible scenarios were performed. The most realistic one is assuming a matrix rock of low permeability and a permeable large-scale fault zone. The middle-scale fractures are considered as well and receive a permeability value which is higher than the permeability of the matrix and lower than the permeability of the fault zone. If the temperature 80°C of injection fluid and 26 L/s circulation rate are assumed in such environment, drop of the produced temperature will not exceed 1°C within 80 years of operation time. Similar values have been calculated for reservoirs located in other crystalline environments, such as in The Hague (Netherlands), or Soultz-sous-Forêts (France). Therefore, it can be stated that under the assumed conditions and the suggested parameters of the doublet geothermal system, the site of the Continental Deep Drillhole is suitable for geothermal energy production.

The high quality three-dimensional seismic data were the key dataset during the assessment of the site's geothermal potential. Structural models of three different grid-cell sizes (50 m, 150 m and 300 m) have been constructed in order to test the ratio of computing time vs. obtained information. Already the broadest grid size proved to provide enough information necessary to explain the prevailing geohydrothermal conditions. It can thus be assumed that a network of 2-D seismic profiles could offer a similar amount of information with less effort spent for the survey and processing as well as a smaller financial budget than which is necessary for acquiring of a 3-D dataset. More attention concerning the structural information is required within the area selected for heat production. Here, especially procedures aiming on fracture network identification would be of high benefit.

Bibliography

ADMASU, F. & TÖNNIES, K., 2005. Anisotropic 3d Seismic Features for Robust Horizons Correlation across Faults. In *IEEE International Conference on Image Processing ICIP2005*, volume **2**, pages 225–228, 11.-14.

ADMASU, F., 2008. A Stochastic Method for Automated Matching of Horizons across a Fault in 3D Seismic Data. Dissertation, Otto-von-Guericke-Universität Magdeburg.

ALLABY, A. & ALLABY M., 1999. "hydraulic head." A Dictionary of Earth Sciences. *Encyclopedia.com.* http://www.encyclopedia.com/doc/1O13-hydraulichead.html

AUSTIN D., 2009. Percolation: Slipping through the cracks. American mathematical society. http://www.ams.org/featurecolumn/archive/percolation.html

AXELSSON, G., GUDMUNDSSON, A., STEINGRIMSSON, B., PALMASON, G., ARMANSSON, H., TULINIUS, H., FLOVENZ, O., BJÖRNSSON, S. & STEFANSSON, V., 2001. Sustainable Production of Geothermal Energy: Suggested Definition. IGA-News, *Quarterly* No. **43**, p. 1-2.

BAISCH, S., BOHNHOFF, M., CERANNA, L., TU, Y. & HARJES, H.-P., 2002. Probing the crust to 9 km depth: Unique fluid injection experiments and induced seismicity at the KTB Superdeep borehole, Germany. *Bull. Seismol. Soc. Amer*. **92**, 2369-2390.

BARTON, C.A., ZOBACK, M.D. & MOOS, D., 1995. Fluid flow along potentially active faults in crystalline rock, *Geology,* **23** (8), 683-686.

BEAR, J., 1972. Dynamics of Fluids in Porous Media, American Elsevier Publishing Co., New York, 761 p.

BERCKHEMER, H., RAUEN, A., WINTER, H., KERN, H., KONTNY, A., LIENERT, M., NOVER, G., POHL, J., POPP, T., SCHULT, A., ZINKE, J. & SOFFEL, H.C., 1997. Petrophysical properties of the 9-km-deep crustal section at KTB. *Journal of Geophysical Research*, **102**(B8), 18,337–18,361.

BOHNHOFF, M., BAISCH, S. & HARJES, H.-P., 2004. Fault mechanisms of induced seismicity at the superdeep German Continental Deep Drilling Program (KTB) borehole and their relation to fault structure and stress field, *Journal of Geophysical Research*, **109**, B02309.

BRACE, W.F., 1980. Permeability of crystalline and argillaceous rocks, *Int. J. Rock Mech. Min. Sci*., **17**, 241-251.

BRAM, K. & DRAXLER, J.K. (Eds.), 1992. Grundlagenforschung und Bohrloch-geophysik: Bohrlochmessungen in der KTB-Oberpfalz HB, Intervall 1720.0 - 4512.0 m, KTB Rep. 92-1, Niedersächsisches Landesamt für Bodenforsch., Hannover, Germany.

BRAM, K. & DRAXLER, J.K. (Eds.), 1993. Basic research and borehole geophysics: borehole logging in the KTB-Oberpfalz HB, interval 4512.0 - 6018.0 m, KTB Rep. 93-1, Niedersächsisches Landesamt für Bodenforsch., Hannover, Germany.

BRAM, K., & DRAXLER J.K., (Eds.) 1994. Basic research and borehole geophysics (final report): borehole logging in the KTB-Oberpfalz HB, interval 6013.5 - 9101.0 m., KTB Rep. 94-1, Niedersächsisches Landesamt für Bodenforsch., Hannover, Germany.

BRAM, K., DRAXLER, J.K., & ZOTH, G. (Eds.), 1991. Grundlagenforschung und Bohrloch-geophysik: Bohrlochmessungen in der KTB-Oberpfalz HB, Intervail 0-1720.0 m, KTB Rep. 91-2, Niedersächsisches Landesamt für Bodenforsch., Hannover, Germany.

BRUDY, M., ZOBACK, M. D., FUCHS, K., RUMMEL, F. & BAUMGARTNER, J., 1997. Estimation of the complete stress tensor to 8 km depth in the KTB scientific drill holes: Implications for crustal strength, *J. Geophys Res*., **102** (B8), 18453 - l8475.

BÜCKER, CH., HUENGES, E., LIPPMANN, E., RAUEN, A., STREIT, K.-M., WIENAND, J. & SOFFEL, H.C., 1990. KTB Pilot Hole. Results obtained in the KTB Field-Laboratory. D. Geophysics, KTB Report, 90-8 (D1-D29), ISSN 0939-8732, Hannover.

BURKHARDT, H., HAACK, U., HAHN, A., HONARMAND, H., JÄGER, K., STIEFEL, A., WÄGERLE, P. & WILHELM, H., 1989. Geothermal Investigations in the KTB Locations Oberpfalz and Schwarzwald, in The German Continental Deep Drilling Program (KTB), edited by Emmermann, R., and Wohlenberg, J., pp. 433-480, Springer-Verlag, New York.

BYERLEE, J., 1978. Friction of rocks, *Pageoph*, **116**, 615-626.

CASTEN, U., GÖTZE, H.-J., PLAUMANN, S. & SOFFEL, H.C., 1997. Gravity anomalies in the KTB area and their structural interpretation with special regard to the granites of the northern Oberpfalz (Germany). *Geol Rundsch* **86**, Suppl.: S79-S86, Springer-Verlag.

CLAUSER, C., GIESE, P., HUENGES, E., KOHL, T., LEHMANN, H., RYBACH, L., SAFANDA, J., WILHELM, H., WINDLOFF, K. & ZOTH, G., 1997. The thermal regime of the crystalline crust: Implication from the KTB. *Journal of geophysical research*, vol. **102**, NO.B8, pages 18,417-18,441.

CLAUSER, C. (ED), BARTELS, J., CHENG, L.Z, CHIANG, W.-H., HURTER, S.J., KÜHN, M., MEYN, V., PAPE, H., PRIBNOW, D.F.C., RANALLI, G., SCHNEIDER, W. & STÖFEN, H., 2003. Numerical Simulation of Reactive Flow in hot Aquifers using SHEMAT/Processing Shemat. Springer Verlag, Heidelberg-Berlin. 331 p.

COOK, J., CHANDRAN, V. & FOOKES, C., 2006. 3D face recognition using log-Gabor templates: presented at the British Machine Vision Conference (BMVC), September 4-7, 2006, Edinburgh.

DARCY, H., 1856. Les fontaines publiques de la ville de Dijon; Victor Dalmont, Paris.

DEKORP Research Group: Results of the DEKORP 4/KTB Oberpfalz deep seismic reflection investigations. *J. Geophys.*, **62,** pp. 69-101, 1988.

DEY, T.K. & GOSWAMI, S., 2003. Tight Cocone: A water tight surface reconstructor. Proc. 8th ACM Sympos. Solid Modeling Appl. 127-134.

DRAXLER, J.K. (Ed.), 1990. Grundlagenforschung und Bohrlochgeophysik: Bohrloch-messunegen in der KTB-Oberpfalz VB, KTB Rep. 90-1, Niedersächsisches Landesamt für Bodenforsch., Hannover, Germany.

DÜRBAUM, H.-J., REICHERT, C. & BRAM, K., 1990. Integrated seismics Oberpfalz 1989: Longterm logging and testing programme of the KTB-Oberpfalz VB. KTB-Report (DEKORP Report), vol. 90-6b. Hannover, Germany: Niedersachsisches Landesamt für Bodenforschung.

DÜRBAUM, H.-J., REICHERT, CH., SADOWIAK, P. & BRAM, K. (Eds)., 1992. Integrated Seismics Oberpfalz 1989. Data evaluation and interpretation as of October 1992. KTB-Report (DEKORP Report), vol. 92-5. Hannover, Germany: Niedersachsisches Landesamt für Bodenforschung.

EMMERMANN, R., ALTHAUS, E., GIESE, P. & STOECKERT, B. (Eds)., 1995. KTB Hauptbohrung: Result of Geoscientific investigation in the KTB Field Laboratory; Final report: 0-9101m. KTB-Report, vol. 95-2. Hannover, Germany: Niedersächsisches Landesamt für Bodenforschung.

EMMERMANN, R. & LAUTERJUNG, J., 1997. The German Continental Deep Drilling Program KTB: Overview and major results. *Journal of geophysical research,* vol. **102**, no. B8, pages 18,179 - 18,201.

EMMERMANN, R. & WOHLENBERG, J. (ed.), 1989. The German Continental Deep Drilling Program (KTB): 37-54, Springer-Verlag, Berlin.

FEHLER, M., HOUSE, L. & KAIEDA, H., 1987. Determining Planes Along Which Earthquakes Occur: Method and Application to Earthquakes Accompanying Hydraulic Fracturing*, J. Geophys. Res*., **92**(B9), 9407-9414.

FIELD, D., 1987. Relations between the statistics of natural images and the response properties of cortical cells, Journal of Optical Society of America, vol. 4, no. 12, pp. 2379–2394.

FLORES, E. L., PROL-LEDESMA, R.M. & ROYER, J.J., 2001: Boundary conditions in thermal models: An application to the KTB site, Germany. *Geofisica International,* Vol., **40**, Num. 2 pp. 97-109.

FLORY, P. J., 1941. Thermodynamics of High Polymer Solutions. *Journal of Chemical Physics* **9**, Issue 8, p. 660.

GEBRANDE, H., BOPP, M., MEICHELBOCK, M. & NEURIEDER, P., 1991. 3-D wide-angle investigations in the KTB surroundings as part of the "Integrated Seismics Oberpfalz 1989," in Continental Lithosphere: Deep Seismic Reflections Geodyn. Ser., vol. 22, edited by R. Meissner et al., pp. 147-169, AGU, Washington, D.C.

GRIGORESCU, S.E., PETKOV, N. & KRUIZINGA, P., 2002. Comparison of texture features based on Gabor filters, *IEEE Trans. on Image Processing*, **11** (10), 1160-1167.

HARJES, H.-P., BRAM, K., DÜRBAUM, H.-J., GEBRANDE, H., HIRSCHMANN, G., JANIK, M., KLÖCKNER, M., LÜSCHEN, E., RABBEL, W., SIMON, M., THOMAS, R., TORMANN, J. & WENZEL, F., 1997. Origin and nature of crustal reflections: Results from integrated seismic measurements at the KTB superdeep drilling site, *Journal of Geophysical Research*, **102**, 18,267- 18,288.

HEALY, J.H., RUBEY, W.W., GRIGGS, D.T. & RALEIGH, C.B., 1968. The Denver earthquakes, *Science*, **191**, 1301 – 1310.

HICKMAN, S., BARTON, C.B., ZOBACK, M.D., MORIN, R., SASS, J. & BENOIT, R., 1997. In-situ stress and fracture permeability in a fault-hosted geothermal reservoir at Dixie Valley, Nevada*, Geoth. Res. Coun. Trans*., **21**, 18l-189.

HIRSCHMANN, G., 1996. Ergebnisse und Probleme des strukturellen Baues im Bereich der KTB-Lokation. *Geologica Bavarica*, **101**, 37–51.

HIRSCHMANN, G., LICH, S. & WALL, H., 1994. KTB Oberpfalz - einige Ergebnisse der geowissenschaftlichen Bearbeitung. *Zbl Geol Paläont.* Teil **I** 7 (8): 861-873.

HOLM, A., BLODGETT, L., JENNEJOHN, D. & GAWELL, K., 2010. Geothermal Energy: International Market Update. Geothermal Energy Association.

HUENGES, E., BURKHARDT, H. & ERBAS, K., 1990. Thermal conductivity profile of the KTB borehole. *Sci. Drilling* **1**,224-230.

HUENGES, E., ERZINGER, J., KÜCK, J., ENGESER, B. & KESSELS, W., 1997. The permeable crust: Geohydraulic properties down to 9101 m depth, *J. Geophys. Res.,* **102**(B8), 18255 - l8265.

HUENGES, E. & ZOTH, G., 1991. KTB-Oberpfalz VB: temperature, thermal conductivity and heat flow density. Scientific Drilling, 2, pp. 81–89.

ITO, T. & ZOBACK, M.D., 2000. Fracture permeability and in situ stress to 7 km depth in the KTB Scientific Drillhole. *Geophysical Research Letters*, vol. **27**, no.7, 1045-1048.

JAHNE, B. & HAUBECKER, H., 2000. Computer vision and Applications: Academic Press, Inc.

JOBMANN, M. & CLAUSER, C., 1994. Heat advection versus conduction at the KTB: possible reasons for vertical variations in heat-flow density. *Geophys. J. Int*. **119**, 44-68.

KEMPER, M. & HARJES H.-P., 1991. Processing and analysis of MSP experiments within the KTB project, in Continental Lithosphere: Deep Seismic Reflections, edited by R. Meissner et al., pp. 135-145, AGU, Washington, D.C.

KESSELS, W., KÜCK, J. & ZOTH, G., 1992. Hydraulische Untersuchingen in der Bohrung KTB-Oberpfalz HB bis 5000 m. KTB Report 92-1, pp. 169-205. Schweitzerbart'sche Verlagbuchhandlung, Stuttgart.

KOHL, T. & RYBACH, L., 1996. Thermal and hydraulic aspects of the KTB drill site. *Geophys, J. Int.* **124**, 756-772.

KOVESI, P., 1999. Image Features From Phase Congruency. *A Journal of Computer Vision Research*. MIT Press. Volume **1**, Number 3.

KÖRBE, M., STILLER, M., HORSTMEYER, H. & RÜHL, T., 1997. Migration of the 3-D deep-seismic reflection survey at the KTB location, Oberpfalz, Germany. *Tectonophysics* **271**, 135-156.

KRUIZINGA, P. & PETKOV, N., 1999. Non-linear operator for oriented texture, *IEEE Trans. on Image Processing*, **8** (10), 1395-1407.

LACHENBRUCH, A.H., 1970. Crustal temperature and heat production: implications of the linear heat flow relation. *J. Geophys*. Res. **75**, 3291–3300.

LEHMANN, H., WANG, K. & CLAUSER, C., 1998. Parameter identification and uncertainty analysis for heat transfer at the KTB drill site using a 2-D inverse method. *Tectonophysics* **291**, 179-194.

LEVESQUE, V., 2000. Texture segmentation using Gabor filters. Center for Intelligent Machines, McGill University.

LUO, Y., WANG, Y.E., ALBINHASSAN, N.M., & ALFARAJ, M.N., 2006. Computation of dips and azimuths with weighted structure-tenser approach. *Geophysics*, Vol.,**71**, Issue 5, pp. V119-V121.

LÜSCHEN, E., SÖLLNER, W., HOHRATH, A. & RABBEL, W., 1991. Integrated P- and S-wave borehole experiments at the KTB-deep drilling site in the Oberpfalz area (SE Germany). - In: R. Meissner et al. (eds.): Continental Lithosphere: Deep Seismic Reflections. *Geodynamics Series* Volume 22, p. 121-133, American Geophysical Union, Washington D.C.

MANDELBROT, B.B., 1983. The Fractal Geometry of Nature. Freeman, New York.

MATTE, P.H., MALUSKI, H., RAJLICH, P. & FRANKE, W., 1990. Terrane boundaries in the Bohemian Massif: Result of large-scale Variscan shearing. *Tectonophysics*, **177,** 151-170.

MOTTAGHY, D., PECHNIG, R. & VOGT, C., 2011. The geothermal project Den Haag: 3D numerical models for temperature prediction and reservoir simulation, *Geothermics,* **40** (3), 199-210.

NGÔ, C., LESCURE, I. & CHAMPVILLARD, G., 2006. WP3: Electricity generation technology and integration system. Geothermal conversion. European Sustainable Electicity Comprehensive Analysis of Future European Demand and Generation of European Electricity and its Security of Supply.

ONDRAK, R., WENDEROTH, F., SCHECK, M. & BAYER, U., 1998. Integrated geothermal modeling on different scales in the Northeast German basin. *Geol Rundsch* **87**: 32-42.

PEACEMAN, D. W., 1983. Interpretation of well-block pressure in numerical reservoir simulation with non-square grid blocks and anisotropic permeability, *Society of Petroleum Engineers Journal*, **23(3)**, 531–543.

PECHNIG, R., HAVERKAMP, S., WOHLENBERG, J., ZIMMERMANN, G. & BURCKHARDT, H., 1997. Integrated log interpretation in the German Continental Deep Drilling Program: Lithology, porosity, and fracture zones, *J. Geophys*. Res., **102**, 18,363 – 18,390.

PHILLIPS, W.S., RUTLEDGE, J.T., HOUSE, L.S. & FEHLER, M.C., 2002. Induced microearthquake patterns in hydrocarbon and geothermal reservoirs: Six case studies, preprint *Pure and Applied Geophysics,* **159**, 345-369.

PRIBINOW, D., BÜCKER, C., RAUEN, A., SPANGENBERG, E., WIENAND, J. & SOFFEL, H.C., 1992. KTB Hauptbohrung. Results of Geoscientific Investigation in the KTB Field Laboratory. 0 – 6000 m. – In: Emmermann, R., Dietrich, H.-G., Lauterjung, J., Wöhrl, T. (eds.): KTB Report 92-2, D1-D42, Hannover.

PRIBINOW, D., WILLIAMS, F. & BURKHARDT, H., 1993. Well Log-derived Estimates of Thermal Conductivity in Crystalline Rocks Penetrated by the 4-km Deep KTB Vorbohrung. *Geophysical Research Letters,* Vol. **20**, No. 12, 1155-1158.

RATH, V., WOLF, A. & BÜCKER, M., 2006. Joint three-dimensional inversion of coupled groundwater flow and heat transfer based on automatic differentiation: sensitivity calculation, verification, and synthetic examples, *Geophys. J. Int.,* **167**, 453–466.

RAUEN, A. & WINTER, H., 1995. Petrophysical Properties. KTB Report 95-2, D1-D45; Hannover.

RYBACH, L., 1976. Radioactive heat production in rocks and its relation to other petrophysical parameters. *Pageoph*, Vol. **114**. Birkhäuser Verlag, Basel.

RYBACH, L., 1992. An attempt to interpret the temperature profile of the KTB pilot drillhole (Germany) by paleoclimatic considerations. Paleogeogr., Paleoclimatol., Paleoecol 98, 193–197.

RYBACH, L. & MONGILLO, M., 2006. Geothermal Sustainability – A Review with Identified Research Needs. *CRC Transactions*, Vol. **30**.

SAUSSE, J., DEZAYES, C., GENTER, A. & BISSET, A., 2008. Characterization of fracture connectivity and fluid flow pathways derived from geological interpretation and 3D modelling of the deep seated EGS reservoir of Soultz (France). Proceedings, Thirty-third workshop on geothermal reservoir engineering, Stanford.

SCHMOLL, J., BITTNER, R., DÜRBAUM, H.-J., HEINRICHS, T., MEISSNER, R., REICHERT, C., R¨U HL, T. & WIEDERHOLD, H., 1989. Oberpfalz deep seismic reflection survey and velocity studies, in The German Continental Deep Drilling Program (KTB). pp. 99-149, Springer-Verlag.

SIEBEL, W., HÖHNDORF, A. & WENDT, I., 1995. Origin of late Variscan granitoids from NE Bavaria, Germany, exemplified by REE and Nd isotope systematics. *Chem Geol* **125**: 249 – 270.

SIMON, M. & GEBRANDE, H., 1994. New seismic images of the Earth's crust: migration before stack. KTB Rep. 94-2: A87 – A96.

SOFFEL, H.C., BÜCKER, C., GEBRANDE, H., HUENGES, E., LIPPMANN, E., POHL, J., RAUEN, A., SCHULT, A., STREIT, K.M. & WIENAND, J., 1992. Physical parameters measured on cores and cuttings from the pilot well (0 m – 4000.1 m) of the German Continental Deep Drilling Program (KTB) in the Oberpfalz area, Bavaria, Federal Republic of Germany, - *Surveys in Geophysics,* **13**, 1-34, Kluwer Academic Publisher, Netherlands.

STAUFFER, D. & AHARONY, A., 1994. Introduction to Percolation Theory. Taylor and Fransis, London.

STILLER, M., 1991. 3-D vertical incidence seismic reflection survey at the KTB location. In: R. Meissner, L. Brown, H.-J. Dürbaum, W. Franke, K. Fuchs and F. Seifert, Editors, *Continental Lithosphere: Deep Seismic Reflections Geodynamics* **22**, pp. 101–113.

STILLER, M., 1992. Preliminary generation of a stacked data volume of the entire ISO89 3D data set using an envelope technique, *KTB Rep.* **92-5**, pp. 3-29, Niedersächsisches Landesamt für Bodenforsch., Hannover, Germany.

STILLER, M. & TORMANN, M., 1992. Application of a simplified horizon migration process to the data of the 3D-seismics ISO'89, *KTB Rep.* **92-5**, pp. 53-65, Niedersächsisches Landesamt für Bodenforsch., Hannover, Germany.

STOCKMAYER, W. H., 1943. Theory of molecular size distribution and gel formation in branched polymers. *Journal of Chemical Physics*. **11**, 45-55.

TURCOTTE, D.L., 1997. Fractals and Chaos in Geology and Geophysics, 2nd Ed., Cambridge Univ. Press, pp. 398.

VOGT, C., MARQUART, G., KOSACK, C.,WOLF, A., & CLAUSER, C., 2011. Estimating the permeability distribution and its uncertainty at the EGS demonstration reservoir Soultz-sous-Forêts using the ensemble Kalman filter, *Water Resources Research*, submitted.

VOGT, C., IWANOWSKI-STRAHSER, K., MARQUART, G., ARNOLD, J., MOTTAGHY, D., PECHNIG, R., GNEJZDA, D. & CLAUSER, C., 2012. Integrated risk assessment in geothermal reservoir modeling. A case study. Submitted.

WENZEL, F., BRAM, K. & REICHERT, C., 1995. Physical Insight in a Crustal Reflector at the KTB, *Technical Report, Niedersächsisches Landesamt für Bodenforschung, Hannover, Germany,* unpublished.

WIEDERHOLT, H., 1991. Investigation of structures and anisotropy by a 3D expanding - spread experiment, in Continental lithosphere: Deep Seismic Reflections, *Geodyn. Ser*., vol. **22**, edited by R. Meissner et al., pp. 115-120, AGU, Washington, D.C.

WILHELM, H., 2000. Undisturbed temperature in the main drillhole of the German Continental Deep Drilling Program predicted from temperature logs recorded after shut-in. *Geothermics* **20**, 393-406.

WINTER, H. & PRIBINOW, D., 1995. Radioactive elements and heat production rate in the KTB. 8th Colloquium of the German research program "Kontinentale Tiefbohrung", 25.-26. May, Giessen, Proc., 205-209.

WOLF, A., 2009. Parallelism Application Experience: Tuning of the SHEMAT – Suite. ScaleMP Workshop 2009.

YILMAZ, Ö., 2001. Seismic Data Analysis; Volume I and II. Tulsa: Society of Exploration Geophysicists.

ZULAUF, G. & DUYSTER, J., 1997. Faults and veins in the superdeep well KTB: constraints on the amount of Alpine intra-plate thrusting and stacking of Variscan basement (Bohemian Massif, Germany). *Geol. Rundsch*. **86**, Suppl.: S28 – S33. Springer Verlag.

ZULAUF, G., MARIER, M. & STÖCKHERT, B., 1997. Depth of intrusion and thermal modeling of the Falkenberg granite (Oberpfalz, Germany). *Geol. Rundsch.* **86**, Suppl.: S87 – S92.

List of Abbreviations

C	covariance matrix	
c_f^p	specific heat capacity of fluid	[$Jkg^{-1}K^{-1}$]
c_s^p	specific heat capacity of rock	[$Jkg^{-1}K^{-1}$]
D	fractal dimension	
E, F, G	direction cosines	
g	gravitational acceleration	[ms^{-2}]
$g_{\lambda,\theta,\varphi,\gamma}$	Gabor filter kernel	
H	hydraulic head	[m]
h	box size	
I	imaginary part of a complex trace	
k	permeability	[m^2]
N	number of boxes	
$-N_c$	cumulative number of boxes	
P	pressure	[MPa]
P_p	pore pressure	[MPa]
p	probability	
p_c	critical probability	
Q	heat-flow	[mWm^{-2}]
q	specific discharge (Darcy velocity)	[ms^{-1}]
q_T	heat flux	[Wm^{-2}]
q_w	circulation rate	[m^3s^{-1}]
R	real part of a complex trace	
r	linear dimension	[m]
r_c	cell radius	[m]
r_w	well radius	[m]
S_s	specific storage coefficient	[L^{-1}]
ST	structural tensor	
T	temperature	[°C]
$T_{surface}$	surface temperature	[°C]
T_{red}	reduced temperature	[°C]
t	time	[s]
$V(V_x, V_y, V_z)$	gradient vector	
v_f	flow velocity	[ms^{-1}]
W_f	hydraulic source term	
W_T	heat source term	
w	weighting function	
x, y, z	space coordinates	[m]

$\bar{x}, \bar{y}, \bar{z}$	variable means	[m]
γ	spatial aspect ratio	
η	dynamic viscosity	[Pa s]
θ	orientation of the Gabor filter	
λ	wavelength	[m]
λ_T	thermal conductivity	[$Wm^{-1}K^{-1}$]
λ_f	hydraulic conductivity	[ms^{-1}]
μ	coefficient of friction	
ρ_0	reference density	[kg m^{-3}]
ρ_f	fluid density	[kg m^{-3}]
ρ_s	rock density	[kg m^{-3}]
σ	standard deviation	
$\sigma_1, \sigma_2, \sigma_3$	three principal stresses	[Pa]
σ_n	normal stress	[Pa]
τ	shear stress	[Pa]
ϕ	porosity	[%]

Acknowledgements

This dissertation was conducted at the Institute of Geosciences at the Christian-Albrechts-University in Kiel as part of the project MeProRisk (Neuartige Metodik zur Aufsuchung, Erschließung und Nutzung geothermischer Lagerstätten. Toolbox zur Prognose und Risikobewertung. Seismische Verfahren zur Prognose geothermischer Lagerstätten). The reflection seismic data and downhole data were provided by the GFZ Potsdam.

It is a pleasure to thank those who made this thesis possible.

In the first place, I would like to express my deepest gratitude to my advisor, Prof. Dr. Wolfgang Rabbel for his guidance, care, patience, and the excellent atmosphere during the research. I would have never been able to finish (or even start) the work without his support and his positive attitude.

I would also like to thank Prof. Dr. Hans-Jürgen Götze for accepting to be the second examiner.

I want to thank Gabriele Marquart for her kind introduction into the SHEMAT software and Christian Vogt for his obviously unlimited amount of patience which he showed every time I flooded him with questions. Without their support, this thesis would be at least one chapter shorter.

Special thanks go to my “Doktorschwester” Katja Iwanowski-Strahser for her help, the many discussions and suggestions and the company during project meetings. I also really appreciated the many ideas for work-breaks and after-university activities, which in short can be described as creative and highly entertaining.

Of course, I shared the best and the worst moments of my dissertation journey with many people. I would like to thank the many colleagues, who I now with pleasure, count to my friends. Thank you for all the suggestions concerning my work, the company during the lunch breaks and the pleasant atmosphere which I will surely miss in the future. In particular, I want to mention the closest ones: Tina, Matthias, Ali and Zuzana, who were always there when help or distraction was needed.

Many thanks go to Deniz, who stood by me through the good times and the not so good ones. His support, even though it was mainly virtual, was essential for my mental balance.

Finally, I would like to thank my parents, my brothers, my aunts and my cousin and of course my two closest friends who supported me from the distance and welcomed me warmly every time I came back home or for visit. Mamo, Eviku, thanks to the almost daily chats with you both, I still remember my native language.

Last, but not least, I want to thank whoever invented the internet. :)

Curriculum Vitae

Name	Eva Szalaiová
Date of birth	14th July 1981
Place of birth	Bratislava, Slovakia
Nationality	Slovak

Education

- 2011 - 2012: Doctoral studies at the Institute of Geosciences, Applied Geophysics, Christian-Albrechts-University Kiel, Germany.
- 2008 – 2011: Doctoral studies and employed as member of a research staff at the Institute of Geosciences, Applied Geophysics, Christian-Albrechts-University Kiel, Germany.
- 2006 – 2008: Doctoral studies (unfinished) at the Department of Applied and Environmental Geophysics, Faculty of Natural Sciences, Comenius University Bratislava, Slovakia.
- 2004 – 2006: Master degree at the Department of Applied and Environmental Geophysics, Faculty of Natural Sciences, Comenius University Bratislava, Slovakia.
- 2003 – 2004: Participation at an exchange program at the Saga University, Japan.
- 2000 – 2003: Bachelor degree at the Department of Applied and Environmental Geophysics, Faculty of Natural Sciences, Comenius University Bratislava, Slovakia.
- 1995 – 1999: St. Ursula High School, Bratislava, Slovakia.

Ich erkläre hiermit, dass ich die vorliegende Arbeit – abgesehen von der Beratung durch den Betreuer - selbständig und ohne Benutzung anderer, als der angegebenen Hilfsmittel angefertigt habe. Die aus fremden Quellen direkt übernommenen Gedanken sind kenntlich gemacht. Diese Arbeit wurde in gleicher oder ähnlicher Form keiner anderen Prüfungsbehörde vorgelegt oder veröffentlicht. Die Arbeit ist unter Einhaltung der Regeln guter wissenschaftlicher Praxis enstanden.

Kiel, den 29. Februar 2012

Eva Szalaiová